






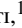




















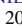






An Early-Time Optical and Ultraviolet Excess in the type-Ic SN 2020oi

ALEXANDER GAGLIANO ^{1,2,3,4} LUCA IZZO ⁵ CHARLES D. KILPATRICK ^{6,7} BRENNIA MOCKLER ⁸
 WYNN VICENTE JACOBSON-GALÁN ^{6,7,4} GIACOMO TERRERAN ^{6,7} GEORGIOS DIMITRIADIS ^{8,9} YOSSEF ZENATI ¹⁰
 KATIE AUCHETTL ^{11,12,8,5} MARIA R. DROUT ^{13,14} GAUTHAM NARAYAN ^{1,2,3} RYAN J. FOLEY ⁸ R. MARGUTTI ^{6,7}
 ARMIN REST ^{15,10} D. O. JONES ^{8,16} CHRISTIAN AGANZE ¹⁷ PATRICK D. ALEO ^{1,2,3} ADAM J. BURGASSER ¹⁷
 D. A. COULTER ^{8,4} ROMAN GERASIMOV ¹⁷ CHRISTA GALL ⁵ JENS HJORTH ⁵ CHIH-CHUN HSU ¹⁷ EUGENE A. MAGNIER ¹⁸
 KAISEY S. MANDEL ¹⁹ ANTHONY L. PIRO ¹⁴ CÉSAR ROJAS-BRAVO ⁸ MATTHEW R. SIEBERT ^{8,4} HOLLAND STACEY ²⁰
 MICHAEL CULLEN STROH ^{6,7} JONATHAN J. SWIFT ²⁰ KIRSTY TAGGART ⁸ SAMAPORN TINYANONT ⁸

(YOUNG SUPERNOVA EXPERIMENT)

¹Department of Astronomy, University of Illinois at Urbana-Champaign, 1002 W. Green St., IL 61801, USA²National Center for Supercomputing Applications, Urbana, IL, 61801, USA³Center for Astrophysical Surveys, Urbana, IL, 61801, USA⁴National Science Foundation Graduate Research Fellow⁵DARK, Niels Bohr Institute, University of Copenhagen, Jagtvej 128, 2200 Copenhagen, Denmark⁶Department of Physics and Astronomy, Northwestern University, Evanston, IL 60208, USA⁷Center for Interdisciplinary Exploration and Research in Astrophysics (CIERA), 1800 Sherman Ave, Evanston, IL 60201, USA⁸Department of Astronomy and Astrophysics, University of California, Santa Cruz, CA 95064, USA⁹School of Physics, Trinity College Dublin, The University of Dublin, Dublin 2, Ireland¹⁰Department of Physics and Astronomy, The Johns Hopkins University, Baltimore, MD 21218¹¹School of Physics, The University of Melbourne, VIC 3010, Australia¹²ARC Centre of Excellence for All Sky Astrophysics in 3 Dimensions (ASTRO 3D)¹³David A. Dunlap Department of Astronomy and Astrophysics, University of Toronto, 50 St. George Street, Toronto, Ontario, M5S 3H4 Canada¹⁴The Observatories of the Carnegie Institution for Science, 813 Santa Barbara St., Pasadena, CA 91101, USA¹⁵Space Telescope Science Institute, Baltimore, MD 21218¹⁶NASA Einstein Fellow¹⁷Center for Astrophysics and Space Science, University of California San Diego, La Jolla, CA 92093, USA¹⁸Institute for Astronomy, University of Hawaii, 2680 Woodlawn Drive, Honolulu, HI 96822, USA¹⁹Institute of Astronomy and Kavli Institute for Cosmology, Madingley Road, Cambridge, CB3 0HA, UK²⁰The Thacher School, 5025 Thacher Rd, Ojai, CA 93023**ABSTRACT**

We present photometric and spectroscopic observations of Supernova 2020oi (SN 2020oi), a nearby (~ 17 Mpc) type-Ic supernova (SN Ic) within the grand-design spiral M100. We undertake a comprehensive analysis to characterize the evolution of SN 2020oi and constrain its progenitor system. We detect flux in excess of the fireball rise model $\delta t \approx 2.5$ days from the date of explosion in multi-band optical and UV photometry from the Las Cumbres Observatory and the Neil Gehrels *Swift* Observatory, respectively. The derived SN bolometric luminosity is consistent with an explosion with $M_{\text{ej}} = 0.81 \pm 0.03 M_{\odot}$, $E_k = 0.79 \pm 0.09 \times 10^{51}$ erg s⁻¹, and $M_{\text{Ni56}} = 0.08 \pm 0.02 M_{\odot}$. Inspection of the event's decline reveals the highest $\Delta m_{15,\text{bol}}$ reported for a stripped-envelope event to date. Modeling of optical spectra near event peak indicates a partially mixed ejecta comparable in composition to the ejecta observed in SN 1994I, while the earliest spectrum shows signatures of a possible interaction with material of a distinct composition surrounding the SN progenitor. Further, *Hubble Space Telescope* (HST) pre-explosion imaging reveals a stellar cluster coincident with the event. From the cluster photometry, we derive the mass and age of the SN progenitor using stellar evolution models implemented in the BPASS library. Our results indicate that SN 2020oi occurred in a binary system from a progenitor of mass $M_{\text{ZAMS}} \approx 9.5 \pm 1.0 M_{\odot}$, corresponding to an age of 27 ± 7 Myr. SN 2020oi is the dimmest SN Ic event to date for which an early-time flux excess has been observed, and the first in which an early excess is unlikely to be associated with shock-cooling.

Keywords: supernovae, core-collapse, progenitor, stripped-envelope

1. INTRODUCTION

Core-collapse supernovae (CCSNe) are both common (Modjaz et al. 2019) and vital in shaping the chemical evolution of the universe (van de Voort et al. 2020); however, many questions remain concerning the nature of their progenitor systems and their behavior immediately before explosion. The final state of a progenitor star likely plays a decisive role in the large observed diversity of CCSNe, influencing their total luminosities (e.g., for SN IIP; Barker et al. 2021), the composition of their ejecta (Thielemann et al. 1996), and the compact remnant that remains when the ejecta clear (Ugliano et al. 2012). These questions have motivated decades of targeted searches for the progenitors of CCSNe (Aldering et al. 1994; Smartt et al. 2003; Smartt 2009; Van Dyk et al. 2014; Smartt 2015; Kilpatrick et al. 2017; Kochanek et al. 2017; Van Dyk et al. 2018; Kilpatrick et al. 2018a; O’Neill et al. 2019; Kilpatrick et al. 2021), beginning with the type-II SN 1987A (West et al. 1987). Nevertheless, despite a wealth of high-resolution pre-explosion imaging within nearby galaxies, only a few progenitors have ever been directly observed.

In the absence of direct detections of CCSN progenitors, multiple lines of indirect evidence have proven fruitful. The first of these is the host galaxy and local environment of the supernova (SN). Owing to the short-lived nature of core-collapse progenitors ($\lesssim 50$ Myr for single stars), stellar populations spatially coincident with the SN are likely to share a formation history. As a result, tight constraints can be placed on the age and mass of a progenitor system by comparing stellar evolution models to resolved photometry from stars near the SN site (Maund 2017; Williams et al. 2018). This method has also been successfully applied to other SN classes with similarly short-lived progenitor systems (e.g., for SNe Iax; Takaro et al. 2019). Host-galaxy spectroscopy can also be used to derive local properties of underlying stellar populations (Kuncarayakti et al. 2015; Galbany et al. 2016; Kuncarayakti et al. 2018; Meza et al. 2019).

Complementing local environment studies, early-time observations are a critical tool in our investigation into the progenitors of CCSNe. In a handful of events, high-cadence observations have facilitated the detection of the X-ray or UV emission associated with shock breakout (Campana et al. 2006; Soderberg et al. 2008; Modjaz et al. 2009; Garnavich et al. 2016; Bersten et al. 2018), during which the explosion shock traveling at velocity v_S escapes the edge of the progenitor star (or the circumstellar medium, if the environment is particularly dense) where the optical depth is $\tau \approx v_S/c$ (Barbarino et al. 2017; Bersten et al. 2018; Xiang et al. 2019). As the shock front cools, its associated emission may further extend into optical wavelengths. Because shock breakout oc-

curs at the edge of the progenitor, the signal uniquely encodes its pre-explosion radius and surface composition (Waxman & Katz 2017). Panchromatic photometry and spectroscopy obtained in the first few days of an explosion can also reveal the presence of circumstellar material by its interaction emission or distinct composition, respectively, encoding the pre-explosion mass-loss history of the progenitor star. In the absence of this early emission, photometric and spectroscopic modeling of later explosion phases still provides valuable insights (e.g., Drout et al. 2011; Morozova et al. 2015; Lyman et al. 2016; Jerkstrand 2017; Taddia et al. 2018).

Type-Ic supernovae (SNe Ic) are a class of core-collapse phenomena for which progenitor searches in recent years have motivated new questions. These explosions are characterized by an absence of hydrogen and helium lines in their spectra, indicating pre-explosion stripping of the stellar envelope. The loss of hydrogen from the outermost layers of the progenitor star is believed to occur either through Roche-lobe overflow onto a stellar companion (in the case of a binary system) or through stellar winds originating from a single progenitor (Yoon et al. 2010; Smith et al. 2011; Yoon 2015). Both channels result in a Helium star that loses its remaining envelope through line-driven winds (Smith 2014; Yoon 2017), but their relative roles in driving type-Ic and type-Ib (in which only hydrogen has been stripped) explosions remain unknown.

The progenitor mass required for explosion as an SN Ic is lower for binary than for single systems, and constraints have often favored the low-mass solution (Drout et al. 2011; Cano 2013; Gal-Yam 2017); further, the dearth of progenitor detections disfavors single massive stars whose comparatively bright flux should be detectable above the magnitude limit of the observations (Eldridge et al. 2008; Groh et al. 2013; Kelly et al. 2014). Nevertheless, detailed investigations into individual objects have revealed unique exceptions: pre-explosion photometry obtained by Cao et al. (2013) for the type-Ib SN iPTF13bvn was found to be consistent with models for a single massive Wolf-Rayet (although this interpretation has been challenged; see Folatelli et al. 2016). Further complicating these efforts, the nature of the SN Ic progenitor system is often ambiguous from pre-explosion photometry, as exemplified by the type-Ic SN 2017ein (Kilpatrick et al. 2018a; Van Dyk et al. 2018).

Uncovering the true nature of the type-Ic progenitor system is critical to understanding what conditions give rise to normal SNe Ic and the more energetic broad-lined type-Ic (Ic-BL) events. Type-Ic-BL are the only SNe that have been unambiguously associated with long-duration Gamma-Ray Bursts (LGRBs) (MacFadyen & Woosley 1999; Hjorth et al. 2003;

Nagataki 2018; Zenati et al. 2020), but we do not know if these phenomena arise from distinct explosion mechanisms or if there is a continuum of stripped-envelope scenarios varying in progenitor mass, explosion velocity, and explosion geometry (Pignata et al. 2011; Taubenberger et al. 2011). Because LGRB emission occurs within a narrow opening angle while SN radiation is isotropic, this picture is further complicated by the possibility of undetected "choked" or off-axis jets arising from SNe Ic-BL (Urata et al. 2015; Izzo et al. 2020). Can single Wolf-Rayet stars yield "normal" type-Ic explosions, or are these events the endpoint of binary interaction, with Wolf-Rayet stars only responsible for GRB-SNe and SNe Ic-BL? Accurate progenitor mass and age estimates will be key for distinguishing these two formation channels and validating models for the physical environments that give rise to SNe Ic, SNe Ic-BL, and LGRBs (Mazzali et al. 2003; Woosley & Bloom 2006).

In this work, we undertake an analysis of SN 2020oi to shed light on the nature of its progenitor system. SN 2020oi was discovered by the Automatic Learning for the Rapid Classification of Events (ALeRCE) transient broker on January 7th, 2020 at 13:00:54.000 UTC (Forster et al. 2020) from the alert stream of the Zwicky Transient Facility (ZTF; Bellm et al. 2019a). It was classified as a type-Ic SN by the authors two days later using the Goodman Spectrograph at the Southern Astrophysical Research Telescope (Siebert et al. 2020b). The event occurred at $\alpha, \delta = 185.7289^\circ, 15.8236^\circ$ (J2000), $\sim 4.67''$ North from the nucleus of the SAB(s)bc spiral galaxy Messier 100 (M100/NGC 4321) presiding at a distance of 17.1 ± 1.8 Mpc (Freedman et al. 1994a). SN 2020oi is the seventh SN discovered in M100, preceded by the unclassified SNe 1901B, 1914A, and 1959E; and the type-III SN 1979C (Carney 1980), type-Ia SN 2006X (Quimby et al. 2006), and calcium-rich transient SN 2019ehk (Jacobson-Galán et al. 2020). As the most recent in this series of observed M100 explosions spanning over a century, SN 2020oi has been continuously monitored since its discovery, and a wealth of pre-explosion data have been collected on its local environment. For these reasons, SN 2020oi represents an ideal event for constraining SN Ic progenitor properties and explosion physics.

Because of the close proximity of M100, redshift-based distance estimates are likely to be biased by the peculiar velocity of the galaxy. Archival estimates for the distance to M100 range from 13 Mpc to 20 Mpc (e.g., Smith et al. 2007; Tully et al. 2008, 2016). In this paper, we assume a redshift-independent distance of 17.1 Mpc corresponding to the distance derived from Cepheids (Freedman et al. 1994a). We note that the distance adopted in the analysis for the Ca-rich transient SN 2019ehk in the same galaxy was $d \approx 16.2$ Mpc, while the distances used in the previous analyses of SN 2020oi were 14 Mpc, 16.22 Mpc, and 16 Mpc, respectively (Horesh

et al. 2020; Rho et al. 2021; Tinyanont et al. 2021). Although these values are roughly consistent, they will be the source of some discrepancy between the SN parameters derived in this work and those from the previous studies.

We have observed a bump lasting ~ 1 day and beginning ~ 2 days from the time of explosion in nearly all bands of our optical and UV photometry. In *gri* bands, we observe a brief increase and decrease in flux; in *u* band, we observe only a flux decrease (see Fig. 2). The coincidence of this phenomenon across bands suggests a high-temperature component to the early-time photometry of SN 2020oi above the standard SN rise.

Early-time bumps such as the one observed in the SN 2020oi photometry are extremely rare among spectroscopically-standard SNe Ic, particularly when observed in multiple bands and across multiple epochs. Early-time ATLAS data revealed emission in excess of a power-law rise for SN 2017ein, which was interpreted as the cooling of a small stellar envelope that was shock-heated (Xiang et al. 2019). A decrease in *V*-band flux in the first photometric observations of SN LSQ14efd (Barbarino et al. 2017) was similarly attributed to shock-cooling. An extended ($> 500 R_\odot$), low-mass ($0.045 M_\odot$) envelope, potentially ejected by a massive Wolf-Rayet progenitor pre-explosion, was proposed to explain the luminous first peak in SN iPTF15dtg (Taddia et al. 2016). The multi-wavelength coverage of the SN 2020oi bump, coupled with the classification spectrum obtained immediately following its decline, together comprise a rich dataset for investigating the early-time behavior of SNe Ic.

In this paper, we describe the photometric and spectroscopic coverage of SN 2020oi spanning ~ 1 year of observations and the corresponding constraints that these data provide for the progenitor of this SN Ic. Further, we provide a detailed spectroscopic analysis of M100 and the region immediately surrounding SN 2020oi using pre-explosion Integral Field Unit (IFU) spectroscopy with the Multi Unit Spectroscopic Explorer (MUSE) mounted on the European Southern Observatory Very Large Telescope. By presenting a comprehensive picture of the most rapidly fading SN Ic observed to date, this work will shed additional light on the full diversity of stripped-envelope explosions and their origins.

Three previously published works have investigated this SN: Horesh et al. (2020), who reported evidence of dense circumstellar material from radio observations; Rho et al. (2021), who modeled near-IR spectroscopy to derive the presence of carbon monoxide and dust; and Tinyanont et al. (2021), who presented spectropolarimetric observations suggesting SN 2020oi is unlikely to be an asymmetric explosion. None of these studies investigated the early-time excess reported here, nor did they attempt an analysis of the explosion environment from host-galaxy spectroscopy.

Our paper is laid out as follows. In §2, we outline the photometric and spectroscopic observations collected for SN 2020oi, which span optical, UV, and X-ray wavelengths. We use the notation δt to refer to the number of days from the explosion time of MJD 58854.0, which is determined using a fireball rise model outlined in §5. We estimate the host-galaxy reddening in §3 and use Gaussian Process Regression to derive the bolometric light curve for the explosion in §4. §5 is devoted to the explosion parameters of SN 2020oi, which are estimated using three different models of the event in the photospheric phase and compared to previous stripped-envelope explosions. Next, we constrain the mass-loss rate of the progenitor from our X-ray observations in §6. We model our spectral sequence near peak light using a radiative transfer code to characterize the ejecta in §7, and independently fit the unique early-time spectrum in §8. In §9, we consider physical interpretations for the early-time optical and UV excess. §10 is devoted to fitting the *HST* pre-explosion photometry of the stellar cluster coincident with the explosion (see §2.1 for details). We then analyze the stellar population within SN 2020oi’s local environment using MUSE IFU spectroscopy in §11, and derive a final age for the SN progenitor in §12. We conclude by summarizing our major findings in §13.

2. OBSERVATIONS

2.1. *HST* Pre- and Post-Explosion Observations

We obtained archival *Hubble Space Telescope* (*HST*) images of the central region of M100 using the Hubble Legacy Archive¹ and the Mikulski Archive for Space Telescopes (MAST)². These observations span nearly three decades, beginning with the calibration of the Wide Field/Planetary Camera 2 (WFPC2) (Brown 1992) for the *Hubble Space Telescope*’s Key Project (Freedman et al. 1994b; Hill et al. 1995) and ending with a study (Proposal ID 16179; PI: Filippenko) into the host environments of nearby SNe. We present a false-color composite of *HST* pointings of M100 post-explosion in Figure 1, in which we have marked the location of SN 2020oi. The diversity of studies involving M100, particularly concerning the dynamics and stellar populations immediately surrounding its nucleus, provide ample context for studying the pre-explosion environment. We present a detailed summary of the *HST* observations in Table 1. As in Kilpatrick et al. (2018a), we use the *astrodrizzle* and *drizzlepac* packages (Gonzaga et al. 2012) to reduce these archival images in the python-based *HST* imaging pipeline *hst123*³. We performed all *HST* photometry using a circular

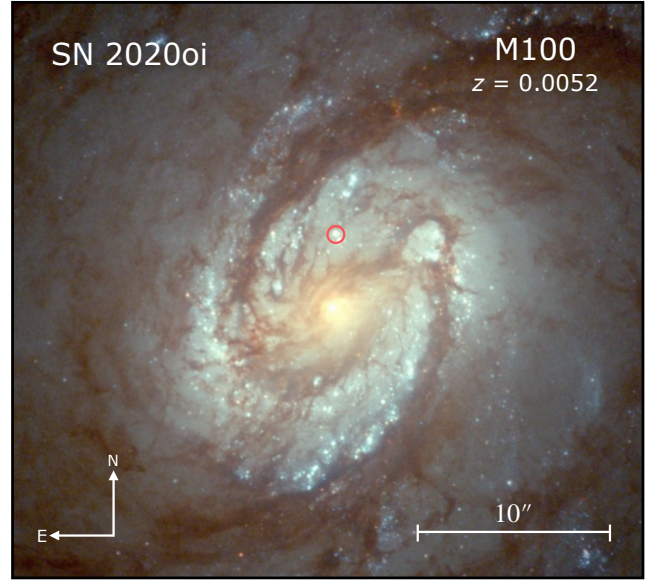


Figure 1. A false-color *HST* image of the nucleus of M100 post-explosion. The location of SN 2020oi is circled, and the physical scale is given bottom right.

aperture fixed to a $0.2''$ width and centered on the location of SN 2020oi as inferred from post-explosion F555W observations. Using the python-based *photutils* package (Bradley et al. 2020), we extracted an aperture in each drizzled frame and estimated the background contribution from the median value within an annulus with inner and outer radii of $0.4''$ and $0.8''$, respectively, and centered on the circular aperture. We derived the AB magnitude zero point within each frame from the *PHOTPLAM* and *PHOTFLAM* keywords in the original image headers⁴.

Although no progenitor is immediately evident in the pre-explosion imaging, a marginally-extended brightness excess likely corresponding to a stellar cluster is nearly coincident with the SN explosion. We calculate the nominal offset between the cluster and the explosion in *HST*/WFC3 UVIS imaging to be 0.55 px, corresponding to a physical separation of less than 2.3 parsecs. This cluster is also visible in the most recent *HST* images obtained (MJD 59267, $\delta t \approx 413$ days). We analyze the photometric properties of this source in §10.

¹ <https://hla.stsci.edu/>

² <https://archive.stsci.edu/>

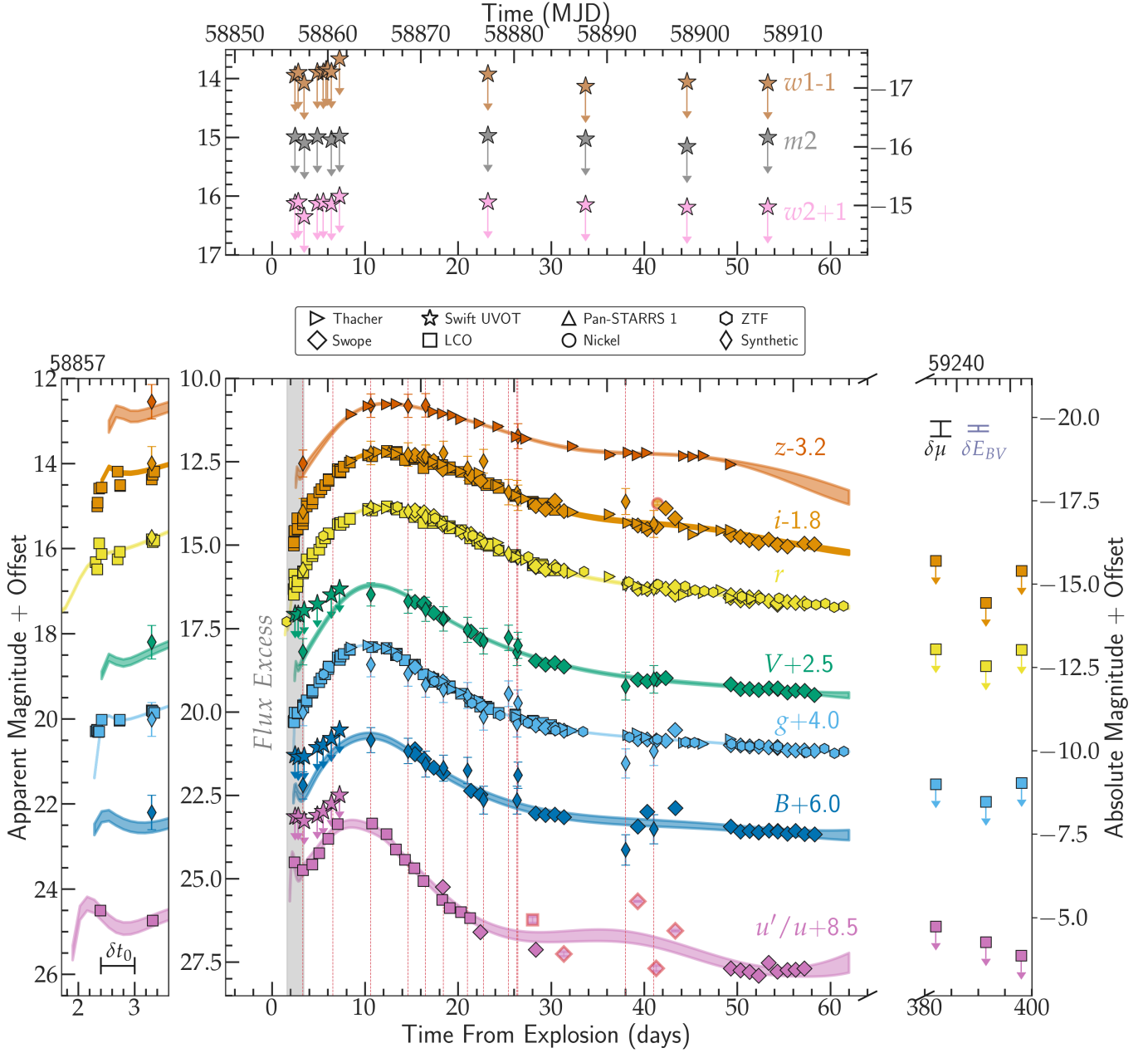
³ <https://github.com/charliekilpatrick/hst123>

⁴ i.e., following the standard formula for WFPC2, ACS, and WFC3 zero points as in <https://www.stsci.edu/hst/instrumentation/acs/data-analysis/zeropoints>

Table 1. *HST* Pre-Explosion Cluster and SN 2020oi Photometry

Date (UT)	MJD	Phase (day)	Instrument	Filter	Exposure	Magnitude	Uncertainty	3 σ Limit	Proposal ID	PI
1993-12-31	49352.6	-9501.4	WFPC2	F555W	1800.0	19.419	0.062	26.242	5195	Sparks
1993-12-31	49352.6	-9501.4	WFPC2	F439W	1920.0	19.460	0.114	24.857	5195	Sparks
1993-12-31	49352.7	-9501.3	WFPC2	F702W	2400.0	19.657	0.057	25.990	5195	Sparks
1994-01-07	49359.5	-9494.5	WFPC2	F555W	1668.5	19.443	0.048	26.228	5195	Sparks
1994-01-07	49359.5	-9494.5	WFPC2	F439W	1920.0	19.444	0.041	24.839	5195	Sparks
1994-01-07	49359.6	-9494.4	WFPC2	F702W	2318.5	19.630	0.095	25.833	5195	Sparks
1999-02-02	51212.0	-7642.0	WFPC2	F218W	1200.0	19.668	0.059	22.845	6358	Colina
2004-05-30	53155.8	-5698.2	ACS/HRC	F814W	1200.0	19.837	0.005	25.430	9776	Richstone
2004-05-30	53155.9	-5698.2	ACS/HRC	F555W	1200.0	19.432	0.005	25.886	9776	Richstone
2006-01-26	53761.4	-5092.6	ACS/HRC	F330W	1200.0	19.271	0.005	25.728	10548	Gonzalez-Delgado
2008-01-04	54469.8	-4384.2	WFPC2	F555W	2000.0	19.409	0.009	25.965	11171	Crotts
2008-01-04	54469.9	-4384.1	WFPC2	F439W	1000.0	19.454	0.022	24.502	11171	Crotts
2008-01-04	54469.9	-4384.1	WFPC2	F380W	1000.0	19.449	0.019	24.824	11171	Crotts
2008-01-04	54469.9	-4384.1	WFPC2	F702W	1000.0	19.614	0.013	25.512	11171	Crotts
2008-01-04	54470.0	-4384.1	WFPC2	F791W	1000.0	19.712	0.021	24.920	11171	Crotts
2009-11-12	55147.1	-3707.0	WFC3/UVIS	F775W	270.0	19.734	0.010	24.951	11646	Crotts
2009-11-12	55147.1	-3706.9	WFC3/UVIS	F475W	970.0	19.326	0.005	27.050	11646	Crotts
2009-11-12	55147.1	-3706.9	WFC3/UVIS	F555W	970.0	19.422	0.005	27.040	11646	Crotts
2018-02-04	58153.7	-700.6	WFC3/UVIS	F814W	500.0	19.849	0.007	25.252	15133	Erwin
2018-02-04	58153.7	-700.3	WFC3/UVIS	F475W	700.0	19.328	0.005	26.500	15133	Erwin
2018-02-04	58153.8	-700.3	WFC3/IR	F160W	596.9	20.133	0.007	24.627	15133	Erwin
2019-05-23	58626.8	-227.2	ACS/WFC	F814W	2128.0	19.823	0.004	26.526	15645	Sand
2020-01-29	58877.9	23.9	WFC3/UVIS	F814W	836.0	15.821	0.004	25.695	15654	Lee
2020-01-29	58877.9	23.9	WFC3/UVIS	F438W	1050.0	16.783	0.004	26.150	15654	Lee
2020-01-29	58877.9	23.9	WFC3/UVIS	F336W	1110.0	18.453	0.004	26.286	15654	Lee
2020-01-29	58877.9	23.9	WFC3/UVIS	F275W	2190.0	19.114	0.005	26.535	15654	Lee
2020-01-29	58877.9	23.9	WFC3/UVIS	F555W	670.0	16.421	0.004	26.426	15654	Lee
2020-03-15	58923.6	69.6	WFC3/UVIS	F814W	836.0	16.943	0.004	25.672	15654	Lee
2020-03-15	58923.6	69.6	WFC3/UVIS	F438W	1050.0	17.770	0.004	26.177	15654	Lee
2020-03-15	58923.6	69.6	WFC3/UVIS	F336W	1110.0	18.928	0.005	26.150	15654	Lee
2020-03-15	58923.6	69.6	WFC3/UVIS	F275W	2190.0	19.215	0.005	26.350	15654	Lee
2020-03-15	58923.6	69.6	WFC3/UVIS	F555W	670.0	17.372	0.004	26.283	15654	Lee
2020-05-21	58990.6	136.6	WFC3/IR	F110W	1211.8	19.853	0.005	25.873	16075	Jacobson-Galán
2020-05-21	58990.6	136.6	WFC3/IR	F160W	1211.8	20.050	0.006	25.088	16075	Jacobson-Galán
2020-05-21	58990.7	136.6	WFC3/UVIS	F814W	900.0	18.984	0.005	25.943	16075	Jacobson-Galán
2020-05-21	58990.7	136.6	WFC3/UVIS	F555W	1500.0	19.027	0.004	27.071	16075	Jacobson-Galán
2021-02-21	59267.0	412.9	WFC3/UVIS	F625W	780.0	19.475	0.005	26.231	16179	Filippenko
2021-02-21	59267.0	413.0	WFC3/UVIS	F438W	710.0	19.244	0.005	25.931	16179	Filippenko

NOTE—Apparent magnitudes are presented in the *AB* photometric system and have not been corrected for host extinction. Rows corresponding to pre-explosion photometry are shaded violet. Phase is given relative to time of explosion (MJD = 58854.0).



2.2. Ground-Based Optical Photometry

We observed SN 2020oi with the Las Cumbres Observatory Global Telescope Network (LCO) 1m telescopes and LCO imagers from 8 Jan. to 5 Feb. 2020 in $g'r'i'$ bands. We downloaded the calibrated BANZAI (McCully et al. 2018) frames from the Las Cumbres archive and re-aligned them using the command-line blind astrometry tool `solve-field` (Lang et al. 2010). The images were also recalibrated using DoPhot photometry (Schechter et al. 1993) and PS1 DR2 standard stars observed in the same field as SN 2020oi in gri bands (Flewelling et al. 2020). We then stacked $g'r'i'$ -band frames obtained from 31 Jan. to 7 Feb. 2021 as templates and reduced them following the same procedure using SWarp (Bertin 2010). The template images were subtracted from all science frames in hotpants (Becker 2015), and finally we performed forced photometry of SN 2020oi on all subtracted frames using DoPhot with a point-spread function (PSF) fixed to the instrumental PSF derived in each science frame.

SN 2020oi was also observed with the Nickel 1m telescope at Lick Observatory, Mt. Hamilton, California in conjunction with the Direct $2k \times 2k$ camera ($6.8' \times 6.8'$) in $BVr'i'$ bands from 31 Jan. to 8 Aug. 2020. All image-level calibrations and analysis were performed in photpipe (Rest et al. 2005; Kilpatrick et al. 2018a) using calibration frames obtained on the same night and in the same instrumental configuration. We then aligned our images using 2MASS astrometric standards in the image frame, then each image was regridded to a corrected frame using SWarp (Bertin 2010) to remove geometric distortion. All photometry was performed using a custom version of DoPhot (Schechter et al. 1993) to construct an empirical PSF and perform photometry on all detected sources. We then calibrated each frame using PS1 DR1 sources (Flewelling et al. 2020) in ri bands and transformed to BV bands using transformations in Tonry et al. (2012).

Observations of SN 2020oi were also obtained with the Thacher 0.7m telescope located at Thacher Observatory, Ojai, California from 14 Jan. to 21 Dec. 2020 in $griz$ bands. The imaging reductions followed the same procedure described above for our Nickel reductions and in Dimitriadis et al. (2019).

We further observed SN 2020oi with the Swope 1m telescope at Las Campanas Observatory, Chile starting on 21 Jan. 2020 through 15 Mar. 2020 in $uBVgri$ bands. Our reductions followed a procedure similar to the one outlined above for the Nickel telescope and described in further detail in Kilpatrick et al. (2018b).

In addition to the photometry listed above, we include observations obtained from the forced-photometry service (Masci et al. 2019) of the Zwicky Transient Facility (ZTF; Bellm et al. 2019b; Graham et al. 2019). These data, which begin on 7 Jan. 2020 ($\delta t = 2$ days) and continue through 26 April 2020 ($\delta t = 111$ days), were obtained using the Palo-

mar 48-inch telescope and reduced according to the methods outlined in Bellm et al. (2019a).

2.3. Swift Ultraviolet Observations

To obtain ultraviolet (UV) photometry for SN 2020oi, we leverage the extensive observations made of M100 by the Neil Gehrels *Swift* Observatory (Gehrels et al. 2004). The earliest of these was obtained in November 2005. The follow-up campaigns of SN 2006X and SN 2019ehk, acquired with the Ultraviolet Optical Telescope (UVOT; Roming et al. 2005), provide excellent UV and UBV -band template images for SN 2020oi, spanning a total of 22 pre-explosion epochs. Indeed, the first 2 post-explosion UVOT epochs come from the follow-up campaign of SN 2019ehk, which serendipitously observed SN 2020oi only ~ 2.45 days after explosion. Observations were collected for SN 2020oi from 2 to 53 days post-explosion.

We performed aperture photometry with the `uvotsource` task within the HEASOFT v6.22⁵, following the guidelines in Brown et al. (2009) and using an aperture of $3''$. Using the 22 pre-explosion epochs obtained, we have estimated the level of contamination from the host-galaxy flux. In doing so, we assume that excess flux contributions from the progenitor system (as in the case of outbursts or flares), if present, are negligible. This assumption is supported by our measurements of a consistent flux at the location of SN 2020oi across all pre-explosion observations. As a result, we averaged the photon count-rate across the 22 epochs for each filter and then subtracted this from the count rates in the post-explosion images, following the prescriptions in Brown et al. (2014).

To further constrain the host-galaxy contamination within our UVOT images, we perform the same aperture photometry described above at three other locations along the star-forming ring of M100 and equidistant from the nucleus. After host-galaxy subtraction, we find an unexplained flux increase at the same post-explosion epoch across all apertures. It is likely that this is a systematic effect in the *Swift* instrumentation, but at present we are unable to validate this hypothesis. To eliminate the possibility of contaminating our photometry with systematics at other epochs, and because of the strong UV contamination from the M100 nucleus, we have replaced our *Swift* photometry with upper limits derived prior to host subtraction.

We present our complete optical and ultraviolet light curve for the explosion in Figure 2, where we have removed all observations with photometric uncertainties above 0.5 mag. Our full photometric dataset is listed in Table 7.

⁵ We used the calibration database (CALDB) version 20201008.

2.4. Chandra X-ray Observations

We obtained deep X-ray observations of SN 2020oi with the Advanced CCD imaging spectrometer (ACIS) instrument onboard the *Chandra X-ray Observatory* (CXO) on February 15, 2020 and March 13, 2020, 40 and 67 days since explosion, respectively (PI Stroth, IDs 23140, 23141) under an approved DDT program 21508712. The exposure time of each of the two observations was 9.95 ks, for a total exposure time of 19.9 ks. These data were then reduced with the CIAO software package (version 4.13; [Fruscione et al. 2006](#)), using the latest calibration database CALDB version 4.9.4. As part of this reduction, we have applied standard ACIS data filtering.

We do not find evidence for statistically significant X-ray emission at the location of the SN in either observations or in the co-added exposure. Using Poissonian statistics we infer a 3σ count-rate limit of $\sim 4.02 \times 10^{-4} \text{ c s}^{-1}$ and $\sim 5.02 \times 10^{-4} \text{ c s}^{-1}$ for the two epochs of CXO observation (0.5 - 8 keV). The Galactic neutral hydrogen column density in the direction of the transient is $N_{\text{H} \text{ MW}} = 1.97 \times 10^{20} \text{ cm}^{-2}$ ([Kalberla et al. 2005](#)). Assuming a power-law spectral model with spectral photon index $\Gamma = 2$, the above count-rate limits translate to 0.3-10 keV unabsorbed flux limits of $F_x < 6.3 \times 10^{-15} \text{ erg s}^{-1} \text{ cm}^{-2}$ (first epoch), and $F_x < 7.9 \times 10^{-15} \text{ erg s}^{-1} \text{ cm}^{-2}$ (second epoch). We note the presence of diffuse soft X-ray emission from the host galaxy at the SN site, which prevents us from achieving deeper limits on the X-ray emission of the explosion.

2.5. Optical Spectroscopy

We have obtained 12 spectra from $\delta t \approx 3.3$ to $\delta t \approx 41.0$ days post-explosion. Two spectra, including the classification spectrum ($\delta t \approx 3.3$ days from explosion), were obtained with the Goodman High Throughput Spectrograph ([Clemens et al. 2004](#)) at the Southern Astrophysical Research (SOAR) Telescope. Six were obtained with the FLOYDS spectrograph on the Faulkes 2m telescopes of the Las Cumbres Observatory Global Telescope Network (LCOGT; [Brown et al. 2013](#)), two with the Low-Resolution Imaging Spectrometer (LRIS; [Oke et al. 1995](#)) on the Keck I telescope, and two with the Kast spectrograph ([Miller & Stone 1993](#)) on the 3m Shane telescope at Lick Observatory. The FLOYDS spectra were reduced using a dedicated spectral reduction pipeline⁶ and the remaining ones with standard IRAF/PYRAF⁷ and python routines ([Siebert et al. 2020a](#)). All of the spectral images were bias/overscan-subtracted and flat-fielded, with the wavelength solution derived using arc lamps and the final flux calibration and telluric line removal performed using

spectro-photometric standard star spectra ([Silverman et al. 2012](#)). We provide a summary of our full spectral sequence, which spans 38 days of explosion, in Table 2, and plot each obtained spectrum in Figure 3.

In addition to those described above, two optical spectra were obtained that did not contain obvious SN emission. The first was obtained using the Keck Observatory’s Low Resolution Imaging Spectrometer (LRIS) on December 10th, 2020, ~ 336 days from the explosion’s maximum brightness in *r* band. After reducing the data, it was determined that the spectrum was dominated by galaxy light. The second spectrum, which was obtained with the FLOYDS spectrograph on the Faulkes 2m telescope of the LCOGT in Siding Springs, Australia, was affected by poor seeing.

3. HOST GALAXY EXTINCTION

We estimate the host-galaxy extinction along the line of sight to the SN first using the empirical relation between the reddening and the equivalent width of the spectrum’s Na $\lambda\lambda 5889, 5895$ doublet ([Poznanski et al. 2012](#)). Using our de-redshifted high resolution Keck/LRIS spectrum obtained on January 27, a pseudo-continuum is defined as a line at the edges of the absorption feature and the spectrum is then normalized at the feature’s position. We then fit the sodium doublet, which we approximate as two Gaussians with their widths forced to be the same and their relative strengths constrained according to their oscillator strengths (obtained from the National Nuclear Data Center⁸). This process is repeated 10,000 times for different choices of the pseudo-continuum. We estimate a combined equivalent width of $0.88 \pm 0.05 \text{ \AA}$, corresponding to a host reddening of $E(B - V) = 0.15 \pm 0.03 \text{ mag}$ (using equation 9 from [Poznanski et al. 2012](#)). This is comparable to the value provided by [Horesh et al. \(2020\)](#), who estimates $E(B - V) = 0.14 \pm 0.05 \text{ mag}$ of reddening using this procedure. Assuming $R_V = 3.1$, this corresponds to a *V* band extinction of $A_V \approx 0.47$.

We additionally estimate the line-of-sight host-galaxy reddening by comparing the observed color evolution of SN 2020oi during the first 20 days following peak luminosity to the type-Ic color templates provided in [Stritzinger et al. \(2018\)](#). First, we sample a range of A_V and R_V values across a uniformly-spaced grid spanning [0.0, 1.0] mag and [1.0, 6.0], respectively. By interpolating the spectra spanning this range in phase, we obtain extinction corrections for each photometric band and calculate the χ^2 value of our corrected color curve. Because we find R_V to be poorly constrained from our photometry, we choose A_V to be the value with the smallest χ^2 value for a fixed $R_V = 3.1$ (corresponding to a Galactic extinction curve). We note that infrared observa-

⁶ https://github.com/LCOGT/floyds_pipeline

⁷ IRAF is distributed by the National Optical Astronomy Observatories, which are operated by the Association of Universities for Research in Astronomy, Inc., under cooperative agreement with the National Science Foundation.

⁸ <https://www.nndc.bnl.gov/>

Table 2. Optical Spectroscopic Observations of SN 2020oi

Date (UT)	MJD	Phase (days)	Telescope	Instrument	Wavelength Range (Å)
2020-01-09	58857.3	+3.3	SOAR	Goodman	4000–9000
2020-01-12	58892.0	+6.6	Shane	KAST	3800–9100
2020-01-16	58864.6	+10.6	Faulkes North	FLOYDS	4800–10000
2020-01-20	58868.6	+14.6	Faulkes North	FLOYDS	4800–10000
2020-01-22	58870.5	+16.5	Faulkes North	FLOYDS	4800–10000
2020-01-24	58872.4	+18.4	Faulkes North	FLOYDS	4800–10000
2020-01-27	58875.0	+21.0	Keck I	LRIS	3200–10800
2020-01-31	58879.4	+25.4	Faulkes North	FLOYDS	4800–10000
2020-02-01	58880.3	+26.3	SOAR	Goodman	4000–9000
2020-02-01	58880.4	+26.4	Faulkes North	FLOYDS	4800–10000
2020-02-13	58892.0	+38.0	Shane	KAST	3500–11000
2020-02-16	58895.0	+41.0	Keck I	LRIS	3200–10800

NOTE—Phase is given relative to time of explosion (MJD = 58854.0).

tions of SN 2020oi are needed to conclusively determine R_V (Stritzinger et al. 2018).

We find a best-fit host-galaxy extinction of $A_V = 0.35$ mag for $R_V = 3.1$, corresponding to a reddening of $E(B - V) = 0.11$ mag. We estimate the error on A_V to be 0.03 mag by calculating the standard deviation of the best-fit values across each of our sampled R_V values. We adopt this value as our host-galaxy extinction instead of the value derived from the Na doublet fitting due to the large dispersion associated with the latter relationship. A slightly higher host reddening of $E(B - V) = 0.13$ mag was adopted by Horesh et al. (2020) from a comparison of the same color templates as we have used. We also report a Galactic reddening value of $E(B - V) = 0.0227 \pm 0.0002$ mag in the direction of the SN based upon the maps of Schlafly & Finkbeiner (2011), leading to a combined reddening of $E(B - V) = 0.133 \pm 0.03$ mag. This is consistent with the 0.153 mag of total reddening reported by Horesh et al. (2020), who find a comparable Galactic value of $E(B - V) = 0.023$ mag in the direction of M100. In the following sections, we adopt a combined reddening of $E(B - V) = 0.133$.

4. BOLOMETRIC LIGHT CURVE FITTING

To consolidate our panchromatic observations obtained at different epochs into a consistent bolometric light curve, we seek to construct a non-parametric model for the photometric evolution of the explosion in each filter using Gaussian Process Regression (GPR; Rasmussen 2006). GPR is an approach to functional approximation that assumes that observations are realizations sampled from a latent function with Gaussian noise. The model is constrained by a kernel func-

tion that describes the similarity between observations using a length scale over which our observations are correlated. By conditioning a chosen kernel, which characterizes our prior, on the observations, we can generate a posterior distribution for a class of functions that describe the data. This procedure can additionally consider a mean model for the observations, and this further conditions the subsequent model predictions. We use the GPR implementation in George (Ambikasaran et al. 2015).

The mean model we construct for our light curve in each band must be sensitive to the early-time bump observed within the first five days, but insensitive to late-time galactic contamination from the bright nucleus. We use SciPy’s `splrep` function, which determines a basis (B-) spline representing a one-dimensional function, to construct this model (Dierckx 1995). The basis calculated by this method is determined both by the degree of the spline fit and the weights imposed on each observation. The observations with highest relative weighting most tightly constrain the B-spline, allowing us to determine the light-curve features captured in the mean model and those smoothed in it.

First, we calculate a B-spline for our r -band photometry with polynomial order five. Observations taken before MJD 58858.0 ($\delta t \approx 4.0$ days) are given a weight of 60, those within 3 days of the r -band peak are given a weight of 50, and all other points are given a weight of 10. We then construct a mean model for our GPR according to the following equation:

$$\bar{m}(t) = \begin{cases} B(t + \alpha) + \beta + \gamma & \text{for } t < 58858.0 \\ B(t + \alpha) + \beta, & \text{for } t \geq 58858.0 \end{cases} \quad (1)$$

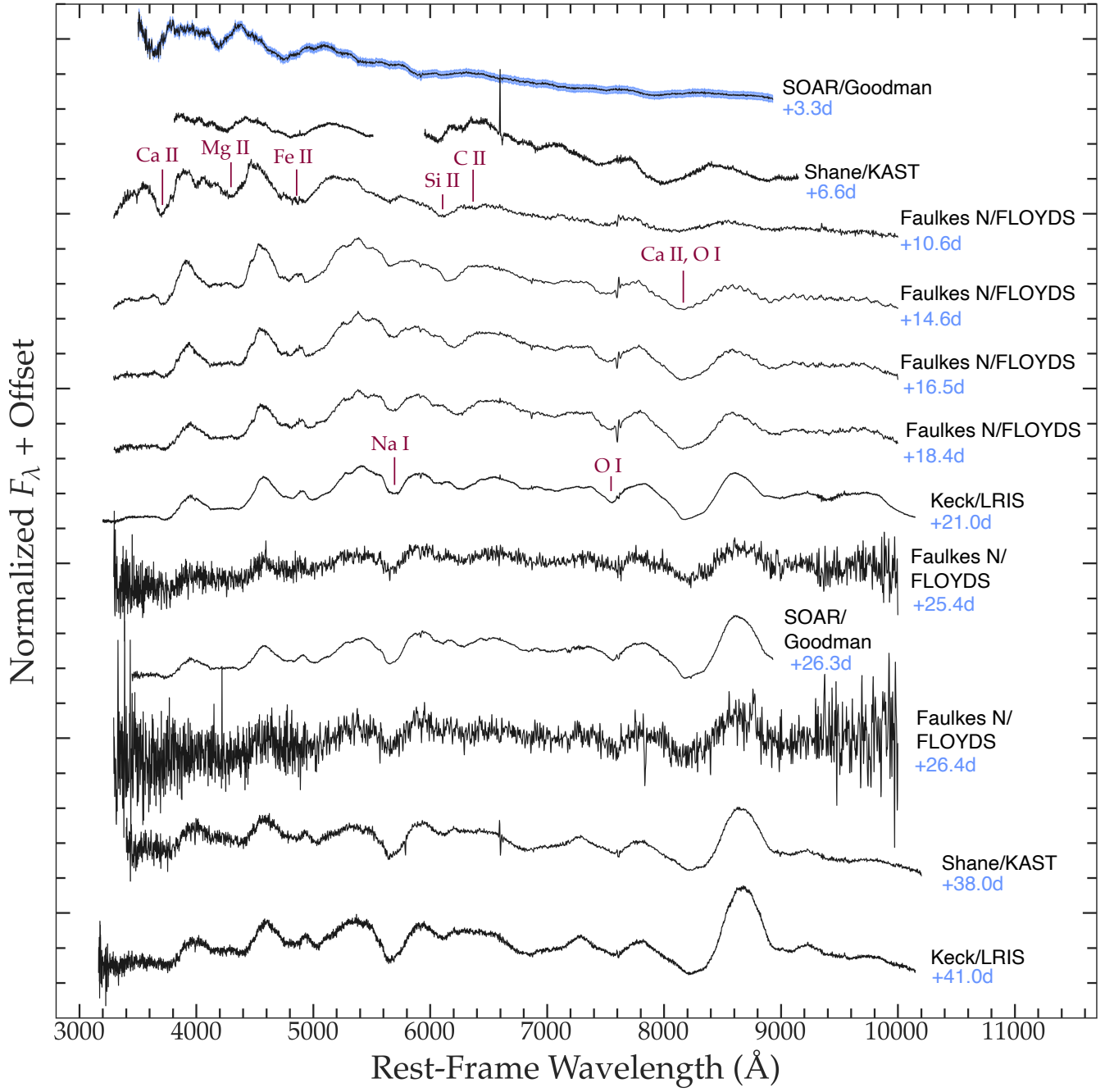


Figure 3. The full sequence of optical spectra obtained for SN 2020oi. Spectrographs used for observations are listed at right, along with the phase of the spectra relative to the time of explosion. Prominent absorption lines are listed in red and the spectrum taken within one day of the early-time photometric excess is highlighted in blue at top.

Where t is the time in MJD, B is the r -band B-spline interpolation function, α is a parameter that shifts the entire curve forward in phase, β is a parameter that shifts the model in magnitude, and γ is a parameter that determines the height of the early-time brightness excess relative to the rest of the light curve. Although this model was constructed from only our r -band photometry, it serves as the mean model for all our passbands. The parameters described above allow the model to account for the difference in light curve properties between r and the other fitted bands.

These three free parameters, in addition to a fourth to account for the intrinsic photometric dispersion, are then fit in each band independently using an exp-sine-squared kernel of length-scale $\Gamma = 0.9$ and period $\ln(P) = 5$ to smoothly predict the rise and decay of the luminosity. The period was chosen to be approximately twice the duration of the photometry (~ 70 days), ensuring that the rise and fall to the light curve corresponds to the first half-wavelength of the model. The value for Γ was determined empirically; larger Γ values resulted in a mean model that overfit the observations and preserved small-scale correlations. This results in a set of 500 interpolated observations in *UBgVriz* bands spanning MJD 58854-58919 (corresponding to the first 65 days of the explosion). We present the posterior distributions obtained from this method in Figure 2.

Next, we use the *Superbol* package⁹ (Nicholl 2018) to calculate the integrated bolometric luminosity of SN 2020oi. After shifting to the rest frame and correcting for the combined Milky Way and host-galaxy extinction, we model the explosion at each epoch as a black-body (a good approximation during the photospheric phase owing to the optically thick ejecta) and use the *curve_fit* routine within the Python package *Scipy* to determine the photospheric temperature and radius that best describe each interpolated observation. These curves are then integrated to account for the unobserved far-UV and near-IR flux from the event and calculate the bolometric luminosity at each epoch. We present the final bolometric light curve in Figure 4, along with those reported by Lyman et al. (2016) and Taddia et al. (2018) for previous SN Ic and SN Ic-BL events.

We find SN 2020oi to be less luminous than nearly all previous SNe Ic from Lyman et al. (2016) for the majority of its evolution. Roughly 10 days before peak, the explosion is the second-dimmest type-Ic event for which data are available. Similarly, at the end of the photospheric phase ($t \approx 30$ days, after which point the SN ejecta can no longer be approximated as a black-body due to its decreasing opacity as it expands), SN 2020oi is dimmer than all but two SN Ic reported (the tail of the SN 1994I is slightly less luminous, although the

extinction in the direction of SN 1994I remains highly uncertain; see Sauer et al. 2006). Interestingly, although we find the event to be dimmer than most other SNe Ic at early- and late-times, at peak SN 2020oi rises to within less than half a standard deviation of the mean peak luminosity for the SN Ic sample.

An event with a lower luminosity pre- and post-maximum but reaching comparable brightness at peak to other type-Ic explosions must necessarily exhibit rise and decline rates greater than other type-Ic events. Indeed, as is reported in Horesh et al. (2020) and visible in Fig. 4, the slope of the bolometric luminosity of SN 2020oi after maximum is steeper than most previously observed SNe Ic. The overall bolometric evolution can be seen to roughly match that of SN 1994I. We can parameterize the decline rate of SN 2020oi by $\Delta m_{15, \text{bol}}$, the difference in the absolute bolometric magnitude from peak brightness to 15 days following peak. We find a value of $\Delta m_{15, \text{bol}} \approx 1.63 \pm 0.14$, higher than any other stripped-envelope SN reported by either Lyman et al. (2016) or Taddia et al. (2018) and ~ 1 mag higher than the median for type-Ic events. The wide scatter in SN Ic decline rates was reported in Li et al. (2011) in a study of eight events, although of the SNe considered only the decline of SN 1994I was characterized as rapid. Larger type-Ic samples are needed to determine whether these rapidly-declining events are intrinsically rare. We present the peak absolute magnitudes and $\Delta m_{15, \text{bol}}$ values for SN 2020oi and other stripped-envelope events in Figure 5.

4.1. Photospheric Properties of SN 2020oi

We now leverage our best-fit black-body model from *Superbol* to estimate the radius and temperature of the photosphere of the SN as it explodes, which we present in Figure 6 for the first 60 days of the explosion. Due to the unknown nature of the flux excess, we consider only the radius and temperature estimates following $\delta t \sim 3$ days from the time of explosion.

Following the observed flux excess, the first photospheric radius observed is $R = 5.1 \pm 0.9 \times 10^{14}$ cm at $\delta t \approx 3$ days from explosion. The corresponding effective temperature at this epoch is $T_{\text{eff}} = 6300 \pm 600$ K. As the ejecta expands, the temperature of the ejecta probed by the photosphere decreases and so does its scattering opacity. At $\delta t = 11.7$ days, the photosphere radius reaches a maximum of $2.1 \pm 0.6 \times 10^{15}$ cm, or 140 AU, and a temperature of $T_{\text{eff}} = 5800 \pm 600$ K. The opacity of the external layers of expanding ejecta has now decreased sufficiently to allow central radiation to escape, causing the photosphere to recede inward. Past $\delta t = 11.7$ days, the radius of the photosphere decreases gradually until $\delta t = 20$ days (10 days following peak luminosity) and then remains roughly constant for the following 30 days considered.

⁹ <https://github.com/mnicholl/superbol>

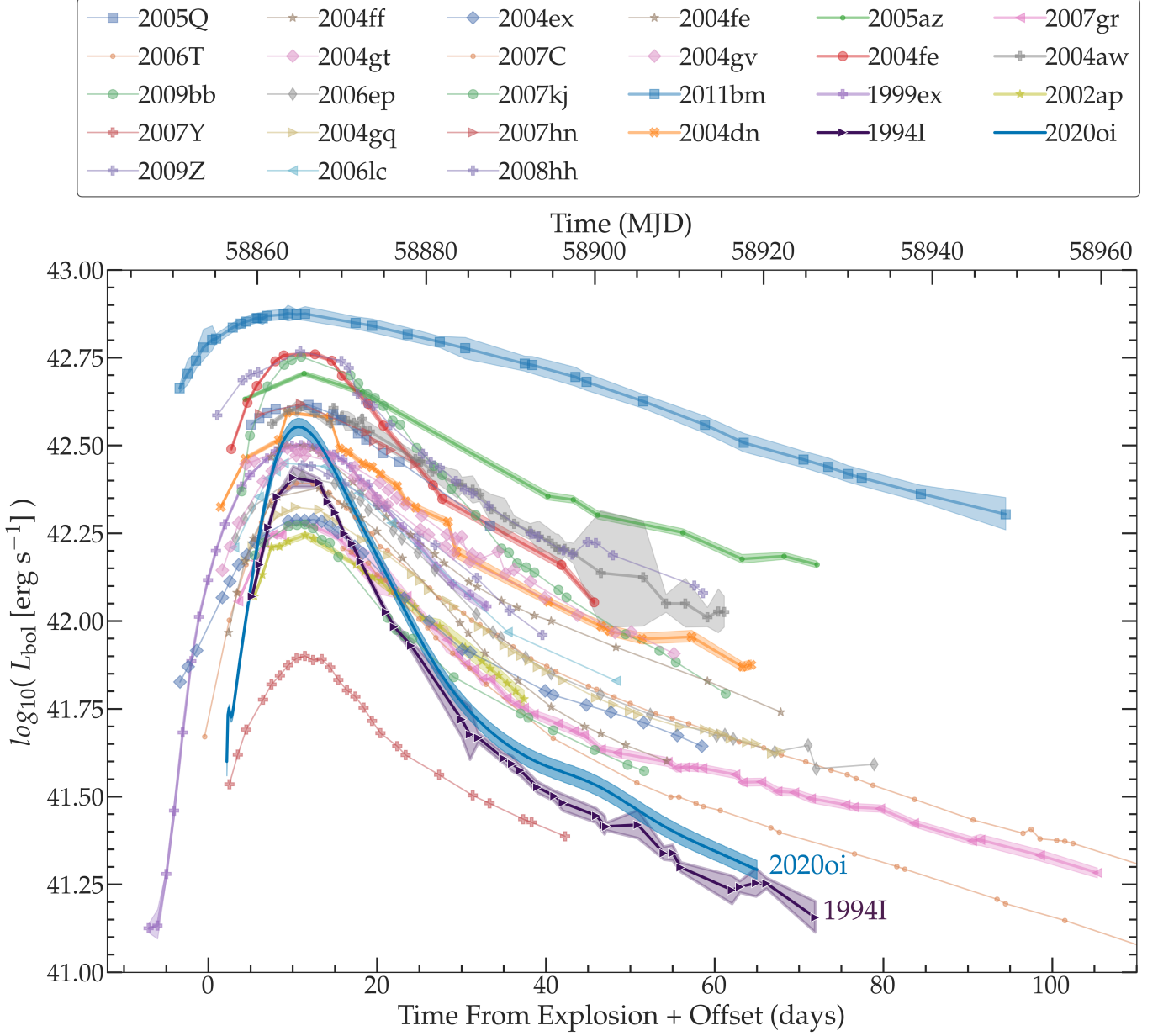


Figure 4. The bolometric light curve for SN 2020oi (blue), plotted alongside the type-Ic/Ic-BL SN samples from [Lyman et al. \(2016\)](#) and [Taddia et al. \(2018\)](#). Light curves have been aligned at peak and the shaded regions correspond to $1-\sigma$ confidence intervals for the SNe in [Lyman et al. \(2016\)](#), which incorporate only uncertainty in the bolometric corrections for each event. Uncertainties in distance modulus and extinction along each line of sight are not shown and may affect this comparison. For clarity, we plot only SNe with pre-maximum observations. The rise and decline rate of SN 2020oi is similar to that of the characteristic type-Ic event SN 1994I (shown in violet), which is identified as a rapidly declining event in [Lyman et al. \(2016\)](#). SN 2020oi appears more luminous than SN 1994I, but unaccounted-for extinction toward SN 1994I may also account for this difference ([Richmond et al. 1996](#)). The bolometric contribution from the SN 2020oi early-time bump can be seen in the first day of observations.

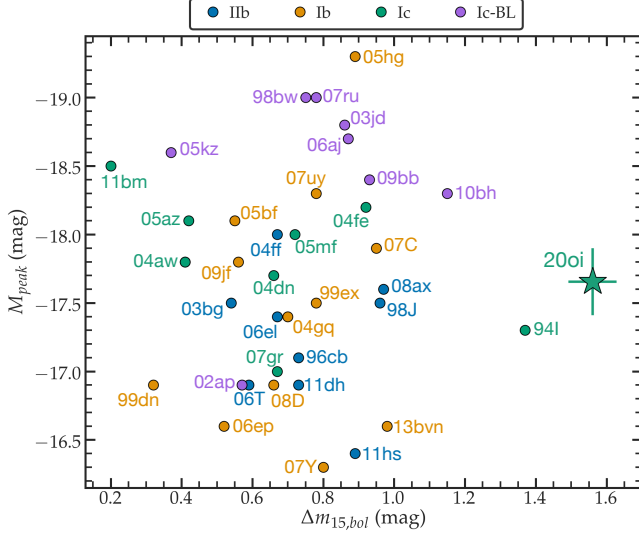


Figure 5. Light curve absolute magnitude at peak (M_{peak}) and linear decline rates ($\Delta m_{15,bol}$) for stripped-envelope SNe from Lyman et al. (2016). The location of SN 2020oi is denoted by a star at right. Error in the value of $\Delta m_{15,bol}$ is propagated from photometric uncertainties, and error in M_{peak} combines uncertainty in event photometry, distance, and extinction. The decline rate for SN 2020oi from peak to 15 days following is ~ 1 mag higher than the median for type-Ic events shown and ~ 0.3 mag higher than the decline rate of the next-closest type-Ic event, SN 1994I (although the decline of SN 1994I may have been higher than is shown here due to uncertainty in extinction estimates in the direction of the SN; see Richmond et al. 1996). Figure adapted from Lyman et al. (2016).

For comparison, we have also estimated the photospheric properties of the explosion as derived from the classification spectrum and the five spectra proceeding it. At each spectral epoch, we obtain an upper limit on the photospheric velocity from the minimum of the Si II $\lambda 6355$ line. Assuming homologous expansion, the radius is then estimated as $R(\delta t) = v_{\text{exp}} \delta t$. We caution that this estimate is highly sensitive to our estimated time of explosion. The effective temperature is calculated from the bolometric luminosity as

$$T_{\text{eff}}(\delta t) = \left(\frac{L_{\text{bol}}(\delta t)}{4\pi R_{\text{ph}}(\delta t)^2 \sigma_{\text{SB}}} \right)^{1/4} \quad (2)$$

where σ_{SB} is the Stefan-Boltzmann constant. We find systematically higher temperatures and lower radii using the spectroscopic indicators for the epochs studied, although the overall evolution is similar.

We also plot the best-fit spectroscopic estimates of the photospheric temperature and radius for the similar type-Ic SN 1994I in Fig. 6. We note a more gradual temperature evolution for SN 2020oi compared to SN 1994I when derived from the event photometry; this difference is less prominent in the spectroscopic indicators, and may be a reflection of the method used rather than an intrinsic difference in the two explosions.

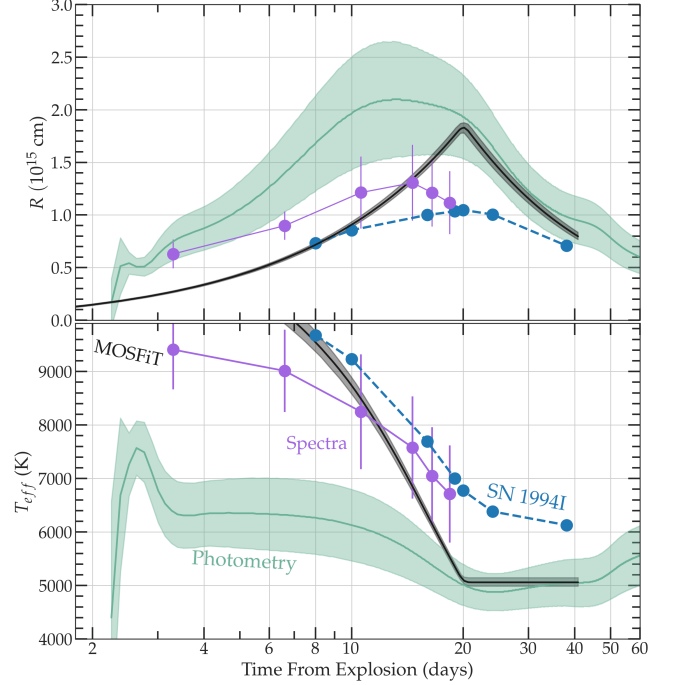


Figure 6. Temperature and radius estimates of the SN photosphere from black-body fits to the photometry at each interpolated epoch in green. Spectra-derived black-body values for SN 2020oi are shown in violet. The spectra-derived photospheric properties of the type-Ic SN 1994I (Sauer et al. 2006) are shown as blue points. The photospheric properties of the best-fit MOSFiT model (described in §5.3) are given in black. Shaded regions denote $1\text{-}\sigma$ confidence intervals. The difference between spectroscopic and photometric estimates of these properties are not physical, but instead reflect the approximate nature of each indicator.

The evolution provided by the black-body fits excluding the early excess closely mimics that of the stripped-envelope SNe considered in both Prentice et al. (2019) and Taddia et al. (2018). The maximum photospheric radius for SN 2020oi is in agreement with the range reported by Taddia et al. (2018) of $0.6\text{--}2.4 \times 10^{15} \text{ cm}^2$, and the SNe in both samples also exhibit a maximum photospheric temperature of $T = 4000\text{--}8000 \text{ K}$ followed by a cooling phase to roughly $\sim 5000 \text{ K}$ 10 days following maximum light. We similarly note an apparent increase in temperature following this leveling off, as is reported in Prentice et al. (2019) and Taddia et al. (2018); however, this is most likely nonphysical and instead a consequence of non-thermal effects following the photospheric phase of the explosion (as we mention above, the explosion is not well-characterized by a black-body following $\delta t \approx 30$ days).

5. EXPLOSION KINETICS FROM BOLOMETRIC FITTING

The rapid brightening of the explosion as observed in Fig. 4 indicates a short diffusion time for photons produced by the radioactive decay of synthesized ^{56}Ni and ^{56}Co . We

derive this timescale along with other explosion parameters for the SN using three independent methodologies, which we describe and compare below.

5.1. The Arnett (1982) Model Applied to the Bolometric Light Curve of SN 2020oi

In this section, we use a modified one-component Arnett model (Arnett 1982) to constrain $M_{\text{Ni}56}$, the mass of ^{56}Ni synthesized in the explosion; t_{exp} , the time of explosion; and t_d , the diffusion timescale. We further derive The total kinetic energy E_k and the total mass ejected in the explosion M_{ej} from these estimates. The Arnett model contains a number of assumptions which are applicable during the photospheric phase of most standard SN explosions ($t \lesssim 30$ days): that the ejecta undergo homologous expansion and are both optically thick and radiation-pressure dominated; that the energy density of the ejecta is most concentrated at its center; and that the explosion exhibits spherical symmetry. This formalism has proven valuable for characterizing the bolometric evolution of both type-Ia SNe and stripped-envelope events (see e.g., Phillips et al. 2007; Foley et al. 2009; Scalzo et al. 2010; Drout et al. 2011; Lyman et al. 2016; Sahu et al. 2018; Barbarino et al. 2020). In this work, we adopt the modified Arnett model developed by Valenti et al. (2008) in which the emission of the SN is assumed to be dominated by the radioactive decay of ^{56}Ni into ^{56}Co early in the explosion and from ^{56}Co to ^{56}Fe at late times.

We iteratively fit our bolometric light curve excluding the early-time flux excess, first for t_d and next for t_{exp} . This procedure requires an estimate of the ejecta velocity at peak bolometric luminosity, which we estimate spectroscopically using the Si line to be $v_{\text{exp}} = -12750 \pm 250 \text{ km s}^{-1}$. We limit our search for t_{exp} to within 5 days of our earliest observation but no later than MJD 58855.54 (the date of the first explosion detection) and our search for t_d to (0, 20) days. We also assume an optical opacity of $\kappa_{\text{opt}} = 0.07 \text{ cm}^2 \text{ g}^{-1}$ as is typically adopted for hydrogen-poor CCSNe (Taddia et al. 2016). Using this routine, we find a diffusion timescale for the event of $t_d = 8.41 \pm 0.28$ days and a predicted time of explosion of $t_{\text{exp}} = 58855.4 \pm 0.2$ (MJD). The uncertainties reported are propagated from our photometric and spectroscopic uncertainties, and do not include uncertainty in the host-galaxy extinction or the distance to the SN. From this procedure, we further derive a total kinetic energy of $E_k = 0.97 \pm 0.13 \times 10^{51} \text{ erg}$, comparable to the estimate of $1 \times 10^{51} \text{ erg}$ provided in Rho et al. (2021).

Because the unusual early-time photometric evolution of the explosion can bias the Arnett estimates for t_0 toward later epochs, we derive the time of explosion by fitting the SN rise (excluding epochs of optical and UV excess) to an expanding-fireball model. We elaborate on this model in §9. We impose an assumption of zero flux at MJD 58852.55 corresponding

to the epoch of the last r -band non-detection from ZTF. From our best-fit model, we predict an explosion time of MJD 58854.0 ± 0.3 . We adopt this value throughout this work. We note that this estimate is consistent with the MJD date of 58854.0 ± 1.5 estimated by Rho et al. (2021) and that of 58854.50 ± 1.46 predicted by Horesh et al. (2020). Further, taking the mean between the last ZTF non-detection and the time of the first explosion detection (on MJD 58855.54), we obtain a comparable MJD date of 58854.05.

5.2. Constraining the Ejecta Mass of SN 2020oi Using the Khatami and Kasen (2019) Formalism

In addition to the Arnett prescription, we use the model described in Khatami & Kasen (2019) to constrain M_{ej} and $M_{\text{Ni}56}$. Although the Arnett model provides an estimate for the mass of synthesized ^{56}Ni , the model assumes that the peak luminosity of the event is equal to the heating rate at peak. This ignores radiative diffusion originating from the central engine and extending to the surface of the ejecta, which can lead to the true peak luminosity being underestimated if the heating source is centrally concentrated and overestimated if the heating source is highly mixed. For stripped-envelope supernovae such as the one considered here, this can have a large effect on the reported ^{56}Ni mass (Khatami & Kasen 2019). By parameterizing the degree of mixing for different classes of explosions with a factor β , the Khatami & Kasen model attempts to account for this diffusion and provide a more accurate estimate of the nickel mass.

With an estimate for the peak luminosity of the event L_{peak} , the time of peak light t_{peak} , and the mixing parameter β , $M_{\text{Ni}56}$ can be determined by re-arranging equation A.13 from Khatami & Kasen (2019):

$$M_{\text{Ni}56} = \frac{L_{\text{peak}} \beta^2 t_{\text{peak}}^2}{2 \varepsilon_{\text{Ni}} t_{\text{Ni}}^2} \left(\left(1 - \frac{\varepsilon_{\text{Co}}}{\varepsilon_{\text{Ni}}} \right) \times \right. \\ \left. (1 - (1 + \beta t_{\text{peak}}/t_{\text{Ni}}) e^{-\beta t_{\text{peak}}/t_{\text{Ni}}}) + \right. \\ \left. \frac{\varepsilon_{\text{Co}} t_{\text{Co}}^2}{\varepsilon_{\text{Ni}} t_{\text{Ni}}^2} \left(1 - (1 + \beta t_{\text{peak}}/t_{\text{Co}}) e^{-\beta t_{\text{peak}}/t_{\text{Co}}} \right) \right)^{-1} \quad (3)$$

where $t_{\text{Ni}} = 8.77$ days is the timescale for the radioactive decay of ^{56}Ni into ^{56}Co , $t_{\text{Co}} = 111.3$ days is the timescale for the radioactive decay of ^{56}Co into ^{56}Fe , and ε_{Ni} and ε_{Co} are the amount of energy per unit mass released from these decays. We adopt a value of $\beta = 0.9$ that has been empirically calibrated from a sample of well-studied SNe Ic (Afsariardchi et al. 2020). The diffusion timescale t_d can be calculated from the rise time by numerically solving the equation

$$\frac{t_{\text{peak}}}{t_d} = 0.11 \ln \left(1 + \frac{9t_s}{t_d} \right) + 0.36 \quad (4)$$

and, from the diffusion timescale, the total ejecta mass is then found by

$$M_{\text{ej}} = t_d^2 v_{\text{ej}} \frac{c}{\kappa_{\text{opt}}} \quad (5)$$

As in the Arnett treatment, we derive the kinetic energy from the ejected mass:

$$E_k = \frac{3}{10} M_{\text{ej}} v_{\text{exp}}^2 \quad (6)$$

where v_{exp} is the velocity of the explosion at peak (found spectroscopically with the Si line).

We report a synthesized ^{56}Ni mass of $M_{\text{Ni}56} = 0.08 \pm 0.02 M_{\odot}$ and a total ejecta mass of $M_{\text{ej}} = 0.81 \pm 0.03 M_{\odot}$ from this method. These estimates are slightly higher than the $M_{56\text{Ni}} = 0.07 M_{\odot}$ and $M_{\text{ej}} = 0.7 M_{\odot}$ values reported by [Rho et al. \(2021\)](#), where they are estimated by comparing photometric observations of the event to a library of explosion models. The best-fit values from our one-component Arnett model are $M_{\text{Ni}56} = 0.16 \pm 0.02 M_{\odot}$ and $M_{\text{ej}} = 1.00 \pm 0.08 M_{\odot}$. The larger M_{ej} values derived with the Arnett model is a direct consequence of their distinct treatments of the diffusion timescale; by considering the additional contributions from radiative diffusion, the timescale calculated using the [Khatami & Kasen \(2019\)](#) method is significantly higher than is found using the Arnett method. [Khatami & Kasen \(2019\)](#) also note that the Arnett model yields less-accurate parameter estimates for lower values of $M_{56\text{Ni}}$, in some cases deviating from the true mass by a factor of two (as is shown for the type-II SN 1987A relative to the value determined from late-time light curve fits). Because of the limitations of the Arnett model, we adopt the [Khatami & Kasen \(2019\)](#) estimates for the nickel and ejecta masses, as well as the kinetic energy of the explosion.

The ejected nickel mass estimated for SN 2020oi from both the Arnett and the Khatami & Kasen formalisms is lower than the median for SNe Ic presented in [Anderson \(2019\)](#). Similarly, [Taddia et al. \(2018\)](#) suggest that the mass of nickel synthesized in SN Ic events is $\sim 0.09 - 0.17 M_{\odot}$, and our estimates occupy the lower end of this distribution. Because the radioactive decays $^{56}\text{Ni} \rightarrow ^{56}\text{Co}$ and $^{56}\text{Co} \rightarrow ^{56}\text{Fe}$ are the dominant energy sources powering the emission at early and late times, respectively, this finding is consistent with the low luminosity of the bolometric light curve observed in Fig. 4. The estimated mass of synthesized ^{56}Ni is comparable to the $0.07 M_{\odot}$ value reported for SN 1994I ([Iwamoto et al. 1994a](#)), explaining their similar bolometric evolution. We compare the best-fit explosion parameters for SN 2020oi to other stripped-envelope SNe in Figure 7, and report the derived explosion properties in Table 3.

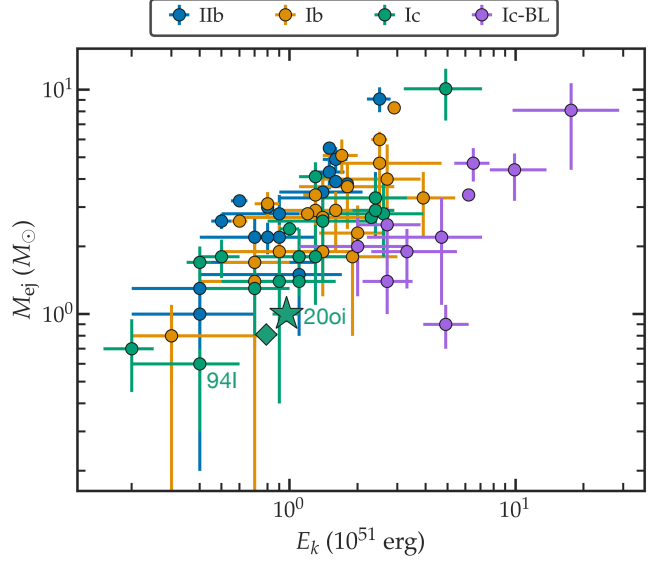


Figure 7. The total ejecta masses and explosion energies for the stripped-envelope SNe in [Lyman et al. \(2016\)](#) and [Taddia et al. \(2018\)](#) derived using a semi-analytic Arnett model ([Arnett 1982](#)). The star denotes the parameter values derived for SN 2020oi in this study using an Arnett model, whereas the diamond denotes the values adopted from the [Khatami & Kasen \(2019\)](#) prescription (see text for details). The location of SN 1994I is labeled bottom left. SN 2020oi was more energetic than the well-studied SN 1994I but the two explosions ejected similar masses of material.

5.3. The MOSFiT type-Ic Model Applied to the Optical/UV Photometry of SN 2020oi

In addition to estimating the properties of SN 2020oi from the bolometric light curve, we use the SN Ic model within the Modular Open Source Fitter for Transients (MOSFiT; [Guillochon et al. 2018](#)) to validate the SN explosion parameters and constrain the photospheric properties of SN 2020oi. In this framework, a forward model for the emission of an explosive transient is constructed by specifying its central engine and emission SED. In the default SN Ic model, energy from ^{56}Ni decay is deposited following the rates provided in [Nadyozhin \(1994\)](#). This produces black-body radiation that diffuses from the SN ejecta according to [Arnett \(1982\)](#). MOSFiT is implemented using a Bayesian framework for iteratively sampling the SN parameter space and approximating the solution with maximum likelihood. As in the models described in previous sections, MOSFiT constrains M_{ej} and $M_{\text{Ni}56}$ (parameterized by the fraction of M_{ej} comprised of nickel, f_{Ni}) and assumes homologous expansion of the ejecta. We additionally solve for the γ -ray opacity κ_{λ} of the ejecta, which controls the degree of trapping of γ -rays generated from ^{56}Ni and ^{56}Co decay; as well as T_{min} , the temperature floor of the model photosphere. We exclude photometry after $\delta t > 30$ days from our fit. We use the dynamic nesting sampling method in *dynesty* ([Speagle 2020](#)), with a burn-in phase of 500 and a chain length

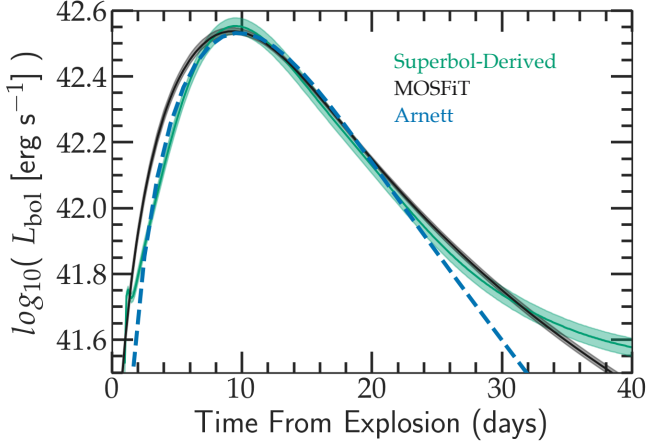


Figure 8. Best-fit bolometric light curve models for the photospheric phase of SN 2020oi. The Arnett model calculated in §5.1 is shown as a blue dashed line, and the black shaded region describes the fit determined using the code MOSFiT (§5.3). The derived bolometric light curve for SN 2020oi is shown in green. Derived parameters are presented in Table 3. The bolometric luminosity of the explosion is not well-described by either model 30 days after explosion due to the rapidly decreasing opacity of the ejecta.

of 2000, to sample our parameter space. We have verified that we obtain comparable results using MCMC sampling with emcee, a Python-based application of an affine invariant Monte Carlo Markov Chain (MCMC) with an ensemble sampler (Foreman-Mackey et al. 2013).

We list our best-fit MOSFiT parameters in Table 3. We also compare the bolometric light curves associated with our MOSFiT and Arnett models in Fig. 8, and present the corner plot from our MOSFiT run in Fig. 9. We have found during this analysis that, by fitting the model band-by-band under the assumption of black-body radiation (as opposed to our Arnett fit to the bolometric light-curve), the MOSFiT model is more sensitive to deviations from black-body. This was particularly evident later in the event’s evolution, where the inclusion of photometry > 30 days from explosion resulted in a best-fit MOSFiT model whose bolometric light-curve was under-luminous relative to that of SN 2020oi.

We can now compare the photospheric evolution of our MOSFiT model to that derived photometrically and spectroscopically. We plot the black-body radius and temperature for the first 60 days of the model in Fig. 6. The temperatures predicted by the model within the first ~ 6 days are higher than those derived from photometry and spectra, but the plateau starting 20 days following explosion is consistent. The photospheric radius suggested by the model is lower than the photometric estimates before 20 days and consistent thereafter.

6. INFERENCES ON THE PRE-EXPLOSION MASS-LOSS HISTORY

The X-ray emission from H-stripped SNe exploding in low-density environments is dominated by Inverse Compton (IC) radiation for $\delta t \lesssim 40$ days (e.g., Chevalier & Fransson 2006). In this scenario, the X-ray emission is generated by the upscattering of seed optical photospheric photons by a population of relativistic electrons that have been accelerated at the SN forward shock. We followed the IC formalism by Margutti et al. (2012) modified for a massive stellar progenitor density profile as in Margutti et al. (2014). Specifically, we assumed a wind-like environment density profile $\rho_{CSM} \propto r^{-s}$ with $s = 2$ as appropriate for massive stars (Chandra 2018), an energy spectrum of the accelerated electrons $N_e(\gamma) \propto \gamma^{-p}$ with $p = 3$ as commonly found from radio observations of Ib/c SNe (e.g., Soderberg et al. 2006b,a,c, 2010) and as observed at late times in SN 2020oi (Horesh et al. 2020), and a fraction of postshock energy into relativistic electrons $\epsilon_e = 0.1$. We further adopted the explosion parameters $M_{ej} = 0.81 M_\odot$ and $E_k = 0.79 \times 10^{51}$ erg inferred from the modeling of the bolometric light curve in §5. Under these assumptions, our deep X-ray upper limits from §2.4 lead to a mass-loss rate limit of $\dot{M} \approx 1.5 \times 10^{-4} M_\odot \text{yr}^{-1}$ for a wind velocity of $v_w = 1000 \text{ km s}^{-1}$.

In an earlier analysis on SN 2020oi by Horesh et al. (2020), radio observations obtained with the Karl G. Jansky Very Large Array (VLA) beginning on day 5 of the explosion (Horesh & Sfaradi 2020) were explained as radiation originating from a shock-wave interaction between the SN ejecta and surrounding circumstellar material. These data were then modeled using the synchrotron self-absorption (SSA) formalism derived in Chevalier (1998). In this model, the microphysics of the interaction are parameterized by the ratio between ϵ_e , the fraction of energy from the shock-wave injected into relativistic electrons; and ϵ_B , the fraction of energy converted to magnetic fields. The best-fit model found by Horesh et al. (2020) suggests a strong departure from equipartition, with $\frac{\epsilon_e}{\epsilon_B} \geq 200$. Further, Horesh et al. (2020) predict an X-ray emission from Inverse Compton of $L_x \approx 1.2 \times 10^{39} \text{ erg s}^{-1}$. This corresponds to a flux of $F_x \approx 5.1 \times 10^{-14} \text{ erg s}^{-1} \text{ cm}^{-2}$ for their estimated distance of 14 Mpc.

We find no evidence for statistically significant X-ray emission using Chandra and infer a 0.3-10 keV unabsorbed flux limit of $F_x < 6.3 \times 10^{-15} \text{ erg s}^{-1} \text{ cm}^{-2}$ at $\delta t = 40$ days (see §2.4). Their derived progenitor mass-loss rate of $\dot{M} = 1.4 \times 10^{-4} M_\odot \text{yr}^{-1}$ is comparable to the value calculated in this work; however, our deeper flux limit indicates either different microphysical parameters (ϵ_e and ϵ_B) than the ones adopted by Horesh et al. (2020) or suppression of the X-ray emission due to photoelectric absorption by a thick neutral medium.

Table 3. SN 2020oi Explosion Parameters Derived Using Multiple Models¹

Method	M_{Ni} (M_{\odot})	M_{ej} (M_{\odot})	t_{exp} (MJD)	t_{d} (days)	E_k 10^{51} erg
Arnett (1982)	$0.16^{+0.02}_{-0.02}$	$1.00^{+0.08}_{-0.08}$	$58855.4^{+0.2}_{-0.2}$	$8.41^{+0.28}_{-0.28}$	$0.97^{+0.13}_{-0.13}$
Khatami & Kasen (2019)	$0.08^{+0.02}_{-0.02}$	$0.81^{+0.03}_{-0.03}$	—	$19.88^{+0.36}_{-0.36}$	$0.79^{+0.09}_{-0.09}$
Guillochon et al. (MOSFiT; 2018)	$0.107^{+0.003}_{-0.003}$	$0.79^{+0.06}_{-0.07}$	$58853.99^{+0.08}_{-0.07}$	$8.08^{+0.23}_{-0.29}$	$0.77^{+0.10}_{-0.10}$
Final Values	$0.08^{+0.02}_{-0.02}$	$0.81^{+0.03}_{-0.03}$	$58854.0^{+0.3}_{-0.3}$	$19.88^{+0.36}_{-0.36}$	$0.79^{+0.09}_{-0.09}$

¹ The adopted explosion time was determined by fitting the early-time rise to a fireball explosion model.

7. SPECTRAL ANALYSIS

We have used the 1D Monte Carlo radiative transfer code TARDIS¹⁰ (Kerzendorf & Sim 2014; Kerzendorf et al. 2018) to estimate the composition of the SN ejecta from the obtained spectra. This requires us to assume a density distribution for the SN ejecta and a bolometric luminosity for each spectrum. For the bolometric luminosities corresponding to each spectral epoch, we have evaluated the bolometric light curve derived in §4. Given the similarity of the explosion to SN 1994I, we have adopted the density distribution model corresponding to a carbon-oxygen core of mass $M_f = 2.1 M_{\odot}$ immediately before explosion (CO21, Nomoto et al. 1994; Iwamoto et al. 1994b). Each spectrum has been computed within a given range of velocities, in which we have assumed the ejecta undergo homologous expansion. The minimum ejecta velocity for each spectrum was derived from the P-Cygni profile associated with its primary absorption features. Elemental abundances are assumed to be uniform within the velocity range considered. We concentrate our analysis on the four spectra measured closest to peak luminosity ($\delta t = 10.6, 14.6, 16.5$, and 18.4 days from explosion).

Our models are able to reproduce the dominant features identified in the observed spectra: we replicate the profiles of the Si II $\lambda 6355$ feature, the near-IR Ca II triplet, the Fe II contributions and the Mg II $\lambda 4481$ lines. Some discrepancies remain; for example, the simulated O I line predicts a slightly larger absorption than the observed line (similar to what is shown in Williamson et al. 2021). We have identified the C II $\lambda 6540$ line in the day 10.6 spectrum, and in order to simulate this feature, we have increased the abundance of carbon in the corresponding velocity regime. We have also included a non-negligible sodium abundance to reproduce the absorption observed around 5600 \AA . This feature may include some contribution from He I $\lambda 5876$, which is excited by non-thermal processes originating from the decay of nickel

generated in the explosion (Lucy 1991). A similar line of reasoning applies for the C II $\lambda 6540$ feature, which can be contaminated by residual absorption from He I $\lambda 6678$. We do not identify clear He I features in our spectral series, such as the triplet 2p-3s transition He I $\lambda 7065$ that is usually observed in the spectra of type-Ib SNe. The other optical He I $\lambda 4471$ feature is located in a region contaminated by other absorptions, mainly from Mg and Fe. Unfortunately, our spectral data do not cover the near-IR range where the bright lines He I $\lambda \lambda 10830, 20580$ are visible from the 2s-2p singlet/triplet transitions, and as a result we are unable to conclusively verify contributions from helium.

To further investigate the presence of a non-negligible helium abundance, we have also used the `recomb-nlte` option in TARDIS. For the day 11 spectrum, we have considered an amount of $\sim 0.01 M_{\odot}$ of helium in our simulated ejecta, and we obtain slightly stronger agreement with the observed spectrum. Nevertheless, we are unable to unambiguously confirm the presence of helium in the SN 2020oi ejecta. We note that the potential presence of helium was also considered in the case of the type-Ic SN 1994I (see e.g., Filippenko et al. 1995; Baron et al. 1999) and previously for SN 2020oi (Rho et al. 2021).

In Figure 10, we show the spectral series obtained near peak with the FLOYDS spectrograph along with the results of our spectral synthesis simulations. As an additional comparison, we plot three spectra corresponding to the type-Ic SN 1994I at comparable epochs in its explosion (Filippenko et al. 1995). The two events show notable similarities in their evolution and in the presence of Ca II, Mg II, Fe II, Si II, and O I features. SN 2020oi shows slightly higher ejecta velocities than SN 1994I (Millard et al. 1999), as estimated from the minima of the P-Cygni absorptions lines (in particular, from the Si II $\lambda 6355$ transition). This result is also consistent with the higher kinetic energy found for this SN (see §5) compared to SN 1994I ($0.6 - 0.8 \times 10^{51}$ erg; see Millard et al. 1999), and also its higher bolometric peak in Figure 4.

¹⁰ <https://tardis-sn.github.io/tardis/index.html>

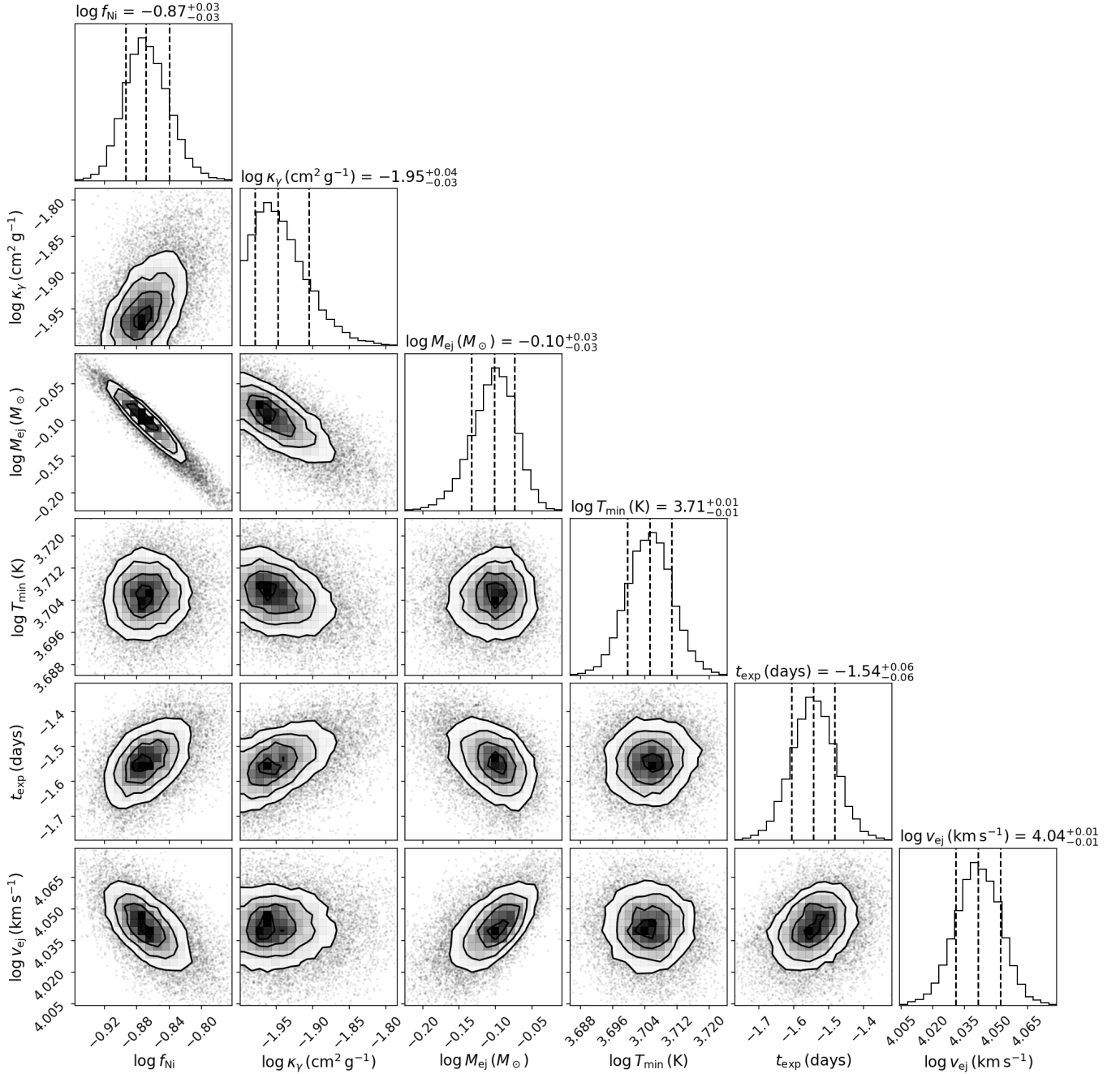


Figure 9. Corner plot of the model parameters for the SN 2020oi explosion found using the nested-sampler implementation in MOSFiT. Marginal distributions from the nested chains are shown at top along with the median parameter values and their $1\text{-}\sigma$ uncertainties. The parameter t_{exp} indicates the date of explosion relative to the first ZTF observation at MJD 58855.54.

The dominant species recovered from the TARDIS (Kerzendorf & Sim 2014; Kerzendorf et al. 2018) simulations of the peak spectra are shown in Figure 11, and the full abundance pattern found for each spectrum is presented in Table 4. The abundance pattern varies only marginally across the epochs that we have simulated and within the velocity range considered, suggesting mixing within the ejecta. Our simulated composition is also similar to that reported for other type-Ic

SNe for which element mixing has been discussed (Sauer et al. 2006). A more detailed analysis of these spectra considering a stratified abundance distribution is planned for an upcoming work, allowing us to further investigate mixing signatures.

8. THE VERY EARLY SPECTRUM OF SN 2020oi

We now consider the peculiar features of the SN 2020oi spectrum obtained at $\delta t = 3.3$ days. This spectrum is one of the earliest obtained for a type-Ic SN.

Table 4. Abundance Patterns for Simulated SN 2020oi Spectra

Phase	X_{He}	X_C	X_O	X_{Ne}	X_{Na}	X_{Mg}	X_{Si}	X_S	X_{Ca}	X_{Ni}	X_{Fe}	X_{Co}	X_{Cr}	X_{Ti}	X_{Ar}
+3.3d	0.65	0.10	0.168	0.00	0.000	0.030	0.040	0.000	0.0050	0.0001	0.0010	0.0000	0.00001	0.00001	0.00
+10.6d	0.14	0.05	0.600	0.10	0.001	0.006	0.006	0.005	0.0005	0.0005	0.0010	0.0001	0.00010	0.00010	0.02
+14.6d	0.01	0.05	0.650	0.19	0.010	0.005	0.004	0.001	0.0005	0.0005	0.0010	0.0000	0.00005	0.00005	0.04
+16.5d	0.00	0.02	0.750	0.20	0.010	0.003	0.003	0.005	0.0005	0.0005	0.0010	0.0000	0.00005	0.00005	0.02
+18.4d	0.00	0.01	0.750	0.20	0.010	0.003	0.003	0.005	0.0010	0.0007	0.0015	0.0000	0.00006	0.00006	0.03

NOTE—Values listed are fractional abundances.

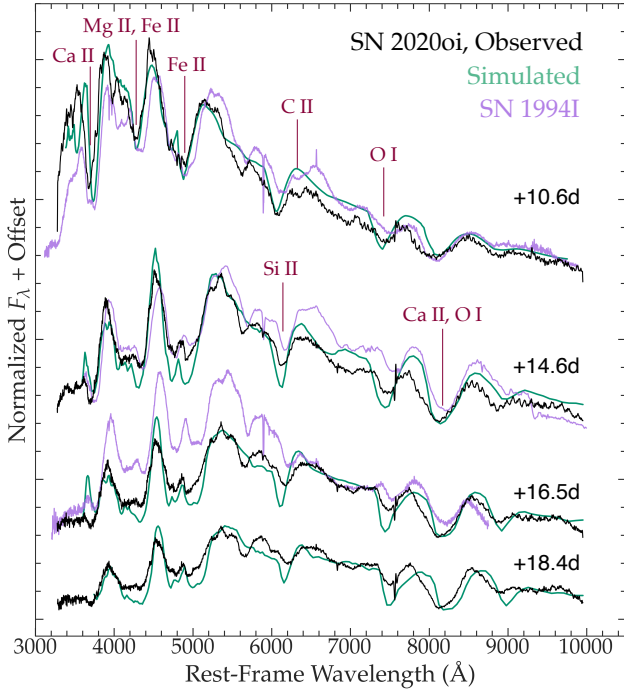


Figure 10. The spectra observed at $\delta t \approx 11, 15, 17$, and 18 days from explosion (black), along with the corresponding best-fit models (green). The spectra of SN 1994I are shown in violet for comparison. Mutual features associated with the presence of Ca, Mg, Fe, Si, and C are shown. The similarity between spectral sequences suggests similar ejecta composition and photospheric evolution for the two SNe.

This spectrum shows considerable absorption features from Si-burning elements, including Si II $\lambda 6355$ and the Ca II NIR triplet jointly expanding at a velocity of $v_{\text{exp}} = -24,000 \pm 500 \text{ km s}^{-1}$. At the same velocity, we have identified the feature at $\sim 4500 \text{ Å}$ as Fe II (multiplet 42), although this feature is likely blended with other fainter absorptions of Fe-peak elements (e.g., $\lambda = 4508.29 \text{ Å}$; see Aleo et al. 2017). The lack of a substantial absorption from O I $\lambda 7773$ indicates that the line-forming region of this spectrum is located in the most external layers of the ejecta, where the abundance pattern is enriched in lighter elements such as carbon and helium. Indeed, we find evidence for He I $\lambda 5876$ and C II $\lambda 6580$, and

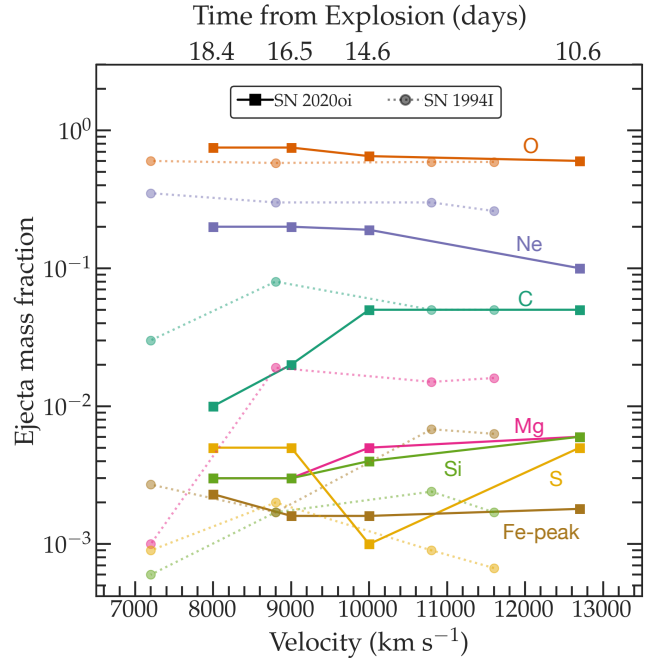


Figure 11. The best-fit ejecta composition for the four epochs corresponding to the modeled peak spectra. The epochs relative to the explosion date are listed at top, and the velocity values adopted for each epoch are shown at bottom. The best-fit composition for the SN 1994I ejecta at similar epochs (Sauer et al. 2006) is also shown. Although the composition of the SN 2020oi ejecta varies between epochs, the comparable abundances of O and Ne across the 8-day evolution indicates partial ejecta mixing.

cannot rule out a potential contribution from He I $\lambda 6678$. Unfortunately, our spectrum does not cover the near-IR region where the He I $\lambda 10830$ line is typically prominent in the presence of a helium-rich gas.

To characterize this early spectrum, we undertake the same composition modeling using TARDIS as was done for the peak spectra. However, we are unable to reproduce the observed spectrum using the same SN 1994I CO21 density distribution (Nomoto et al. 1994; Iwamoto et al. 1994b) that was adopted for the peak spectra; in particular, we cannot reproduce the blue excess observed at wavelengths $\leq 5000 \text{ Å}$.

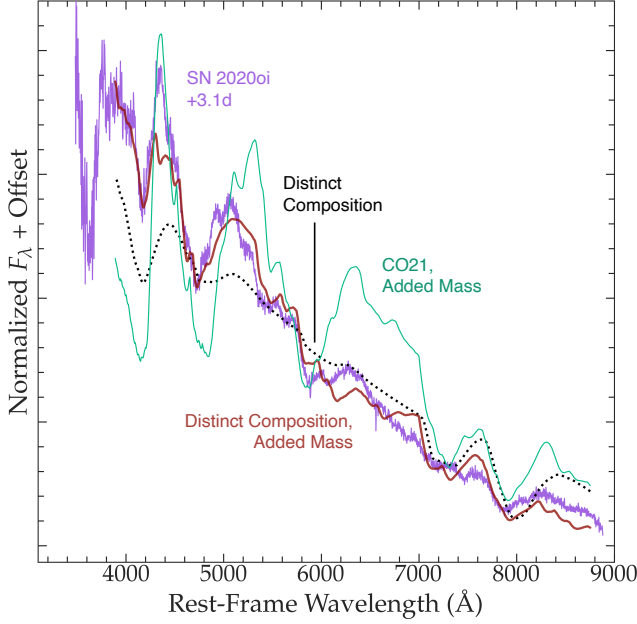


Figure 12. The early-time spectrum for SN 2020oi (violet) compared to three composition models: One in which a best-fit composition distinct from the CO21 model was used (black, dashed); one in which additional mass was added at the highest velocities with composition matching that of CO21 model (green); and one in which high-velocity mass was added with a composition distinct from CO21 (red). The model with a distinct composition (Table 4) of additional mass at high velocities provides the best fit to the day 3 spectrum.

Consequently, we have considered deviations from the pure CO21 model for this spectrum caused by the presence of a gas excess at larger radii. We note that a similar approach has been recently adopted in [Williamson et al. \(2021\)](#) in an analysis of SN 1994I. We find that our observed spectrum can be reproduced by an excess of $\sim 0.2 M_{\odot}$ of material composed of a large amount of carbon, helium, oxygen, and traces of heavy element signatures (Ca, Si, S, Fe) at the highest velocities ($v_{\text{exp}} \approx -24000 \text{ km s}^{-1}$), roughly corresponding to $\sim 10^{14} \text{ cm}$ at the time the spectrum was obtained (assuming homologous expansion). We show this best-fit spectrum, as well as those predicted by the CO21 composition and density models, in Fig. 12. *Our fits suggest that the blue excess of the day 3.3 spectrum can be explained by an additional-mass component with a composition distinct from the ejecta near peak.* However, we note that our final simulation does not precisely reproduce the continuum at bluer wavelengths (e.g. $\lambda < 5000 \text{ Å}$).

If the blue excess observed in the day 3.3 spectrum is the result of emission from material present at the highest explosion velocities, any additional signatures within the day 6.6 spectrum will better constrain its mass and composition. This analysis is beyond the scope of this work but is planned for a separate publication.

9. CHARACTERIZING THE EARLY-TIME OPTICAL AND UV EMISSION OF SN 2020oi

9.1. Evidence for Flux in Excess of an Expanding-Fireball Explosion Model

We now consider the evidence for a bump in the photometry at day $\delta t \approx 2.5$ in excess of the emission expected for traditional SN explosions.

We fit the extinction-corrected flux spanning 3 to 10 days post-explosion in each band (excluding the early-time bump) to a canonical expanding-fireball model ($f \propto (t - t_{\text{exp}})^2$, where t_{exp} is the time of explosion). We have also fit a $(t - t_{\text{exp}})^n$ model where we allow n to vary between 1.0 and 3.0, finding reasonable agreement with the rise across all bands for $n = 1.7$. We present both models in Fig. 13 along with the associated photometry. Although neither model perfectly captures the early-time rise of the SN due to their simplicity, the $n = 1.7$ model more accurately describes the gradual increase in explosion flux past $\delta t \approx 6$ days. The models most closely fit the data between 4 and 6 days, which is unsurprising given the higher photometric uncertainties for data obtained at later epochs. We calculate the reduced- χ^2_{ν} Goodness-of-Fit across all bands for our analytic fireball models, where ν quantifies the degrees of freedom in our early-time dataset.

We find a χ^2_{ν} value of 1.9 for the $n = 2$ model and 0.5 for the $n = 1.7$ model. Next, we calculate the reduced- χ^2 across all bands for the values between 2.2 and 2.7 days (comprising the early bump). We find a χ^2_{ν} value of 15.0 for the $n = 2$ model and 4.7 for the $n = 1.7$ model, indicating significantly worse fits for these observations than for the rest of the data composing the rise. Further, the consistency of the flux in excess of the best-fit models between bands (which is not captured by our χ^2_{ν} metric) and within photometry taken at multiple observatories indicates a physical origin. We investigate potential explanations for this excess in the following sections.

9.2. Emission from Shock Cooling

To characterize the excess flux observed in the pre-maximum UV and optical photometry, we first consider four distinct shock-cooling models. In the first two models, we apply the [Sapir & Waxman \(2017\)](#) treatment using two values for the polytropic indices of the progenitor star. These models assume a progenitor composed of a uniform density core of mass M_c and a polytropic envelope in hydrostatic equilibrium. Immediately following shock breakout, the emission is assumed to be dominated by the outermost layers of the envelope; in subsequent epochs, the emission from successively deeper layers dominate. We adopt polytropic indices of $n = 3/2$ and $n = 3$, appropriate for a red super-giant with a convective envelope and a blue super-giant with a radiative envelope, respectively. Although these extended hydrogen

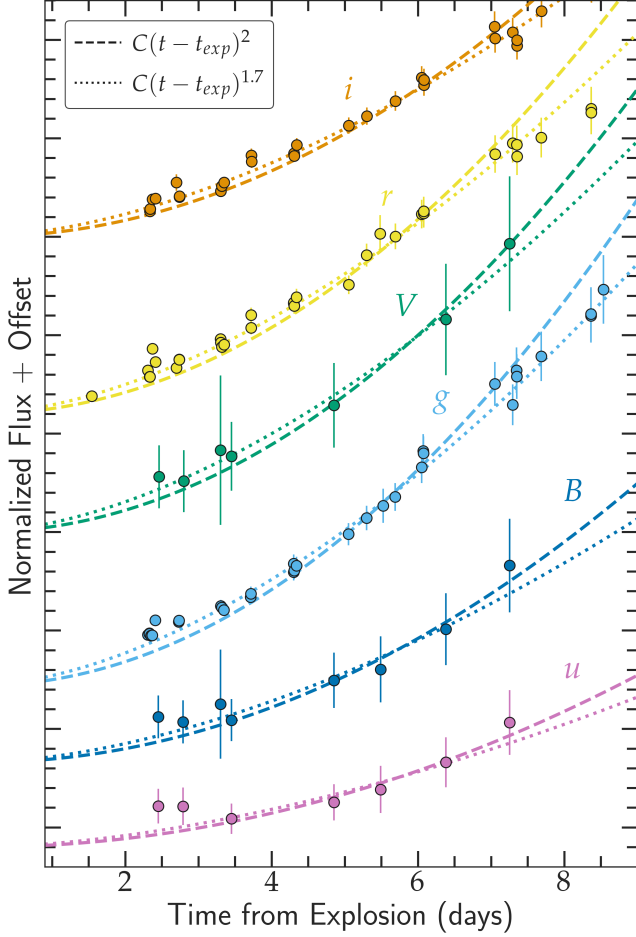


Figure 13. The early-time normalized flux of SN 2020oi. The dashed line corresponds to a canonical expanding-fireball model $f \propto (t - t_{\text{exp}})^2$ applied to days 3 – 10 of the photometry in each band, while the dotted line describes a model with $f \propto (t - t_{\text{exp}})^{1.7}$ to more accurately capture the photometry in *gri* bands following 7 days. Flux in excess of that predicted by both models can be seen at $\delta t \approx 2.5$ days from explosion for the majority of bands.

envelopes have been stripped in the case of SNe Ic such as SN 2020oi, this is one of the only shock-cooling treatments in the literature that attempts to account for the density profile of the progenitor (by the ability to change the polytropic index of its envelope). As a result, it remains a valuable probe of the shock breakout kinetics of stripped-envelope events.

For the third model, we consider the one-zone analytic solution described in Piro (2015). This model considers shock-cooling from surrounding circumstellar material and is independent of the chemical composition and density profile of the material. The fourth model uses a revised treatment for this emission from Piro et al. (2021), which differs from the original formalism with the addition of a power-law dependence of the luminosity with time during the rise of the early emission.

Each of these models allows us to constrain the mass (M_{env}) and the radius (R_{env}) of extended material surrounding the progenitor; the shock velocity v_s ; and the time between the early excess and the time of explosion t_{exp} . As in Jacobson-Galán et al. (2020), we use the package *emcee* to sample our model parameter space and obtain the fit with the smallest χ^2 value.

Adopting the procedure outlined above, none of the four models successfully converged to a solution that accurately characterized the early-time photometry. The reason for this lies in the first photometric observation for the event (see Fig. 13) in *r* band, which was originally reported in the ZTF alert stream (Bellm et al. 2019a). If the explosion occurred within an environment free of surrounding material, the emission during shock-breakout of the progenitor’s photosphere should be the earliest optical emission observed. The initial *r* band observation occurs > 0.5 days earlier than the rest of the photometry and agrees with the continuum predicted by the analytic rise models outlined in the previous section. This suggests that shock breakout from the stellar surface occurred earlier than the optical excess at $\delta t \approx 2.5$ days, and the models considered are unable to reconcile these two phases of early-time photometry. The timescale of these observations disfavors shock-cooling of surrounding material as the cause of the flux excess; nevertheless, we caution that these simplified models have been validated against prominent early emission signatures and may be unsuitable for more subtle excesses.

To account for the possibility that the first ZTF observation was not caused by the explosion, we manually fit our shock-cooling models to the early-time bump excluding this point to estimate the properties of the resulting progenitor photosphere. Both these parameters and those corresponding to the full MCMC fit are presented in Table 5. From the manual fits, which are shown in Fig. 14, we derive $M_{\text{env}} \approx 0.5 - 70 \times 10^{-2} M_{\odot}$, $R_{\text{env}} \approx 4 - 14 R_{\odot}$, and $v_{\text{env}} \approx 2 - 4 \times 10^4 \text{ km s}^{-1}$. Although the range in shock velocities found is consistent with the value of $2.4 \pm 0.2 \times 10^4 \text{ km s}^{-1}$ estimated spectroscopically for the photosphere at $\delta t \approx 3.5$ days, binary evolution models from Yoon et al. (2010) (Fig. 12) predict larger radii for a progenitor of final mass $2.1 M_{\odot}$ as is suggested by the spectroscopic analysis detailed in Section 7. Although these results suggest that only a small amount of mass located at the photosphere of the progenitor is needed to explain this emission, additional analysis is required to reconcile the characteristics of the observed bump with the initial ZTF detection.

Although shock-heating of dense CSM has been proposed to explain the VLA radio observations of SN 2020oi (Horesh et al. 2020), the first radio emission was detected at $\delta t = 4.9$ days. This is ~ 2.5 days later than the early-time optical and UV excess. If both emission is caused by shock-heated media,

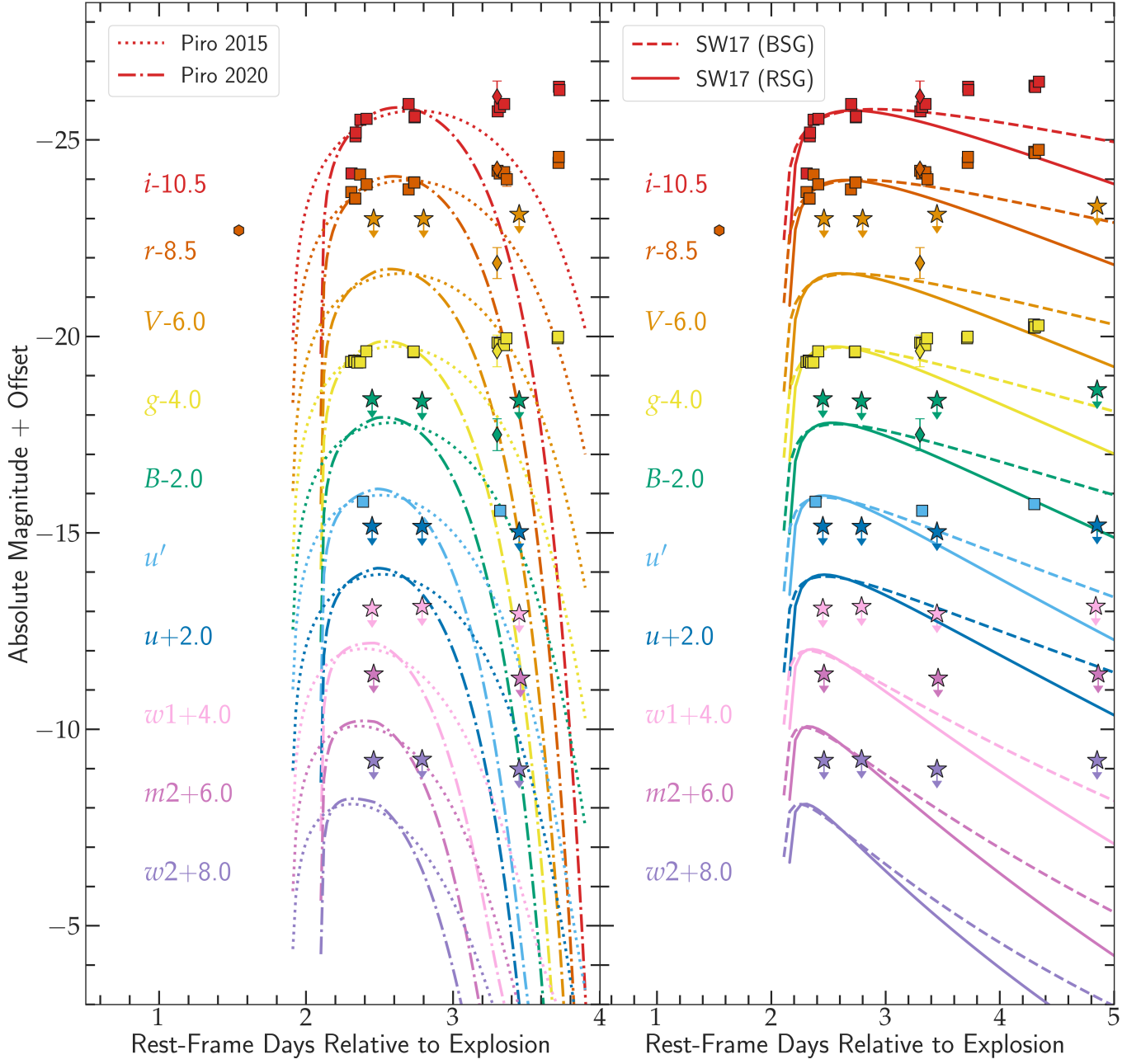


Figure 14. The best-fit shock-cooling models for SN 2020oi excluding the first ZTF observation in r band, shown along with the optical and UV photometry corresponding to the first five days of explosion. Four analytic fits were considered to characterize the early-time observations: Piro (2015); Piro et al. (2021); and Sapir & Waxman (2017) using polytropic indices of $n = 3/2$ and $n = 3$.

the radio-emitting material must either exist at significantly higher radii than the optically-emitting material or the same material must be dense enough to explain the delay (in which case the material would likely be optically thick to the radio emission in the first place). This suggests that the SN 2020oi radio observations are uncorrelated with the optical excess, and that the two signatures are probing distinct environments. Without radio observations closer to the epoch of the photometric bump, we are unable to use the VLA data to verify the presence of nearby CSM.

9.3. Emission from Companion Interaction

The ejecta mass derived in §5 and the agreement of the CO21 composition model with peak spectra in §7 both suggest that SN 2020oi originated in a binary system. For systems with low binary separations, the explosion of the primary star will affect the secondary, and it has been theorized that the presence of a companion can be deduced by the signature it imprints on the earliest moments of an SN explosion.

The study by Kasen (2010) in connection with SNe Ia is illustrative. In the conceptual framework presented, the presence of the companion blocks the expansion of the explosion ejecta and carves out a cavity behind it. Thermal diffusion from the heated ejecta, which is typically unable to escape at early times because of the high optical depths involved, then leaks into this rarefied space as radiation. This emission, which varies in intensity based on the binary separation a and the viewing angle θ , can be observed as an optical and UV excess at $\delta t < 8$ days above the broad continuum dominated by synthesized ^{56}Ni .

For the type-Ia simulated by Kasen, the emission timescale associated with companion interaction varies from ~ 2 days for highly inclined viewing angles to ~ 8 days for an interaction along the line of sight. The lower end of this timescale range agrees more with the inclusion of the early ZTF observation than the timescales associated with the shock-cooling models in the previous section, although we caution that this range may differ for SN Ic progenitor interactions. In addition, as is detailed in §8, interaction with material at $\geq 10^{14}$ cm can explain the blue excess in the day 3.3 spectrum.

Interaction of the explosion with a binary companion, proceeding in a manner similar to that outlined in Kasen (2010), should produce additional early-time signatures. When the initial SN shock collides with the surface of the companion, the post-shock energy is released as an X-ray burst spanning the first few hours of the event in advance of the UV/optical emission. Further, because the SN ejecta are distorted by the presence of the companion, the subsequent emission should show polarization indicative of ejecta asymmetries. Observations of SN 2020oi taken using the WIRC+Pol instrument at Palomar Observatory (Tinyanont et al. 2021) near peak found a broadband polarization of $p = 0.37 \pm 0.09\%$, low

enough to be explained by interstellar dust scattering and not asymmetry within the explosion itself. Because the flux-excess timescale agrees more closely with the highly-inclined interactions simulated in Kasen (2010), and the polarization measurements were taken long after any potential interaction, early asymmetry may be difficult to detect; further, the polarization signature of companion interaction at peak light (or lack thereof) remains unconstrained in the literature.

Nevertheless, the question remains as to whether the interaction of a type-Ic explosion with a binary companion would produce a similar flux excess to that predicted for SNe Ia. The analysis in Kasen (2010) considered a low-mass companion with radius between 10^{11} cm (for an evolved sub-giant) and 10^{13} cm (for a red giant). In contrast, most companions of stripped-envelope supernovae should reside on or near the ZAMS (Zapartas et al. 2017), and so the signatures of binary interaction should be relatively faint (Liu et al. 2015) except for rare close-binary systems (Rimoldi et al. 2016). The stellar cluster coincident with SN 2020oi limits our ability to constrain the brightness of a companion and derive its physical properties. The majority of binary evolution models in BPASS that agree with our derived ejecta mass (see §12) feature a companion with radius immediately pre-explosion below 2×10^{11} cm and an orbital separation below 10^{12} cm. 80% of these systems feature radial separations higher than the close-binary systems considered in Rimoldi et al. (2016). Further, the optical bump occurs ~ 0.7 days after the first ZTF detection. Estimating the ejecta velocity as $\sim 23,000 \text{ km s}^{-1}$ at early times, this corresponds to a distance of $\sim 10^{14}$ cm. As a result, the likely binary separation for this system is lower than suggested by the timescale of the excess if caused by companion interaction and higher than the necessary separation for a bright signature.

9.4. Emission from Hydrodynamical Interaction of the Ejecta with Circumstellar Material

The rapidly-expanding shock wave from an SN is followed by its more slowly-moving ejecta. For progenitor systems surrounded by CSM, the collision of the ejecta with this material creates a high-temperature interface whose multi-wavelength emission is re-processed and re-emitted. Although many stripped-envelope supernovae (SE SNe) for which CSM interaction has been proposed have been SNe Iib (e.g., 1993J and ZTF18aalrxas; Schmidt et al. 1993; Fremling et al. 2019), there is increasing evidence that this process can also occur in SNe Ib/c (Milisavljevic et al. 2015; De et al. 2018; Sollerman et al. 2020).

The presence of local CSM as inferred from an early-time signature indicates a mass-loss episode concurrent with or immediately preceding the explosion. It has been recently realised that SNe can occur even for the fraction of stripped stars that are stably transferring mass onto a binary companion

Table 5. Shock Cooling Models

Model	R_{env}	M_{env}	v_{env}	t_{exp}	χ^2_{ν}	DOF
	R_{\odot}	$[\times 10^{-2}] M_{\odot}$	$[\times 10^4] \text{ km s}^{-1}$	MJD	days	
P15	~ 6	~ 1.5	~ 2.2	—	—	—
P15 ^a	$7.23^{+2.33}_{-0.45}$	$0.82^{+0.02}_{-0.03}$	$2.45^{+0.10}_{-0.20}$	$58855.9^{+0.08}_{-0.03}$	51.7	21
P20	~ 18	~ 0.9	~ 3.6	—	—	—
P20 ^a	$13.6^{+1.31}_{-1.24}$	$0.47^{+0.02}_{-0.02}$	$4.03^{+0.10}_{-0.10}$	$58856.1^{+0.01}_{-0.01}$	53.7	20
SW17 [n=3/2]	~ 7.1	~ 6	~ 1.6	—	—	—
SW17 ^a [n=3/2]	$4.3^{+0.4}_{-0.3}$	$2.4^{+0.3}_{-0.2}$	$2.36^{+0.11}_{-0.11}$	$58856.2^{+0.1}_{-0.1}$	50.6	20
SW17 [n=3]	~ 7.2	~ 70	~ 1.8	—	—	—
SW17 ^a [n=3]	$5.7^{+1.1}_{-1.1}$	$67.0^{+1.5}_{-2.3}$	$2.04^{+0.20}_{-0.21}$	$58856.1^{+0.1}_{-0.1}$	52.9	20

^aFitting only the flux excess i.e., $2 < t < 3$ days after explosion.

(Laplace et al. 2020), potentially providing fresh CSM with which the ejecta could collide.

Current models (Laplace et al. 2020; Götzberg et al. 2020; Mandel et al. 2021) indicate that significant expansion of the progenitor star occurs only at sub-solar metallicity, ~ 50 kyr before the explosion and once again a few kyr before the explosion (although different progenitor mass-loss histories may allow for expansion at higher metallicities, as is suggested by Gilkis et al. 2019). During the latter interaction phase, the radius of the SN progenitor exceeds several R_{\odot} , thus creating a CSM cloud of at least 10^{13} cm. Much less mass ($< 0.1 M_{\odot}$) is shed during this secondary pre-explosion interaction relative to the first. Given that the envelope mass will be continuously ejected over the few kyr before the SN, and assuming a characteristic ejection velocity of 100 km s^{-1} (comparable to the orbital velocity at such separations), one may realistically expect a tenuous cloud extending up to $10^{17.5}$ cm around the system by the explosion time. Such clouds are sufficient to produce an early excess (Chevalier 1982). Because the density of this material strongly decreases with radius, a flux excess from CSM interaction would originate in the inner layers ($10^{14} - 10^{15}$ cm) of the cloud and the collision shock would accelerate as it expanded into the outermost low-density media. This distance is consistent with the timescale for the optical bump observed. The SN energy, in turn, would decrease due to the mass loss in the preceding binary interactions but remain comparable to typical type-Ic SN energies as an upper limit (Zenati 2021).

The main prediction of this scenario is that the event must have originated in a location with sub-solar metallicity, which supports the findings both from *HST* photometry in §10 and from MUSE spectroscopy in §11. Further, the explosion of the progenitor into CSM composed of its own lost envelope should lead to early-time spectroscopic signatures of the light elements shed, as is strongly suggested by the spectroscopic

analysis in §8. Radiative diffusion through asymmetrically-distributed or clumpy CSM may also explain the offset of the excess relative to the initial ZTF observation.

Another interesting line of evidence that may indicate CSM interaction lies in the rising *K* band continuum found by Rho et al. (2021) 63 days from MJD 58854, which can be attributed to infrared emission from dust. Rho et al. (2021) suggest that this signature may be produced by dust condensing directly from the SN ejecta, pre-existing CSM dust heated by SN radiation, newly formed dust from CSM interactions with the explosion, or an infrared echo from dust in the galaxy’s interstellar medium. A dusty pre-existing CSM shell heated by the SN shock at the time of explosion should be located at a distance of $10^{16} - 10^{17}$ cm to generate infrared (IR) emission ~ 60 days post-explosion. This distance is in general agreement with the limits placed on the sizes of previously-observed dust shells (Fox et al. 2013), but it remains unclear whether any CSM surrounding SN 2020oi at these radii would be dense enough to produce the day-63 IR emission. Additional analysis is therefore necessary to determine whether the most-likely CSM density structure created by type-Ic SNe undergoing Roche-lobe overflow could be responsible for both optical and IR signatures.

9.5. Emission caused by Asymmetric ^{56}Ni

It is possible that the presence of decaying ^{56}Ni in the outer layers of the SN ejecta is the source of the early flux excess, as has been proposed for stripped-envelope events with multiple light curve peaks (Drott et al. 2016) and other type-I events with less-prominent photometric excesses (Magee & Maguire 2020). An asymmetric or shallow distribution, in comparison to the centrally concentrated ^{56}Ni ejecta assumed by the Arnett model, would power an event that is blue at early times and red at late times as the outer layers are locally heated (Magee et al. 2018). We do not find significant evi-

dence for this trend in our spectral sequence relative to that for SN 1994I in §7.

It is possible that a jet can deposit ^{56}Ni into the outermost, high-velocity ejecta of an SN, as was proposed for the type-Ib SN 2008D (Bersten et al. 2013); however, we have detected no X-ray emission associated with SN 2020oi as would be expected for a jet. In theory, the mass of nickel-rich material needed to explain our early-time emission is likely small (Magee & Maguire 2020). However, as we note in earlier sections, significant asymmetry in the ejecta is at odds with the negligible polarization at peak light observed by Tinyanont et al. (2021). Further, we have found in §8 that by including C and He at significantly higher radii than the rest of the ejecta, we are able to reproduce the day 3.3 spectrum more faithfully than by considering an excess contribution of Ni and Fe.

9.6. Conclusions on the Photometric Excess

The above considerations lead us to the conclusion that the early-time flux excess may be the emission from ejecta interaction with CSM at large radii. We illustrate this scenario in Fig. 15. We note that the interpretation of CSM interaction is not inconsistent with the absence of narrow photoionization features in the day 3.3 spectrum from §8, as these may have been detectable at earlier epochs (Khazov et al. 2016). We caution that given the limited number of predictive excess models available in the literature for stripped-envelope events, other interpretations are possible. Further, at present we are unable to constrain whether CSM surrounding the SN is the result of late-stage Roche-lobe overflow, the tenuous remnant of a previous mass-transfer episode, or an eruptive mass-loss event (e.g., Shiode & Quataert 2014). The viability of late-stage Roche-lobe overflow from theoretical simulations of this explosion will be the focus of a subsequent paper.

10. PROPERTIES OF THE STELLAR CLUSTER COINCIDENT WITH 2020oi FROM PRE-EXPLOSION PHOTOMETRY

In this section, we derive the properties of the stellar cluster associated with SN 2020oi from pre-explosion photometry obtained with the *Hubble Space Telescope* (*HST*).

We use the code *Prospector* (Leja et al. 2017) to generate synthetic integrated Spectral Energy Distributions (SEDs) corresponding to a series of Simple Stellar Populations (SSPs, which are assumed to be created instantaneously). The *Prospector* package allows for both MCMC sampling in *emcee* (Foreman-Mackey et al. 2013) and dynamic nested sampling in *Dynesty* (Speagle 2020) to generate posterior estimates for a set of model parameters. In addition, it provides an interpolation scheme for generating SEDs spanning an arbitrarily fine grid in parameter space.

To characterize the stellar cluster associated with the SN, we first calculate its extinction-corrected flux in each *HST*

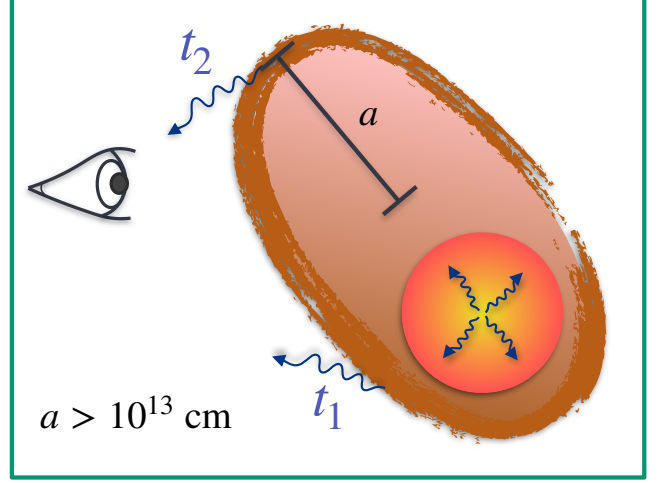


Figure 15. Diagram illustrating flux excess from ejecta interaction with asymmetric CSM. In this scenario, the SN ejecta collide with an asymmetric cloud and the thermal emission of the material as it cools is observed at distinct epochs (t_1 and t_2 corresponding to the epoch of the first ZTF point and the epoch of the photometric bump, respectively) based on its optical depth. From simulations of similar binary systems, the minimum semi-major axis of the cloud predicted is $\geq 10^{14}$ cm, which would agree with the presence of material as is inferred in §8.

filter prior to explosion. We then develop an SED model in *Prospector* parameterized by the age of the stellar cluster t_{Clust} ; the cluster metal mass fraction $\log_{10}(Z/Z_{\odot})$; and the cluster mass M_{Clust} . We implement top-hat priors for $\log_{10}(Z/Z_{\odot})$ and t_{Clust} spanning $[-2, 0.2]$ and $[0.1, 300]$ Myr, respectively, informed both by our later MUSE analysis and the stellar populations predicted in Allard et al. (2006). For our prior on M_{Clust} , we impose a log-uniform distribution spanning $[10^4, 10^{11}] M_{\odot}$. We then sample the posterior distribution of each SED model marginalized by our *HST* observations using *emcee*, where we have chosen 128 walkers for two rounds of burn-in of length 25 and 50, respectively, and a run length of 1000 iterations.

For comparison, we have additionally calculated the results obtained using *dynesty* and from a targeted brute-force grid search of the parameter space, in which we have sampled 200 values each of M_{Clust} , $\log_{10}(Z/Z_{\odot})$, and t_{Clust} within $[10^{4.5}, 10^{6.5}] M_{\odot}$, $[-2, 0]$, and $[1, 100]$ Myr, respectively. For each of our SSPs, we assume the Chabrier log-normal stellar IMF (Chabrier 2003) and a Milky-Way curve for extinction of starlight from dust surrounding old stars (Cardelli et al. 1989). We have verified that the use of the Calzetti et al. (2000) extinction law does not alter our results.

We present a corner plot of our posterior estimates from both *emcee* and grid search in the right panel of Figure 16. Both methods predict a best-fit median cluster mass of $\log(M_{\text{Clust}}) = 5.86^{+0.14}_{-0.26} M_{\odot}$, a cluster metallicity of $\log(Z/Z_{\odot}) = -1.58^{+0.35}_{-0.31}$, and a cluster age of $t_{\text{Age}} =$

40^{+30}_{-20} Myr. Our dynesty values are consistent with these estimates.

Knapen et al. (1995) undertakes a similar analysis in the innermost region of M100 by fitting spatially-averaged optical and IR observations of dominant star-forming regions to stellar population models. For the region coincident with SN 2020oi, the authors find a best-fit model composed of multiple stellar populations but dominated by stars of age ~ 40 Myr, in close agreement with our estimate. A further study by Allard et al. (2006) derived an age of $10 - 30$ Myr for the stellar population associated with SN 2020oi. These studies, coupled with our Prospector results from above, suggest that the SN progenitor is coincident with a young (~ 40 Myr) stellar cluster. Although we do not find evidence for multiple populations of stars as a direct consequence of our simplified SSP treatment, we do not have the wavelength coverage to constrain a more complex star formation history.

11. HOST-GALAXY PROPERTIES FROM MUSE SPECTROSCOPY

The inner region of NGC 4321/M100 was observed with the European Southern Observatory Very Large Telescope (Henault et al. 2003) with the Multi Unit Spectroscopic Explorer (MUSE) in the wide-field mode with adaptive optics configuration (WFM-AO) on April 28, 2019 (Prog. ID 1100.B-0651, PI: Schinnerer). Using the code described in Fusco et al. (2020) to reconstruct the atmospheric conditions at the epochs observed, we derive PSF FWHM values of $0.677''$, $0.509''$, and $0.375''$, for 5000 \AA , 7000 \AA , and 9000 \AA , respectively, for our MUSE data. MUSE data have been reduced using standard esorex recipes that were embedded in a general python-based script. The final data cube covers $\sim 90\%$ of the *HST/ACS F814W* image, corresponding to the bright star-forming ring surrounding the center of the galaxy as can be seen in Fig. 17.

To analyze the MUSE data cube, we have first corrected for the Galactic reddening in the direction of the galaxy and then reported each single spaxel in the rest-frame, assuming a redshift of $z = 0.0052$. Then, we have applied the Voronoi spatial binning method (Cappellari & Copin 2003) assuming a signal-to-noise value of 40 in a wavelength range characterized by an absence of spectral features ($\Delta\lambda = 5600 - 5700 \text{ \AA}$). After this binning, we use our analysis tools to study the properties of the underlying stellar component and nebular gaseous emission in each spectral bin. For each specific physical property we aim to study, we obtain a detailed spatially-resolved map across the full data cube and in the immediate surroundings of SN 2020oi.

11.1. Stellar Populations within M100

To distinguish the underlying stellar continuum from the gaseous emission, we have applied the stellar population synthesis code STARLIGHT (Cid Fernandes et al. 2005) to each spectral bin. STARLIGHT allows us to fit an observed spectrum to a combination of template spectra, which can be composed of either individual stellar spectra or distinct stellar population models obtained from evolutionary codes. In the current work, we have used the stellar population synthesis models described in Bruzual & Charlot (2003). This library consists of 150 stellar templates generated with a Chabrier initial mass function (Chabrier 2003) with ages varying between 10^6 yrs and 1.8×10^{10} yrs, and with metallicity spanning from $Z = 0.0001$ to $Z = 0.05$ in six bins (where $Z_{\odot} = 0.02$). This allows us to generate best-fit estimates for the age and metallicity distribution of M100, according to the input templates. A caveat is given by the wavelength range provided by MUSE: with a rest-frame range of $4675 - 9300 \text{ \AA}$, we miss the bluest region of stellar spectra where important indicators for the star formation history are present (e.g., Mg and Ca H&K absorption lines). As a result, the values provided are mainly based on indicators available in the wavelength range covered by MUSE at $z = 0.0052$, e.g. the Ca II near-IR triplet.

We plot the light fraction contributions for young ($t < 500$ Myr), intermediate age ($500 \text{ Myr} < t < 5 \text{ Gyr}$), and old ($t > 5 \text{ Gyr}$) stellar populations in Fig. 18. Most evident is an anti-correlation of old stellar light with the spiral arms that comprise the nuclear ring. This anti-correlation is not evident in either of the two other maps, suggesting that the nuclear ring is comprised primarily of a combination of young and intermediate-age stars. Light from all three of these populations can be seen near the location of the SN, and because of the limited resolution of the IFU data we are unable to definitively associate it with a single stellar population.

11.2. SN 2020oi as Evidence for Cold Gas Dynamics in M100

M100 has been extensively studied due to its close proximity and its active star formation sites (Sakamoto et al. 1995; Garcia-Burillo et al. 1998; Castillo-Morales et al. 2007; Azeez et al. 2016; Elmegreen et al. 2018). To date, seven SNe have been discovered within M100, but only SN 2020oi occurred within its central $5''$. This makes it possible to leverage previous analyses to further characterize the progenitor system and its formation as a consequence of the dynamical evolution of its host galaxy.

SN 2020oi exploded within a “nuclear ring” of radius $\sim 5''$ where the majority of star formation within M100 occurs (Ryder & Knapen 2001). Allard et al. (2005) used SAURON IFU spectroscopy to probe the ring’s H β emission and gas dispersion. In their model of nuclear ring formation, cold gas is channeled inward along the dust lanes of the spiral arms

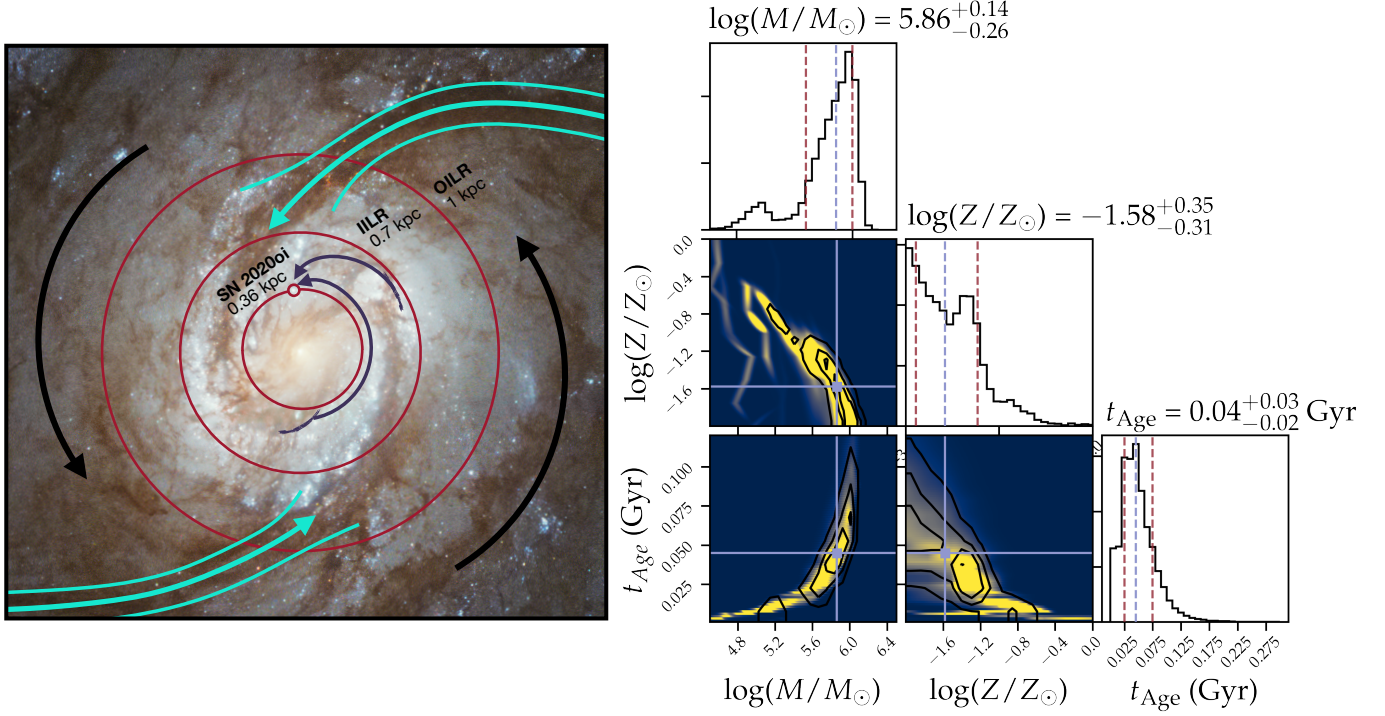


Figure 16. Left: Schematic diagram illustrating the proposed star formation mechanism associated with M100’s nuclear ring. Cold gas flows inward along the spiral arms (turquoise channels) and collects between the Outer Inner and Inner Inner Lindblad resonances (OILR and IILR, indicated as red circles at ~ 1 kpc and ~ 0.7 kpc, respectively), and then sinks toward the nucleus from gravity. This material then sweeps past the spiral arm shock fronts in its rotation and collapses, forming new stars. Two possible paths for the SN 2020oi progenitor from formation to explosion are shown in violet and used to provide an independent estimate for the age of the system (see §11.2). The innermost red circle marks the radial offset of SN 2020oi. **Right:** Corner plot corresponding to our best-fit parameters for the *HST* pre-explosion photometry of the stellar cluster associated with SN 2020oi. Emcee results are shown in black contours and posterior probabilities derived from a manual grid search is shown in color (where yellow corresponds to the highest-probability parameters and blue corresponds to the lowest). Marginal histograms are plotted at top, with median posterior values marked by light blue lines and first and third quartiles marked by red lines.

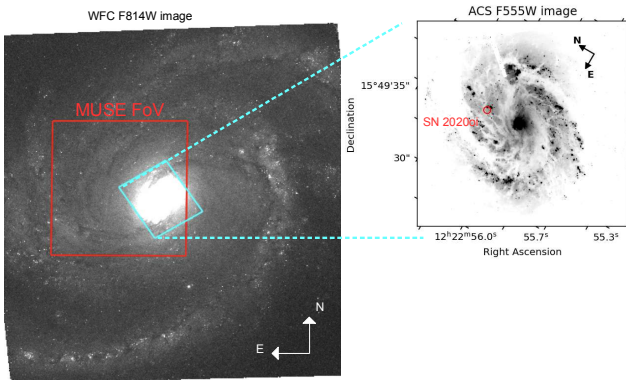


Figure 17. *Hubble Space Telescope* images of the host galaxy of SN 2020oi. The left image corresponds to a Wide-Field Camera observation in the F814W filter, which covers almost the entire galaxy, while the right panel shows the inner region of M100 as observed by the Advanced Camera for Surveys (ACS) in the F555W filter. The position of SN 2020oi is shown as a red circle. On the WFC image, the corresponding field of view of the ACS, as well as the region covered by MUSE observations, are over-plotted with cyan and red squares, respectively.

under the gravitational influence of the central bar. This gas settles near the inner Lindblad resonances for the galaxy at the contact points between the nuclear ring and the innermost spiral arms. At the trailing edge of the spiral arms, where the velocity gradient is smaller than at the shock fronts, cold gas clumps and star formation is induced. These locations are predicted to contain the youngest stellar populations within the nuclear ring. The connection between core-collapse progenitors and the clumping of atomic gas by the motion of spiral arms has also been explored in the galaxy M74 (Michałowski et al. 2020). We illustrate this mechanism in the left panel of Fig. 16.

Because the SN took place within the co-rotation radius for M100, the gas and dust at the radius of SN 2020oi is rotating more rapidly than the pattern speed of the spiral arms. If the SN 2020oi progenitor formed from the action of the spiral arms, we can obtain a rough estimate for its age from the time over which the newly-formed stellar cluster underwent roughly circular motion from within a spiral arm to its current location. We first use a PS1 *gri*-band composite pointing of M100 to estimate the coordinates of a point along the leading edge of each of the inner dust lanes, such that they are

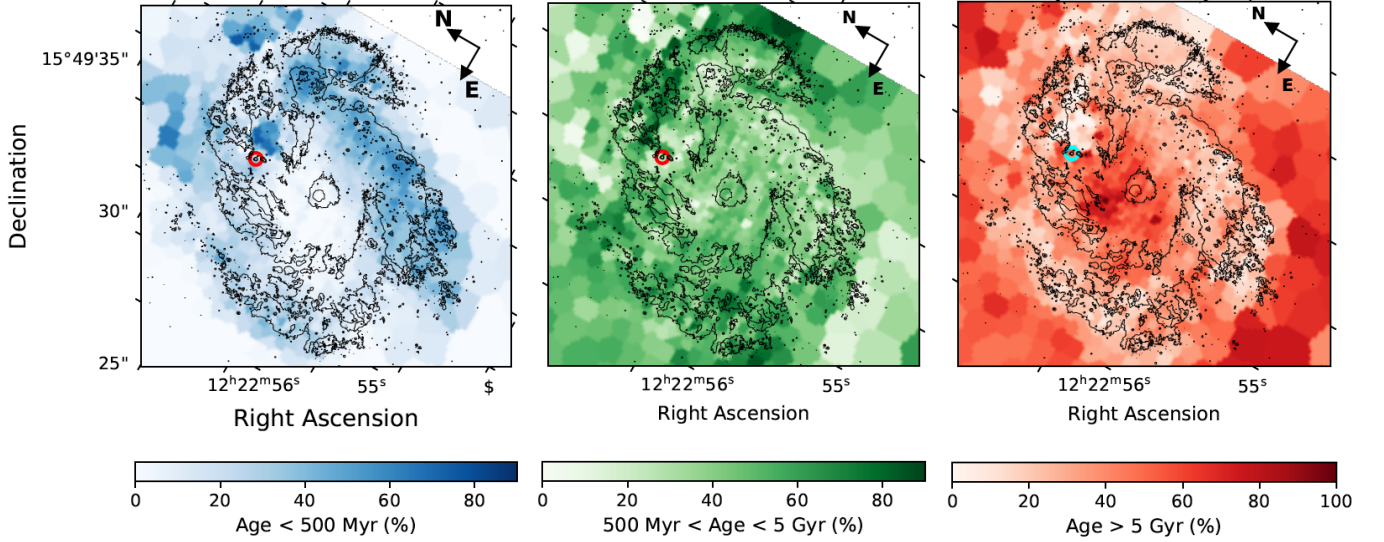


Figure 18. Light fraction contributions for three populations of stars within the nucleus of M100 as derived from MUSE spectroscopy. The location of SN 2020oi is marked with a circle in the upper left corner of each map.

roughly the same distance from the nucleus as SN 2020oi (~ 4.5 arcsec). Assuming the cluster undergoes circular rotation, we evaluate the rotation curve for M100 from Knapen et al. (2000) at $4.5''$ (using both the $H\alpha$ and CO-derived estimates) and determine the differential speed between the matter at this radius and the pattern speed of the spiral arms from Hernandez et al. (2005). We then calculate the length of the circular arc connecting SN 2020oi to each of the dust lanes, accounting for an extinction with respect to our line of sight of $i = 30^\circ$ (Knapen et al. 2000). From these estimates, we derive an upper limit to the age of the progenitor cluster of $t_{\text{Age}} \approx 9 - 17$ Myr, if it formed from the passage of the nearest spiral arm; and $t_{\text{Age}} \approx 14 - 26$ Myr if it formed from the furthest arm. The second age range overlaps both with our earlier stellar cluster age estimate and with the age provided by Knapen et al. (1995) (who estimates an age of ~ 15 Myr for the majority of stars in the star-forming region coincident with SN 2020oi). Although neither of these estimates alone is conclusive evidence for the age of the SN 2020oi progenitor (and earlier passes of the material through the spiral arms could have equally triggered star formation events), in conjunction with the cluster age estimates from Prospector they present a consistent picture for its formation.

Using population synthesis models, Allard et al. (2006) finds that the spectral emission from the nuclear ring is equally well-explained by two models. In the first, an initial period of star formation ($t \sim 3$ Gyr ago) concludes and is followed only by the starburst event currently observed. In the second, the period of initial formation was followed by multiple continuous starburst events occurring every ~ 100 Myr and starting $t \sim 500$ Myr ago. Allard et al. (2006) favors the latter hypothesis, which is consistent with a continuous inflow of gas under the gravitational pumping action of the central bar.

While we are unable to distinguish between these two scenarios, our estimate of ~ 40 Myr for the age of the SN 2020oi cluster suggests that its formation corresponds to the most recent burst of star formation.

11.3. Metallicity and Star Formation at the Supernova Site

Because our IFU data span the inner region of M100, we can use traditional emission-line flux indicators to estimate the metallicity at the location of the SN. We employ the empirical relations derived by Marino et al. (2013) to estimate the metallicity at the SN 2020oi spectral bin location based on the $(\text{O III } \lambda 5007/\text{H}\beta)/(\text{N II } \lambda 6583/\text{H}\alpha)$ and $(\text{N II } \lambda 6583)/(\text{H}\alpha)$ line ratios (the O3N2 and N2 indices, respectively), as is appropriate for low-redshift HII regions:

$$12 + \log(\text{O}/\text{H}) = 8.743 + 0.462 \times \log(\text{N2}) \quad (7)$$

$$12 + \log(\text{O}/\text{H}) = 8.753 - 0.214 \times \log(\text{O3N2}) \quad (8)$$

Line fluxes have been measured on the spectrum obtained by the subtraction of the composite stellar population best-fit spectrum obtained from STARLIGHT with the observed spectrum (see Fig. 19). Using the N2 and O3N2 indices, we find a metallicity at the location of SN 2020oi of $12 + \log(\text{O}/\text{H}) = 8.50 \pm 0.01$ (± 0.18 sys), and $12 + \log(\text{O}/\text{H}) = 8.57 \pm 0.03$ (± 0.18 sys), respectively. Averaging these, we find $12 + \log(\text{O}/\text{H}) = 8.55 \pm 0.03$. Assuming a value for solar metallicity of $12 + \log(\text{O}/\text{H}) = 8.69$ (Asplund et al. 2009), the metallicity at the position of SN 2020oi is found to be slightly sub-solar. Another estimate for the metallicity comes from the final results of the STARLIGHT fits, where

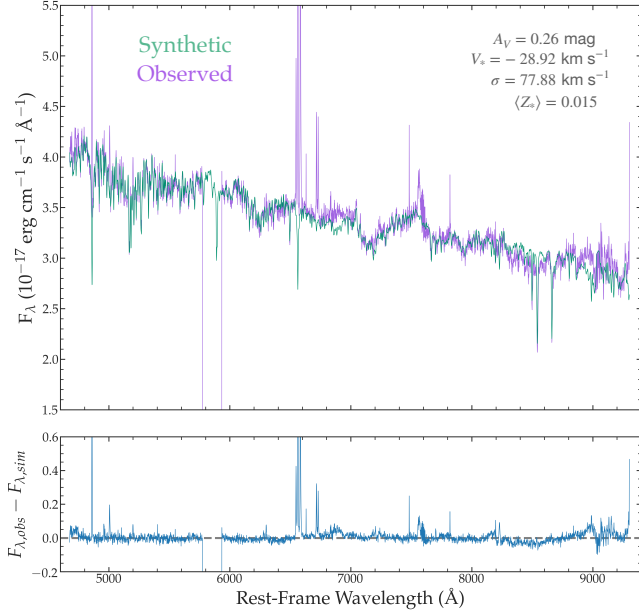


Figure 19. The spectrum at the bin of SN 2020oi as observed by MUSE (in violet). The composite stellar population spectrum obtained from STARLIGHT is shown in green. Emission-line fluxes have been measured from the residual spectrum, calculated by subtracting the synthetic spectrum by the observed spectrum. Host-galaxy extinction has been calculated internally from emission-line fluxes.

we have averaged the metallicities of each stellar base with its corresponding stellar mass weighted by the eigenvalues of the results obtained. From the analysis of the spectral bin corresponding to the location of SN 2020oi we find $\langle Z \rangle = 0.015$, where the Solar value is $Z_{\odot} = 0.02$. We conclude that the stellar metallicity inferred from the analysis of the stellar population underlying the SN is consistent with the metallicity obtained from the analysis of the nebular gas. Both values are also consistent with the average values for the gas-phase and stellar metallicities found from the analysis of a IFU-data sample of type-Ic SN host galaxies (Galbany et al. 2016).

We have also estimated the star-formation rate at the location of SN 2020oi using the method delineated in Kennicutt (1998), which is based on the luminosity of the extinction-corrected H α recombination line, $L_{H\alpha} = 6.9 \pm 1.4 \times 10^{37}$ erg s $^{-1}$: we obtain an effective star-formation rate of $\text{SFR} = 6.0 \pm 1.2 \times 10^{-3} M_{\odot} \text{ yr}^{-1} \text{ kpc}^{-2}$. This value is lower than the average SFR value found in a systematic analysis of type-Ic SN local environments (Galbany et al. 2018).

12. DEDUCING THE PROPERTIES OF THE SN 2020oi PROGENITOR

The estimated mass ejected in the explosion has strong implications for its progenitor system. We evaluate these implications by comparing our results to events simulated using the binary and single-star models from v2.2 of the Binary

Population And Spectral Synthesis (BPASS) code¹¹, which are described in detail in Eldridge et al. (2017). We constrain BPASS simulations to those consisting of a primary star with a CO-core mass greater than $1.38 M_{\odot}$ and a total mass greater than $1.5 M_{\odot}$ immediately pre-explosion, as progenitors less massive than this are unlikely to undergo core-collapse (Eldridge et al. 2017); and to only those systems containing a primary star with a hydrogen mass of less than $10^{-3} M_{\odot}$ immediately prior to explosion (the threshold reported in BPASS as corresponding to a stripped-envelope event). The resulting models span stellar metallicities from $Z = 10^{-5}$ to $Z = 0.04$. We plot the ejected mass for a fiducial SN explosion energy of 10^{51} erg (roughly corresponding to the energy of SN 2020oi) against the progenitor mass of the system at the beginning of the simulation in Figure 20. We find the M_{ej} value estimated for SN 2020oi near the lowest end of estimates for a system of initial mass $M_{\text{ZAMS}} \approx 6.5 - 13.0 M_{\odot}$, which occurs only in the simulated binary progenitor systems. The mean and median of initial progenitor masses within this subset of models are both $9.5 M_{\odot}$. Adopting this value and calculating the standard deviation across all viable models, we obtain a most-likely progenitor mass of $M_{\text{ZAMS}} = 9.5 \pm 1.0 M_{\odot}$. This value is lower than the initial mass predicted by Rho et al. (2021), who reports a value of $13 M_{\odot}$. As is also noted in Rho et al. (2021) (see their Table 2), the most likely initial progenitor mass predicted for SN 1994I, whose bolometric properties are similar to those of SN 2020oi, is $13 - 15 M_{\odot}$ (Iwamoto et al. 1994b; Sauer et al. 2006). Adopting our higher Arnett estimate of $M_{\text{ej}} = 1.00 M_{\odot}$ results in a higher progenitor mass of $M_{\text{ZAMS}} = 10 M_{\odot}$. This strongly suggests a low-mass binary progenitor origin for SN 2020oi.

Because we have derived a likelihood surface for the properties of our SN cluster from *HST* pre-explosion photometry in §10, we can combine our results with the derived properties of the explosion to extract a most likely age for the SN 2020oi progenitor.

From our likelihood surface, we first marginalize over the cluster metallicity and mass to obtain a probability density function for the age of the cluster. We then obtain a histogram of likely progenitor ages from BPASS by considering the ages of only the stellar models that result in a stripped-envelope explosion within the M_{ej} range predicted by the Khatami and Kasen fit to our bolometric light curve. As we note above, these models are all low-mass binary systems. We generate a kernel density estimate associated with this histogram, and then multiply our probability densities and normalize the result to obtain a combined probability density function for the age of the explosion. The resulting distribution is shown in Figure 21. The most likely age for the SN 2020oi progeni-

¹¹ <https://bpass.auckland.ac.nz/>

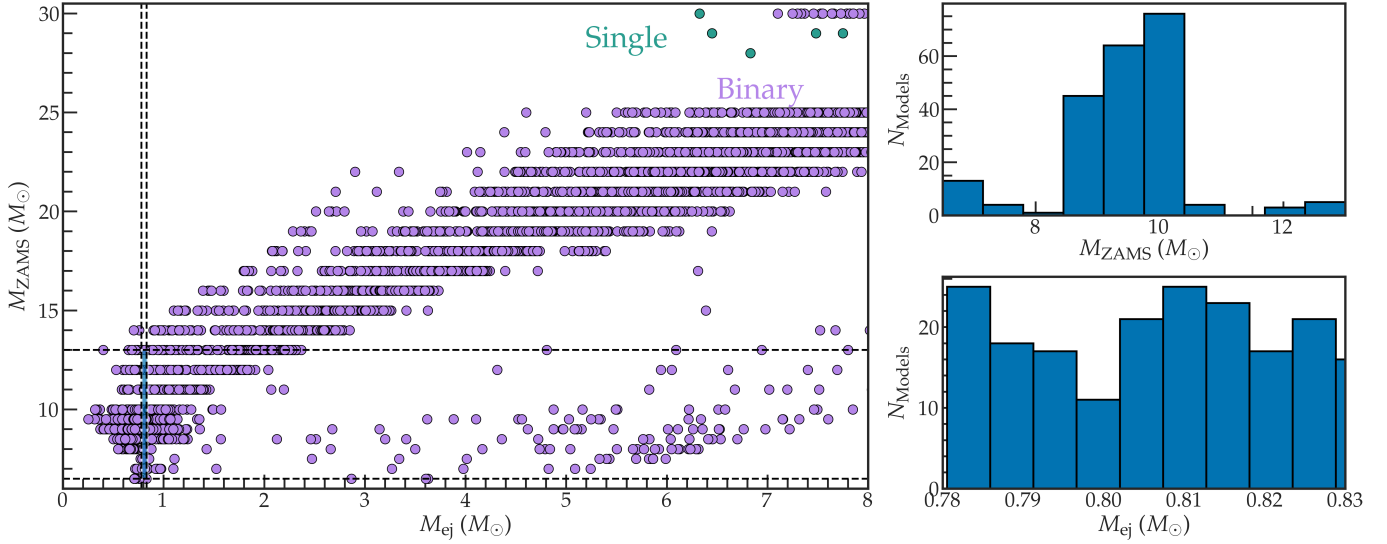


Figure 20. **Left:** The Zero-Age Main Sequence (ZAMS) mass of the progenitor star M_{ZAMS} versus the ejecta mass M_{ej} following explosion for single (green) and binary (violet) progenitor systems in BPASS. The blue shaded region captures the models in BPASS with predicted M_{ej} values within the range estimated for SN 2020oi. These models are weighted by the initial mass function with properties determined by Moe & Di Stefano (2017) to reproduce observed binary populations. **Right Upper Panel:** The distribution of M_{ZAMS} values for the models within the blue shaded region at left. Considering only these models, the most likely mass for the SN progenitor is $9.5 M_{\odot}$. **Right Lower Panel:** The range of M_{ej} values for the same set of models as above.

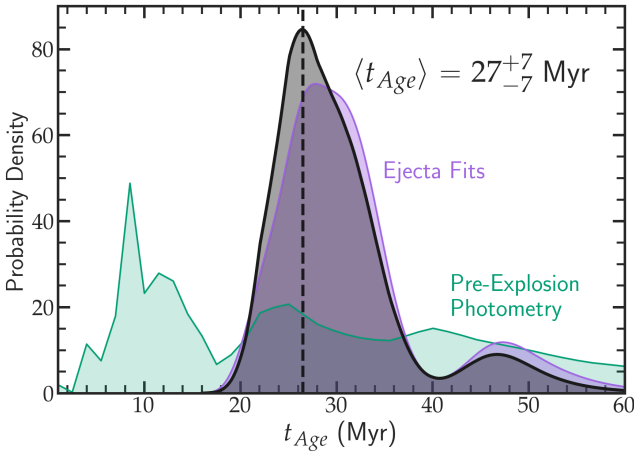


Figure 21. The probability density functions (PDFs) associated with the age of the SN 2020oi progenitor. The estimates derived from pre-explosion cluster photometry are given in green, and those derived from comparing explosion parameters to stellar evolution models are given in violet. The normalized probability density found by combining these two estimates are given as the black PDF at center, and the age with highest posterior probability is reported at right along with the standard deviation of the combined PDF.

tor is found by calculating the peak of the probability density function, and the uncertainty is reported by taking its standard deviation.

From these estimates, we calculate a final progenitor age of $t_{\text{Age}} = 27 \pm 7$ Myr. Although none of the previous SN 2020oi studies constrained the age of the progenitor, this estimate is in general agreement with simulations of stripped-envelope SNe

from binary systems (a $3 M_{\odot}$ helium core pre-explosion is expected to be ~ 19 Myr old, compared to our $2.1 M_{\odot}$ density distribution; see Rimoldi et al. 2016). Combined with the explosion parameters from previous sections and the derived progenitor mass of $M_{\text{ZAMS}} = 9.5 \pm 1.0 M_{\odot}$, our analysis strongly disfavors a single massive Wolf-Rayet as progenitor for the explosion (Crockett et al. 2008; Dessart et al. 2011).

13. DISCUSSION AND CONCLUSION

We have presented photometric and spectroscopic observations of the type-Ic SN 2020oi, which resides in the grand-design spiral galaxy M100. Our observations were obtained using Keck, SOAR, and other ground-based telescopes and span ~ 400 days of the event, allowing us to characterize the explosion in detail. Additional pre-explosion *HST* photometry and MUSE IFU spectroscopy has permitted a detailed investigation of the underlying stellar population at the location of the SN. Table 6 lists the properties of both the SN and its host environment derived in previous sections.

Below, we summarize the primary conclusions associated with our analysis:

1. Using the bolometric light curve code Superbol in tandem with a Gaussian Process routine to interpolate our photometric observations, we find SN 2020oi to be dimmer than the majority of SNe Ic and with a photometric evolution similar to that of the type-Ic SN 1994I. We calculate a luminosity decline rate of $\Delta m_{15, \text{bol}} \approx 1.6$, higher than all stripped-envelope SNe analyzed in both Lyman et al. (2016) and Taddia et al. (2018).

Table 6. Derived Properties of SN 2020oi

SFR at SN Site [$M_{\odot} \text{ yr}^{-1} \text{ kpc}^{-2}$]	$6.0 \pm 1.2 \times 10^{-3}$
Metallicity at SN Site ($\langle Z_{*} \rangle$) [Z_{\odot}]	~ 0.75
Total Reddening ($E(B - V)$) [mag]	0.133 ± 0.03
Cluster Age (t_{Clust}) [Myr]	40^{+30}_{-20}
Cluster Mass (M_{Clust}) [M_{\odot}]	$7.24^{+2.33}_{-4.33} \times 10^5$
Cluster Metallicity (Z_{Clust}) [Z_{\odot}]	0.03 ± 0.02
Date of Explosion (t_{exp}) [MJD]	58854.0 ± 0.3
Bolometric Decline Rate ($\Delta m_{15, \text{bol}}$)	1.63 ± 0.14
Kinetic Energy (E_k) [10^{51} erg]	0.79 ± 0.09
Ejecta Mass (M_{ej}) [M_{\odot}]	0.81 ± 0.03
Mass of Synthesized ^{56}Ni (M_{Ni56}) [M_{\odot}]	0.08 ± 0.02
Progenitor ZAMS Mass (M_{ZAMS}) [M_{\odot}]	9.5 ± 1.0
Progenitor Pre-Explosion Mass (M_f) [M_{\odot}]	~ 2.1
Progenitor Mass-Loss Rate (\dot{M}) [$M_{\odot} \text{ yr}^{-1}$]	$\sim 1.5 \times 10^{-4}$
Progenitor Age (t_{Age}) [Myr]	27 ± 7

2. We separately model the bolometric luminosity of the event in the photospheric phase using the modified one-component Arnett model described in [Valenti et al. \(2008\)](#) and following the [Khatami & Kasen \(2019\)](#) treatment for stripped-envelope SNe. We further use the MOSFiT code ([Guillochon et al. 2018](#)) to model the photoemetry of the event in each observed band. Adopting the results from [Khatami & Kasen \(2019\)](#), we find a mass of synthesized nickel of $M_{\text{Ni56}} = 0.08 \pm 0.02 M_{\odot}$ and a total ejecta mass of $M_{\text{ej}} = 0.81 \pm 0.03 M_{\odot}$. These values fall at the lowest end of the range reported by [Taddia et al. \(2018\)](#) for SNe Ic, a result consistent with the faint bolometric light curve and the rapid decline of the explosion. We derive an explosion time of MJD 58854.0 ± 0.3 using a fireball rise model applied to the first 10 days of photometry.
3. Detailed 1D spectral modeling using the radiative transfer code TARDIS reveals a composition near peak in strong agreement with the CO21 model developed to explain the spectral sequence of SN 1994I. We find evidence of Ca II, Mg II, Fe II, Si II, and O II features and a best-fit composition that remains roughly consistent across the epochs simulated, indicating at least partial ejecta mixing.
4. The earliest spectrum obtained ($\delta t = 3.3\text{d}$) features an enhanced blue continuum that cannot be explained by the SN 1994I CO21 composition model. Further, we find evidence of Fe II $\lambda 4500$ but not O I $\lambda 7773$, indicating that this material is associated with the outermost layers of the ejecta but contains higher-mass

elements typically observed at later epochs. We have obtained reasonable fits to this spectrum by considering an additional high-velocity ($< -23000 \text{ km s}^{-1}$) gas component ($0.1 M_{\odot}$) to the emission, with a distinct composition to the primary ejecta that includes carbon and potentially helium.

5. The optical and UV photometry near $\delta t \approx 2.5$ days reveals emission in excess of the expanding-fireball model. This excess is present in data obtained with Las Cumbres Observatory and with *Swift*. We have considered several physical scenarios to explain this emission, including shock-cooling, binary interaction, CSM interaction, and an asymmetric distribution of nickel synthesized from the explosion. We slightly favor the interpretation of ejecta interaction with CSM material, potentially from wave-driven mass-loss or mass transfer onto the companion at the time of the explosion. Nevertheless, until a more complete picture of the diversity of possible signatures from each of these phenomena is known, we cannot rule out alternative interaction mechanisms. The flux excess could also potentially be explained by properties intrinsic to the type-Ic explosion; early observations of a statistical sample of events are needed to investigate this possibility.
6. We have identified a marginally-extended source, likely a stellar cluster, coincident with the explosion in *HST* pre-explosion imaging. By combining stellar evolution models from BPASS with modeling of the cluster photometry in Prospector, we derive an age for the SN 2020oi progenitor of 27 ± 7 Myr. This age is consistent with values predicted from previous starburst evolution models ([Knapen et al. 1995](#); [Allard et al. 2006](#)), and with the conceptual picture of the progenitor forming from dynamical interaction of the innermost spiral arms with cold gas in M100's nuclear ring. This is the sole SN of seven discovered in M100 whose location has allowed us to validate the mechanism underlying star formation in the nuclear ring.
7. Our age constraints, coupled with an initial mass of $M_{\text{ZAMS}} \approx 9.5 M_{\odot}$ predicted from BPASS models and a pre-explosion mass of $M_f \approx 2.1 M_{\odot}$ estimated from spectral modeling in TARDIS, present a consistent picture of a low-mass binary progenitor system for SN 2020oi. An explanation for the optical/UV excess and early spectrum of the explosion must be consistent with a binary progenitor system. The possibility of an explosion during an episode of mass-transfer will be examined in greater detail in a subsequent paper.

The results of this study highlight the value of early-time observations in constraining the nature of SN progenitors. From its initial discovery, SN 2020oi was closely monitored

by the Young Supernovae Experiment (YSE; Jones et al. 2021), which surveys 1,512 deg² of sky in *griz* bands using the Pan-STARRS telescopes to a median 5- σ depth of 21.5 mag. Although surveys such as the Vera Rubin Observatory’s Legacy Survey for Space and Time (LSST; Ivezić et al. 2019) will vastly expand our understanding of the diversity of stripped-envelope SNe, high-cadence photometry and spectroscopy from additional surveys such as YSE will be critical for distinguishing between progenitor models and expanding our sample of observed short-duration phenomena (as in the case of the type-Ia SN 2018oh, observed by *TESS*; Dimitriadis et al. 2019). SN 2020oi is only the fourth spectroscopically-standard SN Ic with excess flux detected pre-maximum, and this dearth of sufficient analogues for comparison challenges our ability to conclusively characterize this emission. Rapid follow-up of events identified in large surveys will allow us to construct a statistical sample of early-time phenomena and more accurately distinguish between their signatures.

ACKNOWLEDGEMENTS

We acknowledge V. Alarcon, K. Clever, A. Dhara, J. Lopez, S. Medallon, J. Nunez, C. Smith, and E. Strasburger for help with the Nickel observations presented in this paper. We further acknowledge J. A. Vilchez, A. Campillay, Y. K. Riveros and N. Ulloa for their assistance with the Swope observations.

A.G. is supported by the National Science Foundation Graduate Research Fellowship Program under Grant No. DGE-1746047. A.G. also acknowledges funding from the Center for Astrophysical Surveys Fellowship at UIUC/NCSA and the Illinois Distinguished Fellowship.

W.J-G is supported by the National Science Foundation Graduate Research Fellowship Program under Grant No. DGE-1842165 and the IDEAS Fellowship Program at Northwestern University. W.J-G acknowledges support through NASA grants in support of *Hubble Space Telescope* program GO-16075.

Parts of this research were supported by the Australian Research Council Centre of Excellence for All Sky Astrophysics in 3 Dimensions (ASTRO 3D), through project number CE170100013.

M.R.D. acknowledges support from the NSERC through grant RGPIN-2019-06186, the Canada Research Chairs Program, the Canadian Institute for Advanced Research (CIFAR), and the Dunlap Institute at the University of Toronto.

The UCSC team is supported in part by NASA grant 80NSSC20K0953; NSF grant AST-1815935; the Gordon & Betty Moore Foundation; the Heising-Simons Foundation; and by a fellowship from the David and Lucile Packard Foundation to R.J.F.

The transient group at Northwestern is partially supported by the Heising-Simons Foundation under grant #2018-0911 (PI: Margutti). R.M. acknowledges support by the National

Science Foundation under Award No. AST-1909796 and AST-1944985. Support for this work was provided by the National Aeronautics and Space Administration through Chandra Award Number DD0-21114X (PI Stroh) issued by the Chandra X-ray Center, which is operated by the Smithsonian Astrophysical Observatory for and on behalf of the National Aeronautics Space Administration under contract NAS8-03060.

D.O.J. is supported by NASA through the NASA Hubble Fellowship grant HF2-51462.001 awarded by the Space Telescope Science Institute, which is operated by the Association of Universities for Research in Astronomy, Inc., for NASA, under contract NAS5-26555. D. A. Coulter acknowledges support from the National Science Foundation Graduate Research Fellowship under Grant DGE1339067. This work was supported by a VILLUM FONDEN Young Investigator Grant to C.G. (project number 25501) and a VILLUM FONDEN Investigator grant to J.H. (project number 16599). K.S.M. acknowledges funding from the European Research Council under the European Union’s Horizon 2020 research and innovation programme (Grant agreement No. 101002652), and from Horizon 2020, EU Grant agreement No. 873089. M.R.S. is supported by the National Science Foundation Graduate Research Fellowship Program under Grant No. 1842400.

The scientific results reported in this article are based in part on observations made by the Chandra X-ray Observatory. This research has made use of software provided by the Chandra X-ray Center (CXC) in the application packages CIAO. Partial support for this work was provided by the National Aeronautics and Space Administration through Chandra Award Number DD0-21114X issued by the Chandra X-ray Center, which is operated by the Smithsonian Astrophysical Observatory for and on behalf of the National Aeronautics Space Administration under contract NAS8-03060.

The Pan-STARRS1 Surveys (PS1) and the PS1 public science archive have been made possible through contributions by the Institute for Astronomy, the University of Hawaii, the Pan-STARRS Project Office, the Max-Planck Society and its participating institutes, the Max Planck Institute for Astronomy, Heidelberg and the Max Planck Institute for Extraterrestrial Physics, Garching, The Johns Hopkins University, Durham University, the University of Edinburgh, the Queen’s University Belfast, the Harvard-Smithsonian Center for Astrophysics, the Las Cumbres Observatory Global Telescope Network Incorporated, the National Central University of Taiwan, the Space Telescope Science Institute, the National Aeronautics and Space Administration under Grant No. NNX08AR22G issued through the Planetary Science Division of the NASA Science Mission Directorate, the National Science Foundation Grant No. AST-1238877, the University of Maryland, Eotvos Lorand University (ELTE), the

Los Alamos National Laboratory, and the Gordon and Betty Moore Foundation.

This work makes use of observations from the FLOYDS spectrograph on the LCOGT 2m telescope at Siding Spring. This work also makes use of observations from the Las Cumbres Observatory global telescope network (NOIRLab Prop. IDs 2019B-0250, 2020A-0334; PI: R. Foley).

A major upgrade of the Kast spectrograph on the Shane 3m telescope at Lick Observatory was made possible through generous gifts from the Heising-Simons Foundation as well as William and Marina Kast. Research at Lick Observatory is partially supported by a generous gift from Google.

Some of the data presented herein were obtained at the W. M. Keck Observatory, which is operated as a scientific partnership among the California Institute of Technology, the University of California and the National Aeronautics and Space Administration. The Observatory was made possible by the generous financial support of the W. M. Keck Foundation.

The authors wish to recognize and acknowledge the very significant cultural role and reverence that the summit of Maunakea has always had within the indigenous Hawaiian community. We are most fortunate to have the opportunity to conduct observations from this mountain. We further acknowledge that Lick Observatory sits on the unceded ancestral homelands of the Chochenyo and Tamyen Ohlone peoples, including the Alson and Socostac tribes, who were the original inhabitants of the area that includes Mt. Hamilton.

Based in part on observations obtained at the Southern Astrophysical Research (SOAR) telescope (NOIRLab Prop. IDs 2019B-0251, 2020A-0333; PI: R. Foley), which is a joint project of the Ministério da Ciência, Tecnologia e Inovações do Brasil (MCTI/LNA), the US National Science Founda-

tion’s NOIRLab, the University of North Carolina at Chapel Hill (UNC), and Michigan State University (MSU).

We acknowledge the use of public data from the Neil Gehrels *Swift* Observatory data archive.

Based on observations obtained with the Samuel Oschin 48-inch Telescope at the Palomar Observatory as part of the Zwicky Transient Facility project. ZTF is supported by the National Science Foundation under Grant No. AST-1440341 and a collaboration including Caltech, IPAC, the Weizmann Institute for Science, the Oskar Klein Center at Stockholm University, the University of Maryland, the University of Washington, Deutsches Elektronen-Synchrotron and Humboldt University, Los Alamos National Laboratories, the TANGO Consortium of Taiwan, the University of Wisconsin at Milwaukee, and Lawrence Berkeley National Laboratories. Operations are conducted by COO, IPAC, and UW. The ZTF forced-photometry service was funded under the Heising-Simons Foundation grant #12540303 (PI: Graham).

Software: BPASS (v2.2; Eldridge et al. 2017), CIAO (v4.13; Fruscione et al. 2006), DoPhot (Schechter et al. 1993), drizzlepac (Gonzaga et al. 2012), dynesty (Speagle 2020), emcee (Foreman-Mackey et al. 2013), HOTPANTS (Becker 2015), numpy (Walt et al. 2011), pandas (pandas development team 2020), photpipe (Rest et al. 2005; Kilpatrick et al. 2018a), photutils (Bradley et al. 2020), Prospector (Leja et al. 2017), PSFR (Fusco et al. 2020), Scipy (Jones et al. 2001), Superbol (Nicholl 2018), SWarp (Bertin 2010), STARLIGHT (Cid Fernandes et al. 2005), TARDIS (Kerzendorf & Sim 2014; Kerzendorf et al. 2018)

REFERENCES

- Afsariardchi, N., Drout, M. R., Khatami, D., et al. 2020, arXiv e-prints, arXiv:2009.06683. <https://arxiv.org/abs/2009.06683>
- Aldering, G., Humphreys, R. M., & Richmond, M. 1994, AJ, 107, 662, doi: [10.1086/116886](https://doi.org/10.1086/116886)
- Aleo, P. D., Sobotka, A. C., & Ramírez, I. 2017, ApJ, 846, 24, doi: [10.3847/1538-4357/aa83b6](https://doi.org/10.3847/1538-4357/aa83b6)
- Allard, E. L., Knapen, J. H., Peletier, R. F., & Sarzi, M. 2006, MNRAS, 371, 1087, doi: [10.1111/j.1365-2966.2006.10751.x](https://doi.org/10.1111/j.1365-2966.2006.10751.x)
- Allard, E. L., Peletier, R. F., & Knapen, J. H. 2005, ApJL, 633, L25, doi: [10.1086/498264](https://doi.org/10.1086/498264)
- Ambikasaran, S., Foreman-Mackey, D., Greengard, L., Hogg, D. W., & O’Neil, M. 2015, IEEE Transactions on Pattern Analysis and Machine Intelligence, 38, 252, doi: [10.1109/TPAMI.2015.2448083](https://doi.org/10.1109/TPAMI.2015.2448083)
- Anderson, J. P. 2019, A&A, 628, A7, doi: [10.1051/0004-6361/201935027](https://doi.org/10.1051/0004-6361/201935027)
- Arnett, W. D. 1982, ApJ, 253, 785, doi: [10.1086/159681](https://doi.org/10.1086/159681)
- Asplund, M., Grevesse, N., Sauval, A. J., & Scott, P. 2009, ARA&A, 47, 481, doi: [10.1146/annurev.astro.46.060407.145222](https://doi.org/10.1146/annurev.astro.46.060407.145222)
- Azeez, J. H., Hwang, C. Y., Abidin, Z. Z., & Ibrahim, Z. A. 2016, Scientific Reports, 6, 26896, doi: [10.1038/srep26896](https://doi.org/10.1038/srep26896)
- Barbarino, C., Botticella, M. T., Dall’Ora, M., et al. 2017, MNRAS, 471, 2463, doi: [10.1093/mnras/stx1709](https://doi.org/10.1093/mnras/stx1709)
- Barbarino, C., Sollerman, J., Taddia, F., et al. 2020, arXiv e-prints, arXiv:2010.08392. <https://arxiv.org/abs/2010.08392>
- Barker, B. L., Harris, C. E., Warren, M. L., O’Connor, E. P., & Couch, S. M. 2021, arXiv e-prints, arXiv:2102.01118. <https://arxiv.org/abs/2102.01118>
- Baron, E., Branch, D., Hauschildt, P. H., Filippenko, A. V., & Kirshner, R. P. 1999, ApJ, 527, 739, doi: [10.1086/308107](https://doi.org/10.1086/308107)
- Becker, A. 2015, HOTPANTS: High Order Transform of PSF AND Template Subtraction. <http://ascl.net/1504.004>

- Bellm, E. C., Kulkarni, S. R., Graham, M. J., et al. 2019a, *PASP*, 131, 018002, doi: [10.1088/1538-3873/aaecbe](https://doi.org/10.1088/1538-3873/aaecbe)
- Bellm, E. C., Kulkarni, S. R., Barlow, T., et al. 2019b, *PASP*, 131, 068003, doi: [10.1088/1538-3873/ab0c2a](https://doi.org/10.1088/1538-3873/ab0c2a)
- Bersten, M. C., Tanaka, M., Tominaga, N., Benvenuto, O. G., & Nomoto, K. 2013, *ApJ*, 767, 143, doi: [10.1088/0004-637X/767/2/143](https://doi.org/10.1088/0004-637X/767/2/143)
- Bersten, M. C., Folatelli, G., García, F., et al. 2018, *Nature*, 554, 497, doi: [10.1038/nature25151](https://doi.org/10.1038/nature25151)
- Bertin, E. 2010, SWarp: Resampling and Co-adding FITS Images Together. <http://ascl.net/1010.068>
- Bradley, L., Sipőcz, B., Robitaille, T., et al. 2020, *astropy/photutils*: 1.0.1, 1.0.1, Zenodo, doi: [10.5281/zenodo.4049061](https://doi.org/10.5281/zenodo.4049061)
- Brown, D. I. 1992, WFC2 Science Capability Report, Space Telescope WFC2 Instrument Science Report
- Brown, P. J., Breeveld, A. A., Holland, S., Kuin, P., & Pritchard, T. 2014, *Ap&SS*, 354, 89, doi: [10.1007/s10509-014-2059-8](https://doi.org/10.1007/s10509-014-2059-8)
- Brown, P. J., Holland, S. T., Immler, S., et al. 2009, *AJ*, 137, 4517, doi: [10.1088/0004-6256/137/5/4517](https://doi.org/10.1088/0004-6256/137/5/4517)
- Brown, T. M., Baliber, N., Bianco, F. B., et al. 2013, *PASP*, 125, 1031, doi: [10.1086/673168](https://doi.org/10.1086/673168)
- Bruzual, G., & Charlot, S. 2003, *MNRAS*, 344, 1000, doi: [10.1046/j.1365-8711.2003.06897.x](https://doi.org/10.1046/j.1365-8711.2003.06897.x)
- Calzetti, D., Armus, L., Bohlin, R. C., et al. 2000, *ApJ*, 533, 682, doi: [10.1086/308692](https://doi.org/10.1086/308692)
- Campana, S., Mangano, V., Blustin, A. J., et al. 2006, *Nature*, 442, 1008, doi: [10.1038/nature04892](https://doi.org/10.1038/nature04892)
- Cano, Z. 2013, *MNRAS*, 434, 1098, doi: [10.1093/mnras/stt1048](https://doi.org/10.1093/mnras/stt1048)
- Cao, Y., Kasliwal, M. M., Arcavi, I., et al. 2013, *ApJL*, 775, L7, doi: [10.1088/2041-8205/775/1/L7](https://doi.org/10.1088/2041-8205/775/1/L7)
- Cappellari, M., & Copin, Y. 2003, *MNRAS*, 342, 345, doi: [10.1046/j.1365-8711.2003.06541.x](https://doi.org/10.1046/j.1365-8711.2003.06541.x)
- Cardelli, J. A., Clayton, G. C., & Mathis, J. S. 1989, *ApJ*, 345, 245, doi: [10.1086/167900](https://doi.org/10.1086/167900)
- Carney, B. W. 1980, *PASP*, 92, 56, doi: [10.1086/130614](https://doi.org/10.1086/130614)
- Castillo-Morales, A., Jiménez-Vicente, J., Mediavilla, E., & Battaner, E. 2007, *MNRAS*, 380, 489, doi: [10.1111/j.1365-2966.2007.12104.x](https://doi.org/10.1111/j.1365-2966.2007.12104.x)
- Chabrier, G. 2003, *PASP*, 115, 763, doi: [10.1086/376392](https://doi.org/10.1086/376392)
- Chandra, P. 2018, *SSRv*, 214, 27, doi: [10.1007/s11214-017-0461-6](https://doi.org/10.1007/s11214-017-0461-6)
- Chevalier, R. A. 1982, *ApJ*, 258, 790, doi: [10.1086/160126](https://doi.org/10.1086/160126)
- . 1998, *ApJ*, 499, 810, doi: [10.1086/305676](https://doi.org/10.1086/305676)
- Chevalier, R. A., & Fransson, C. 2006, *ApJ*, 651, 381, doi: [10.1086/507606](https://doi.org/10.1086/507606)
- Cid Fernandes, R., Mateus, A., Sodré, L., Stasińska, G., & Gomes, J. M. 2005, *MNRAS*, 358, 363, doi: [10.1111/j.1365-2966.2005.08752.x](https://doi.org/10.1111/j.1365-2966.2005.08752.x)
- Clemens, J. C., Crain, J. A., & Anderson, R. 2004, in *Society of Photo-Optical Instrumentation Engineers (SPIE) Conference Series*, Vol. 5492, *Ground-based Instrumentation for Astronomy*, ed. A. F. M. Moorwood & M. Iye, 331–340, doi: [10.1117/12.550069](https://doi.org/10.1117/12.550069)
- Crockett, R. M., Maund, J. R., Smartt, S. J., et al. 2008, *ApJL*, 672, L99, doi: [10.1086/527299](https://doi.org/10.1086/527299)
- De, K., Kasliwal, M. M., Ofek, E. O., et al. 2018, *Science*, 362, 201, doi: [10.1126/science.aas8693](https://doi.org/10.1126/science.aas8693)
- Dessart, L., Hillier, D. J., Livne, E., et al. 2011, *MNRAS*, 414, 2985, doi: [10.1111/j.1365-2966.2011.18598.x](https://doi.org/10.1111/j.1365-2966.2011.18598.x)
- Dierckx, P. 1995, *Curve and surface fitting with splines* (Oxford University Press)
- Dimitriadis, G., Foley, R. J., Rest, A., et al. 2019, *ApJL*, 870, L1, doi: [10.3847/2041-8213/aeddb0](https://doi.org/10.3847/2041-8213/aeddb0)
- Drout, M. R., Soderberg, A. M., Gal-Yam, A., et al. 2011, *ApJ*, 741, 97, doi: [10.1088/0004-637X/741/2/97](https://doi.org/10.1088/0004-637X/741/2/97)
- Drout, M. R., Milisavljevic, D., Parrent, J., et al. 2016, *ApJ*, 821, 57, doi: [10.3847/0004-637X/821/1/57](https://doi.org/10.3847/0004-637X/821/1/57)
- Eldridge, J. J., Izzard, R. G., & Tout, C. A. 2008, *MNRAS*, 384, 1109, doi: [10.1111/j.1365-2966.2007.12738.x](https://doi.org/10.1111/j.1365-2966.2007.12738.x)
- Eldridge, J. J., Stanway, E. R., Xiao, L., et al. 2017, *PASA*, 34, e058, doi: [10.1017/pasa.2017.51](https://doi.org/10.1017/pasa.2017.51)
- Elmegreen, B. G., Elmegreen, D. M., & Efremov, Y. N. 2018, *ApJ*, 863, 59, doi: [10.3847/1538-4357/aacf9a](https://doi.org/10.3847/1538-4357/aacf9a)
- Filippenko, A. V., Barth, A. J., Matheson, T., et al. 1995, *ApJL*, 450, L11, doi: [10.1086/309659](https://doi.org/10.1086/309659)
- Flewelling, H. A., Magnier, E. A., Chambers, K. C., et al. 2020, *ApJS*, 251, 7, doi: [10.3847/1538-4365/abb82d](https://doi.org/10.3847/1538-4365/abb82d)
- Folatelli, G., Van Dyk, S. D., Kuncarayakti, H., et al. 2016, *ApJL*, 825, L22, doi: [10.3847/2041-8205/825/2/L22](https://doi.org/10.3847/2041-8205/825/2/L22)
- Foley, R. J., Chornock, R., Filippenko, A. V., et al. 2009, *AJ*, 138, 376, doi: [10.1088/0004-6256/138/2/376](https://doi.org/10.1088/0004-6256/138/2/376)
- Foreman-Mackey, D., Hogg, D. W., Lang, D., & Goodman, J. 2013, *PASP*, 125, 306, doi: [10.1086/670067](https://doi.org/10.1086/670067)
- Forster, F., Pignata, G., Bauer, F. E., et al. 2020, *Transient Name Server Discovery Report*, 2020-67, 1
- Fox, O. D., Filippenko, A. V., Skrutskie, M. F., et al. 2013, *AJ*, 146, 2, doi: [10.1088/0004-6256/146/1/2](https://doi.org/10.1088/0004-6256/146/1/2)
- Freedman, W. L., Madore, B. F., Mould, J. R., et al. 1994a, *Nature*, 371, 757, doi: [10.1038/371757a0](https://doi.org/10.1038/371757a0)
- Freedman, W. L., Madore, B. F., Stetson, P. B., et al. 1994b, *ApJL*, 435, L31, doi: [10.1086/187587](https://doi.org/10.1086/187587)
- Fremling, C., Ko, H., Dugas, A., et al. 2019, *ApJL*, 878, L5, doi: [10.3847/2041-8213/ab218f](https://doi.org/10.3847/2041-8213/ab218f)
- Fruscione, A., McDowell, J. C., Allen, G. E., et al. 2006, in *Society of Photo-Optical Instrumentation Engineers (SPIE) Conference Series*, Vol. 6270, *Society of Photo-Optical Instrumentation Engineers (SPIE) Conference Series*, ed. D. R. Silva & R. E. Doxsey, 62701V, doi: [10.1117/12.671760](https://doi.org/10.1117/12.671760)

- Fusco, T., Bacon, R., Kamann, S., et al. 2020, *A&A*, 635, A208, doi: [10.1051/0004-6361/202037595](https://doi.org/10.1051/0004-6361/202037595)
- Gal-Yam, A. 2017, *Observational and Physical Classification of Supernovae*, ed. A. W. Alsabti & P. Murdin, 195, doi: [10.1007/978-3-319-21846-5_35](https://doi.org/10.1007/978-3-319-21846-5_35)
- Galbany, L., Anderson, J. P., Rosales-Ortega, F. F., et al. 2016, *MNRAS*, 455, 4087, doi: [10.1093/mnras/stv2620](https://doi.org/10.1093/mnras/stv2620)
- Galbany, L., Anderson, J. P., Sánchez, S. F., et al. 2018, *ApJ*, 855, 107, doi: [10.3847/1538-4357/aaaf20](https://doi.org/10.3847/1538-4357/aaaf20)
- Garcia-Burillo, S., Sempere, M. J., Combes, F., & Neri, R. 1998, *A&A*, 333, 864. <https://arxiv.org/abs/astro-ph/9803006>
- Garnavich, P. M., Tucker, B. E., Rest, A., et al. 2016, *ApJ*, 820, 23, doi: [10.3847/0004-637X/820/1/23](https://doi.org/10.3847/0004-637X/820/1/23)
- Gehrels, N., Chincarini, G., Giommi, P., et al. 2004, *ApJ*, 611, 1005, doi: [10.1086/422091](https://doi.org/10.1086/422091)
- Gilkis, A., Vink, J. S., Eldridge, J. J., & Tout, C. A. 2019, *MNRAS*, 486, 4451, doi: [10.1093/mnras/stz1134](https://doi.org/10.1093/mnras/stz1134)
- Gonzaga, S., Hack, W., Fruchter, A., & Mack, J. 2012, *The DrizzlePac Handbook*
- Götberg, Y., Korol, V., Lamberts, A., et al. 2020, *ApJ*, 904, 56, doi: [10.3847/1538-4357/abbda5](https://doi.org/10.3847/1538-4357/abbda5)
- Graham, M. J., Kulkarni, S. R., Bellm, E. C., et al. 2019, *PASP*, 131, 078001, doi: [10.1088/1538-3873/ab006c](https://doi.org/10.1088/1538-3873/ab006c)
- Groh, J. H., Georgy, C., & Ekström, S. 2013, *A&A*, 558, L1, doi: [10.1051/0004-6361/201322369](https://doi.org/10.1051/0004-6361/201322369)
- Guillochon, J., Nicholl, M., Villar, V. A., et al. 2018, *ApJS*, 236, 6, doi: [10.3847/1538-4365/aab761](https://doi.org/10.3847/1538-4365/aab761)
- Henault, F., Bacon, R., Bonneville, C., et al. 2003, in *Society of Photo-Optical Instrumentation Engineers (SPIE) Conference Series*, Vol. 4841, *Instrument Design and Performance for Optical/Infrared Ground-based Telescopes*, ed. M. Iye & A. F. M. Moorwood, 1096–1107, doi: [10.1117/12.462334](https://doi.org/10.1117/12.462334)
- Hernandez, O., Wozniak, H., Carignan, C., et al. 2005, *ApJ*, 632, 253, doi: [10.1086/431964](https://doi.org/10.1086/431964)
- Hill, R. J., Ferrarese, L., Stetson, P. B., et al. 1995, in *Calibrating Hubble Space Telescope. Post Servicing Mission*, ed. A. P. Koratkar & C. Leitherer, 360
- Hjorth, J., Sollerman, J., Møller, P., et al. 2003, *Nature*, 423, 847, doi: [10.1038/nature01750](https://doi.org/10.1038/nature01750)
- Horesh, A., & Sfaradi, I. 2020, *Transient Name Server AstroNote*, 9, 1
- Horesh, A., Sfaradi, I., Ergon, M., et al. 2020, *ApJ*, 903, 132, doi: [10.3847/1538-4357/abbd38](https://doi.org/10.3847/1538-4357/abbd38)
- Ivezić, Ž., Kahn, S. M., Tyson, J. A., et al. 2019, *ApJ*, 873, 111, doi: [10.3847/1538-4357/ab042c](https://doi.org/10.3847/1538-4357/ab042c)
- Iwamoto, K., Nomoto, K., Höflich, P., et al. 1994a, *ApJL*, 437, L115, doi: [10.1086/187696](https://doi.org/10.1086/187696)
- . 1994b, *ApJL*, 437, L115, doi: [10.1086/187696](https://doi.org/10.1086/187696)
- Izzo, L., Auchettl, K., Hjorth, J., et al. 2020, *A&A*, 639, L11, doi: [10.1051/0004-6361/202038152](https://doi.org/10.1051/0004-6361/202038152)
- Jacobson-Galán, W. V., Margutti, R., Kilpatrick, C. D., et al. 2020, *ApJ*, 898, 166, doi: [10.3847/1538-4357/ab9e66](https://doi.org/10.3847/1538-4357/ab9e66)
- Jerkstrand, A. 2017, *Spectra of Supernovae in the Nebular Phase*, ed. A. W. Alsabti & P. Murdin, 795, doi: [10.1007/978-3-319-21846-5_29](https://doi.org/10.1007/978-3-319-21846-5_29)
- Jones, D. O., Foley, R. J., Narayan, G., et al. 2021, *ApJ*, 908, 143, doi: [10.3847/1538-4357/abd7f5](https://doi.org/10.3847/1538-4357/abd7f5)
- Jones, E., Oliphant, T., & Peterson, P. 2001
- Kalberla, P. M. W., Burton, W. B., Hartmann, D., et al. 2005, *A&A*, 440, 775, doi: [10.1051/0004-6361:20041864](https://doi.org/10.1051/0004-6361:20041864)
- Kasen, D. 2010, *ApJ*, 708, 1025, doi: [10.1088/0004-637X/708/2/1025](https://doi.org/10.1088/0004-637X/708/2/1025)
- Kelly, P. L., Fox, O. D., Filippenko, A. V., et al. 2014, *ApJ*, 790, 3, doi: [10.1088/0004-637X/790/1/3](https://doi.org/10.1088/0004-637X/790/1/3)
- Kennicutt, Robert C., J. 1998, *ARA&A*, 36, 189, doi: [10.1146/annurev.astro.36.1.189](https://doi.org/10.1146/annurev.astro.36.1.189)
- Kerzendorf, W., Nöbauer, U., Sim, S., et al. 2018, *Tardis-Sn/Tardis: Tardis V2.0.2 Release, v2.0.2*, Zenodo, doi: [10.5281/zenodo.1292315](https://doi.org/10.5281/zenodo.1292315)
- Kerzendorf, W. E., & Sim, S. A. 2014, *MNRAS*, 440, 387, doi: [10.1093/mnras/stu055](https://doi.org/10.1093/mnras/stu055)
- Khatami, D. K., & Kasen, D. N. 2019, *ApJ*, 878, 56, doi: [10.3847/1538-4357/ab1f09](https://doi.org/10.3847/1538-4357/ab1f09)
- Khazov, D., Yaron, O., Gal-Yam, A., et al. 2016, *ApJ*, 818, 3, doi: [10.3847/0004-637X/818/1/3](https://doi.org/10.3847/0004-637X/818/1/3)
- Kilpatrick, C. D., Foley, R. J., Abramson, L. E., et al. 2017, *MNRAS*, 465, 4650, doi: [10.1093/mnras/stw3082](https://doi.org/10.1093/mnras/stw3082)
- Kilpatrick, C. D., Takaro, T., Foley, R. J., et al. 2018a, *MNRAS*, 480, 2072, doi: [10.1093/mnras/sty2022](https://doi.org/10.1093/mnras/sty2022)
- Kilpatrick, C. D., Foley, R. J., Drout, M. R., et al. 2018b, *MNRAS*, 473, 4805, doi: [10.1093/mnras/stx2675](https://doi.org/10.1093/mnras/stx2675)
- Kilpatrick, C. D., Drout, M. R., Auchettl, K., et al. 2021, *arXiv e-prints*, arXiv:2101.03206. <https://arxiv.org/abs/2101.03206>
- Knapen, J. H., Beckman, J. E., Shlosman, I., et al. 1995, *ApJL*, 443, L73, doi: [10.1086/187839](https://doi.org/10.1086/187839)
- Knapen, J. H., Shlosman, I., Heller, C. H., et al. 2000, *ApJ*, 528, 219, doi: [10.1086/308162](https://doi.org/10.1086/308162)
- Kochanek, C. S., Fraser, M., Adams, S. M., et al. 2017, *MNRAS*, 467, 3347, doi: [10.1093/mnras/stx291](https://doi.org/10.1093/mnras/stx291)
- Kuncarayakti, H., Aldering, G., Anderson, J. P., et al. 2015, *Publication of Korean Astronomical Society*, 30, 139, doi: [10.5303/PKAS.2015.30.2.139](https://doi.org/10.5303/PKAS.2015.30.2.139)
- Kuncarayakti, H., Anderson, J. P., Galbany, L., et al. 2018, *A&A*, 613, A35, doi: [10.1051/0004-6361/201731923](https://doi.org/10.1051/0004-6361/201731923)
- Lang, D., Hogg, D. W., Mierle, K., Blanton, M., & Roweis, S. 2010, *AJ*, 139, 1782, doi: [10.1088/0004-6256/139/5/1782](https://doi.org/10.1088/0004-6256/139/5/1782)
- Laplace, E., Götberg, Y., de Mink, S. E., Justham, S., & Farmer, R. 2020, *A&A*, 637, A6, doi: [10.1051/0004-6361/201937300](https://doi.org/10.1051/0004-6361/201937300)
- Leja, J., Johnson, B. D., Conroy, C., van Dokkum, P. G., & Byler, N. 2017, *ApJ*, 837, 170, doi: [10.3847/1538-4357/aa5ffe](https://doi.org/10.3847/1538-4357/aa5ffe)

- Li, W., Leaman, J., Chornock, R., et al. 2011, MNRAS, 412, 1441, doi: [10.1111/j.1365-2966.2011.18160.x](https://doi.org/10.1111/j.1365-2966.2011.18160.x)
- Liu, Z.-W., Tauris, T. M., Röpke, F. K., et al. 2015, A&A, 584, A11, doi: [10.1051/0004-6361/201526757](https://doi.org/10.1051/0004-6361/201526757)
- Lucy, L. B. 1991, ApJ, 383, 308, doi: [10.1086/170787](https://doi.org/10.1086/170787)
- Lyman, J. D., Bersier, D., James, P. A., et al. 2016, MNRAS, 457, 328, doi: [10.1093/mnras/stv2983](https://doi.org/10.1093/mnras/stv2983)
- MacFadyen, A. I., & Woosley, S. E. 1999, ApJ, 524, 262, doi: [10.1086/307790](https://doi.org/10.1086/307790)
- Magee, M. R., & Maguire, K. 2020, A&A, 642, A189, doi: [10.1051/0004-6361/202037870](https://doi.org/10.1051/0004-6361/202037870)
- Magee, M. R., Sim, S. A., Kotak, R., & Kerzendorf, W. E. 2018, A&A, 614, A115, doi: [10.1051/0004-6361/201832675](https://doi.org/10.1051/0004-6361/201832675)
- Mandel, I., Müller, B., Riley, J., et al. 2021, MNRAS, 500, 1380, doi: [10.1093/mnras/staa3390](https://doi.org/10.1093/mnras/staa3390)
- Margutti, R., Soderberg, A. M., Chomiuk, L., et al. 2012, ApJ, 751, 134, doi: [10.1088/0004-637X/751/2/134](https://doi.org/10.1088/0004-637X/751/2/134)
- Margutti, R., Milisavljevic, D., Soderberg, A. M., et al. 2014, ApJ, 797, 107, doi: [10.1088/0004-637X/797/2/107](https://doi.org/10.1088/0004-637X/797/2/107)
- Marino, R. A., Rosales-Ortega, F. F., Sánchez, S. F., et al. 2013, A&A, 559, A114, doi: [10.1051/0004-6361/201321956](https://doi.org/10.1051/0004-6361/201321956)
- Masci, F. J., Laher, R. R., Rusholme, B., et al. 2019, PASP, 131, 018003, doi: [10.1088/1538-3873/aae8ac](https://doi.org/10.1088/1538-3873/aae8ac)
- Maund, J. R. 2017, MNRAS, 469, 2202, doi: [10.1093/mnras/stx879](https://doi.org/10.1093/mnras/stx879)
- Mazzali, P. A., Deng, J., Tominaga, N., et al. 2003, ApJL, 599, L95, doi: [10.1086/381259](https://doi.org/10.1086/381259)
- McCully, C., Volgenau, N. H., Harbeck, D.-R., et al. 2018, in Society of Photo-Optical Instrumentation Engineers (SPIE) Conference Series, Vol. 10707, Software and Cyberinfrastructure for Astronomy V, ed. J. C. Guzman & J. Ibsen, 107070K, doi: [10.1117/12.2314340](https://doi.org/10.1117/12.2314340)
- Meza, N., Prieto, J. L., Clocchiatti, A., et al. 2019, A&A, 629, A57, doi: [10.1051/0004-6361/201834972](https://doi.org/10.1051/0004-6361/201834972)
- Michałowski, M. J., Gotkiewicz, N., Hjorth, J., & Kamphuis, P. 2020, A&A, 638, A47, doi: [10.1051/0004-6361/202037692](https://doi.org/10.1051/0004-6361/202037692)
- Milisavljevic, D., Margutti, R., Kamble, A., et al. 2015, ApJ, 815, 120, doi: [10.1088/0004-637X/815/2/120](https://doi.org/10.1088/0004-637X/815/2/120)
- Millard, J., Branch, D., Baron, E., et al. 1999, ApJ, 527, 746, doi: [10.1086/308108](https://doi.org/10.1086/308108)
- Miller, J. S., & Stone, R. P. S. 1993, LOTRM
- Modjaz, M., Gutiérrez, C. P., & Arcavi, I. 2019, Nature Astronomy, 3, 717, doi: [10.1038/s41550-019-0856-2](https://doi.org/10.1038/s41550-019-0856-2)
- Modjaz, M., Li, W., Butler, N., et al. 2009, ApJ, 702, 226, doi: [10.1088/0004-637X/702/1/226](https://doi.org/10.1088/0004-637X/702/1/226)
- Moe, M., & Di Stefano, R. 2017, ApJS, 230, 15, doi: [10.3847/1538-4365/aa6fb6](https://doi.org/10.3847/1538-4365/aa6fb6)
- Morozova, V., Piro, A. L., Renzo, M., et al. 2015, ApJ, 814, 63, doi: [10.1088/0004-637X/814/1/63](https://doi.org/10.1088/0004-637X/814/1/63)
- Nadyozhin, D. K. 1994, ApJS, 92, 527, doi: [10.1086/192008](https://doi.org/10.1086/192008)
- Nagataki, S. 2018, Reports on Progress in Physics, 81, 026901, doi: [10.1088/1361-6633/aa97a8](https://doi.org/10.1088/1361-6633/aa97a8)
- Nicholl, M. 2018, Research Notes of the American Astronomical Society, 2, 230, doi: [10.3847/2515-5172/aaf799](https://doi.org/10.3847/2515-5172/aaf799)
- Nomoto, K., Yamaoka, H., Pols, O. R., et al. 1994, Nature, 371, 227, doi: [10.1038/371227a0](https://doi.org/10.1038/371227a0)
- Oke, J. B., Cohen, J. G., Carr, M., et al. 1995, PASP, 107, 375, doi: [10.1086/133562](https://doi.org/10.1086/133562)
- O'Neill, D., Kotak, R., Fraser, M., et al. 2019, A&A, 622, L1, doi: [10.1051/0004-6361/201834566](https://doi.org/10.1051/0004-6361/201834566)
- pandas development team, T. 2020, pandas-dev/pandas: Pandas, latest, Zenodo, doi: [10.5281/zenodo.3509134](https://doi.org/10.5281/zenodo.3509134)
- Phillips, M. M., Li, W., Frieman, J. A., et al. 2007, PASP, 119, 360, doi: [10.1086/518372](https://doi.org/10.1086/518372)
- Pignata, G., Stritzinger, M., Soderberg, A., et al. 2011, ApJ, 728, 14, doi: [10.1088/0004-637X/728/1/14](https://doi.org/10.1088/0004-637X/728/1/14)
- Piro, A. L. 2015, ApJL, 808, L51, doi: [10.1088/2041-8205/808/2/L51](https://doi.org/10.1088/2041-8205/808/2/L51)
- Piro, A. L., Haynie, A., & Yao, Y. 2021, ApJ, 909, 209, doi: [10.3847/1538-4357/abe2b1](https://doi.org/10.3847/1538-4357/abe2b1)
- Poznanski, D., Prochaska, J. X., & Bloom, J. S. 2012, MNRAS, 426, 1465, doi: [10.1111/j.1365-2966.2012.21796.x](https://doi.org/10.1111/j.1365-2966.2012.21796.x)
- Prentice, S. J., Ashall, C., James, P. A., et al. 2019, MNRAS, 485, 1559, doi: [10.1093/mnras/sty3399](https://doi.org/10.1093/mnras/sty3399)
- Quimby, R., Brown, P., Gerardy, C., Odewahn, S. C., & Rostopchin, S. 2006, Central Bureau Electronic Telegrams, 393, 1
- Rasmussen, C. E. 2006, in (MIT Press)
- Rest, A., Stubbs, C., Becker, A. C., et al. 2005, ApJ, 634, 1103, doi: [10.1086/497060](https://doi.org/10.1086/497060)
- Rho, J., Evans, A., Geballe, T. R., et al. 2021, ApJ, 908, 232, doi: [10.3847/1538-4357/abd850](https://doi.org/10.3847/1538-4357/abd850)
- Richmond, M. W., van Dyk, S. D., Ho, W., et al. 1996, AJ, 111, 327, doi: [10.1086/117785](https://doi.org/10.1086/117785)
- Rimoldi, A., Portegies Zwart, S., & Rossi, E. M. 2016, Computational Astrophysics and Cosmology, 3, 2, doi: [10.1186/s40668-016-0015-4](https://doi.org/10.1186/s40668-016-0015-4)
- Roming, P. W. A., Kennedy, T. E., Mason, K. O., et al. 2005, SSRv, 120, 95, doi: [10.1007/s11214-005-5095-4](https://doi.org/10.1007/s11214-005-5095-4)
- Ryder, S. D., & Knapen, J. H. 2001, Ap&SS, 276, 405, doi: [10.1023/A:1017578713184](https://doi.org/10.1023/A:1017578713184)
- Sahu, D. K., Anupama, G. C., Chakradhari, N. K., et al. 2018, MNRAS, 475, 2591, doi: [10.1093/mnras/stx3212](https://doi.org/10.1093/mnras/stx3212)
- Sakamoto, K., Okumura, S., Minezaki, T., Kobayashi, Y., & Wada, K. 1995, AJ, 110, 2075, doi: [10.1086/117670](https://doi.org/10.1086/117670)
- Sapir, N., & Waxman, E. 2017, ApJ, 838, 130, doi: [10.3847/1538-4357/aa64df](https://doi.org/10.3847/1538-4357/aa64df)
- Sauer, D. N., Mazzali, P. A., Deng, J., et al. 2006, MNRAS, 369, 1939, doi: [10.1111/j.1365-2966.2006.10438.x](https://doi.org/10.1111/j.1365-2966.2006.10438.x)
- Scalzo, R. A., Aldering, G., Antilogus, P., et al. 2010, ApJ, 713, 1073, doi: [10.1088/0004-637X/713/2/1073](https://doi.org/10.1088/0004-637X/713/2/1073)

- Schechter, P. L., Mateo, M., & Saha, A. 1993, *PASP*, 105, 1342, doi: [10.1086/133316](https://doi.org/10.1086/133316)
- Schlaflly, E. F., & Finkbeiner, D. P. 2011, *ApJ*, 737, 103, doi: [10.1088/0004-637X/737/2/103](https://doi.org/10.1088/0004-637X/737/2/103)
- Schmidt, B. P., Kirshner, R. P., Eastman, R. G., et al. 1993, *Nature*, 364, 600, doi: [10.1038/364600a0](https://doi.org/10.1038/364600a0)
- Shiode, J. H., & Quataert, E. 2014, *ApJ*, 780, 96, doi: [10.1088/0004-637X/780/1/96](https://doi.org/10.1088/0004-637X/780/1/96)
- Siebert, M. R., Dimitriadis, G., Polin, A., & Foley, R. J. 2020a, *ApJL*, 900, L27, doi: [10.3847/2041-8213/abae6e](https://doi.org/10.3847/2041-8213/abae6e)
- Siebert, M. R., Kilpatrick, C. D., Foley, R. J., & Cartier, R. 2020b, *Transient Name Server Classification Report*, 2020-90, 1
- Silverman, J. M., Foley, R. J., Filippenko, A. V., et al. 2012, *MNRAS*, 425, 1789, doi: [10.1111/j.1365-2966.2012.21270.x](https://doi.org/10.1111/j.1365-2966.2012.21270.x)
- Smartt, S. J. 2009, *ARA&A*, 47, 63, doi: [10.1146/annurev-astro-082708-101737](https://doi.org/10.1146/annurev-astro-082708-101737)
- . 2015, *PASA*, 32, e016, doi: [10.1017/pasa.2015.17](https://doi.org/10.1017/pasa.2015.17)
- Smartt, S. J., Maund, J. R., Gilmore, G. F., et al. 2003, *MNRAS*, 343, 735, doi: [10.1046/j.1365-8711.2003.06718.x](https://doi.org/10.1046/j.1365-8711.2003.06718.x)
- Smith, B. J., Struck, C., Hancock, M., et al. 2007, *AJ*, 133, 791, doi: [10.1086/510350](https://doi.org/10.1086/510350)
- Smith, N. 2014, *ARA&A*, 52, 487, doi: [10.1146/annurev-astro-081913-040025](https://doi.org/10.1146/annurev-astro-081913-040025)
- Smith, N., Li, W., Filippenko, A. V., & Chornock, R. 2011, *MNRAS*, 412, 1522, doi: [10.1111/j.1365-2966.2011.17229.x](https://doi.org/10.1111/j.1365-2966.2011.17229.x)
- Soderberg, A. M., Nakar, E., Berger, E., & Kulkarni, S. R. 2006a, *ApJ*, 638, 930, doi: [10.1086/499121](https://doi.org/10.1086/499121)
- Soderberg, A. M., Berger, E., Kasliwal, M., et al. 2006b, *ApJ*, 650, 261, doi: [10.1086/506429](https://doi.org/10.1086/506429)
- Soderberg, A. M., Kulkarni, S. R., Nakar, E., et al. 2006c, *Nature*, 442, 1014, doi: [10.1038/nature05087](https://doi.org/10.1038/nature05087)
- Soderberg, A. M., Berger, E., Page, K. L., et al. 2008, *Nature*, 453, 469, doi: [10.1038/nature06997](https://doi.org/10.1038/nature06997)
- Soderberg, A. M., Chakraborti, S., Pignata, G., et al. 2010, *Nature*, 463, 513, doi: [10.1038/nature08714](https://doi.org/10.1038/nature08714)
- Sollerman, J., Fransson, C., Barbarino, C., et al. 2020, *A&A*, 643, A79, doi: [10.1051/0004-6361/202038960](https://doi.org/10.1051/0004-6361/202038960)
- Speagle, J. S. 2020, *MNRAS*, 493, 3132, doi: [10.1093/mnras/staa278](https://doi.org/10.1093/mnras/staa278)
- Stritzinger, M. D., Taddia, F., Burns, C. R., et al. 2018, *A&A*, 609, A135, doi: [10.1051/0004-6361/201730843](https://doi.org/10.1051/0004-6361/201730843)
- Taddia, F., Fremling, C., Sollerman, J., et al. 2016, *A&A*, 592, A89, doi: [10.1051/0004-6361/201628703](https://doi.org/10.1051/0004-6361/201628703)
- Taddia, F., Stritzinger, M. D., Bersten, M., et al. 2018, *A&A*, 609, A136, doi: [10.1051/0004-6361/201730844](https://doi.org/10.1051/0004-6361/201730844)
- Takaro, T., Foley, R. J., McCully, C., et al. 2019, *arXiv:1901.05461*
- Taubenberger, S., Benetti, S., Childress, M., et al. 2011, *MNRAS*, 412, 2735, doi: [10.1111/j.1365-2966.2010.18107.x](https://doi.org/10.1111/j.1365-2966.2010.18107.x)
- Thielemann, F.-K., Nomoto, K., & Hashimoto, M.-A. 1996, *ApJ*, 460, 408, doi: [10.1086/176980](https://doi.org/10.1086/176980)
- Tinyanont, S., Millar-Blanchaer, M., Kasliwal, M., et al. 2021, *arXiv e-prints*, arXiv:2102.02075, <https://arxiv.org/abs/2102.02075>
- Tonry, J. L., Stubbs, C. W., Lykke, K. R., et al. 2012, *ApJ*, 750, 99, doi: [10.1088/0004-637X/750/2/99](https://doi.org/10.1088/0004-637X/750/2/99)
- Tully, R. B., Courtois, H. M., & Sorce, J. G. 2016, *AJ*, 152, 50, doi: [10.3847/0004-6256/152/2/50](https://doi.org/10.3847/0004-6256/152/2/50)
- Tully, R. B., Shaya, E. J., Karachentsev, I. D., et al. 2008, *ApJ*, 676, 184, doi: [10.1086/527428](https://doi.org/10.1086/527428)
- Ugliano, M., Janka, H.-T., Marek, A., & Arcones, A. 2012, *ApJ*, 757, 69, doi: [10.1088/0004-637X/757/1/69](https://doi.org/10.1088/0004-637X/757/1/69)
- Urata, Y., Huang, K., Yamazaki, R., & Sakamoto, T. 2015, *ApJ*, 806, 222, doi: [10.1088/0004-637X/806/2/222](https://doi.org/10.1088/0004-637X/806/2/222)
- Valenti, S., Benetti, S., Cappellaro, E., et al. 2008, *MNRAS*, 383, 1485, doi: [10.1111/j.1365-2966.2007.12647.x](https://doi.org/10.1111/j.1365-2966.2007.12647.x)
- van de Voort, F., Pakmor, R., Grand, R. J. J., et al. 2020, *MNRAS*, 494, 4867, doi: [10.1093/mnras/staa754](https://doi.org/10.1093/mnras/staa754)
- Van Dyk, S. D., Zheng, W., Fox, O. D., et al. 2014, *AJ*, 147, 37, doi: [10.1088/0004-6256/147/2/37](https://doi.org/10.1088/0004-6256/147/2/37)
- Van Dyk, S. D., Zheng, W., Brink, T. G., et al. 2018, *ApJ*, 860, 90, doi: [10.3847/1538-4357/aac32c](https://doi.org/10.3847/1538-4357/aac32c)
- Walt, S. v. d., Colbert, S. C., & Varoquaux, G. 2011, *Computing in Science & Engineering*, 13, 22
- Waxman, E., & Katz, B. 2017, *Shock Breakout Theory*, ed. A. W. Alsabti & P. Murdin, 967, doi: [10.1007/978-3-319-21846-5_33](https://doi.org/10.1007/978-3-319-21846-5_33)
- West, R. M., Lauberts, A., Jorgensen, H. E., & Schuster, H. E. 1987, *A&A*, 177, L1
- Williams, B. F., Hillis, T. J., Murphy, J. W., et al. 2018, *ApJ*, 860, 39, doi: [10.3847/1538-4357/aaba7d](https://doi.org/10.3847/1538-4357/aaba7d)
- Williamson, M., Kerzendorf, W., & Modjaz, M. 2021, *ApJ*, 908, 150, doi: [10.3847/1538-4357/abd244](https://doi.org/10.3847/1538-4357/abd244)
- Woosley, S. E., & Bloom, J. S. 2006, *ARA&A*, 44, 507, doi: [10.1146/annurev.astro.43.072103.150558](https://doi.org/10.1146/annurev.astro.43.072103.150558)
- Xiang, D., Wang, X., Mo, J., et al. 2019, *ApJ*, 871, 176, doi: [10.3847/1538-4357/aaf8b0](https://doi.org/10.3847/1538-4357/aaf8b0)
- Yoon, S.-C. 2015, *PASA*, 32, e015, doi: [10.1017/pasa.2015.16](https://doi.org/10.1017/pasa.2015.16)
- . 2017, *MNRAS*, 470, 3970, doi: [10.1093/mnras/stx1496](https://doi.org/10.1093/mnras/stx1496)
- Yoon, S. C., Woosley, S. E., & Langer, N. 2010, *ApJ*, 725, 940, doi: [10.1088/0004-637X/725/1/940](https://doi.org/10.1088/0004-637X/725/1/940)
- Zapartas, E., de Mink, S. E., Van Dyk, S. D., et al. 2017, *ApJ*, 842, 125, doi: [10.3847/1538-4357/aa7467](https://doi.org/10.3847/1538-4357/aa7467)
- Zenati, Y. 2021, in prep.
- Zenati, Y., Siegel, D. M., Metzger, B. D., & Perets, H. B. 2020, *MNRAS*, 499, 4097, doi: [10.1093/mnras/staa3002](https://doi.org/10.1093/mnras/staa3002)

APPENDIX

Table 7. Optical and UV Photometry of SN 2020oi

MJD	Phase	Band	Mag.	Uncertainty	Telescope	MJD	Phase	Band	Mag.	Uncertainty	Telescope
58856.46	+2.46	UVW2	>13.95	–	<i>Swift</i>	58868.27	+14.27	<i>u</i>	15.29	0.08	LCO
58856.79	+2.79	UVW2	>13.92	–	<i>Swift</i>	58869.27	+15.27	<i>u</i>	15.54	0.07	LCO
58857.45	+3.45	UVW2	>14.17	–	<i>Swift</i>	58870.27	+16.27	<i>u</i>	15.93	0.10	LCO
58858.85	+4.85	UVW2	>13.95	–	<i>Swift</i>	58871.26	+17.26	<i>u</i>	16.16	0.17	LCO
58859.49	+5.49	UVW2	>13.93	–	<i>Swift</i>	58872.29	+18.29	<i>u</i>	16.49	0.07	LCO
58860.38	+6.38	UVW2	>13.96	–	<i>Swift</i>	58872.35	+18.35	<i>u</i>	16.11	0.03	Swope
58861.25	+7.25	UVW2	>13.83	–	<i>Swift</i>	58873.09	+19.09	<i>u</i>	16.73	0.06	LCO
58877.19	+23.19	UVW2	>13.93	–	<i>Swift</i>	58874.28	+20.28	<i>u</i>	16.86	0.08	LCO
58887.68	+33.68	UVW2	>13.98	–	<i>Swift</i>	58875.25	+21.25	<i>u</i>	17.04	0.07	LCO
58898.57	+44.57	UVW2	>14.02	–	<i>Swift</i>	58876.33	+22.33	<i>u</i>	17.01	0.61	LCO
58907.25	+53.25	UVW2	>14.01	–	<i>Swift</i>	58876.33	+22.33	<i>u</i>	>14.02	–	LCO
58856.46	+2.46	UVM2	>13.75	–	<i>Swift</i>	58876.37	+22.37	<i>u</i>	17.46	0.04	Swope
58857.46	+3.46	UVM2	>13.86	–	<i>Swift</i>	58878.34	+24.34	<i>u</i>	17.14	0.19	LCO
58858.86	+4.86	UVM2	>13.75	–	<i>Swift</i>	58881.99	+27.99	<i>u</i>	17.10	0.10	LCO
58860.38	+6.38	UVM2	>13.81	–	<i>Swift</i>	58882.32	+28.32	<i>u</i>	17.99	0.05	Swope
58861.25	+7.25	UVM2	>13.74	–	<i>Swift</i>	58884.37	+30.37	<i>u</i>	17.32	0.16	LCO
58877.19	+23.19	UVM2	>13.73	–	<i>Swift</i>	58884.37	+30.37	<i>u</i>	>15.72	–	LCO
58887.68	+33.68	UVM2	>13.79	–	<i>Swift</i>	58885.36	+31.36	<i>u</i>	18.12	0.08	Swope
58898.57	+44.57	UVM2	>13.92	–	<i>Swift</i>	58893.29	+39.29	<i>u</i>	16.54	0.03	Swope
58907.25	+53.25	UVM2	>13.76	–	<i>Swift</i>	58895.29	+41.29	<i>u</i>	18.55	0.09	Swope
58856.45	+2.45	UVW1	>14.08	–	<i>Swift</i>	58895.29	+41.29	<i>u</i>	>15.44	–	LCO
58856.79	+2.79	UVW1	>14.04	–	<i>Swift</i>	58896.29	+42.29	<i>u</i>	18.37	0.11	Swope
58857.45	+3.45	UVW1	>14.22	–	<i>Swift</i>	58897.32	+43.32	<i>u</i>	17.42	0.04	Swope
58858.84	+4.84	UVW1	>14.03	–	<i>Swift</i>	58902.24	+48.24	<i>u</i>	>14.81	–	LCO
58859.48	+5.48	UVW1	>14.04	–	<i>Swift</i>	58903.28	+49.28	<i>u</i>	18.55	0.10	Swope
58859.81	+5.81	UVW1	>13.99	–	<i>Swift</i>	58904.33	+50.33	<i>u</i>	18.60	0.07	Swope
58859.97	+5.97	UVW1	>13.99	–	<i>Swift</i>	58905.29	+51.29	<i>u</i>	18.65	0.07	Swope
58860.38	+6.38	UVW1	>14.03	–	<i>Swift</i>	58906.10	+52.10	<i>u</i>	>15.62	–	LCO
58861.24	+7.24	UVW1	>13.80	–	<i>Swift</i>	58906.28	+52.28	<i>u</i>	18.77	0.08	Swope
58877.19	+23.19	UVW1	>14.06	–	<i>Swift</i>	58907.37	+53.37	<i>u</i>	18.38	0.08	Swope
58887.68	+33.68	UVW1	>14.27	–	<i>Swift</i>	58908.31	+54.31	<i>u</i>	18.65	0.10	Swope
58898.57	+44.57	UVW1	>14.20	–	<i>Swift</i>	58909.36	+55.36	<i>u</i>	18.59	0.07	Swope
58907.25	+53.25	UVW1	>14.22	–	<i>Swift</i>	58910.16	+56.16	<i>u</i>	>15.77	–	LCO
58856.39	+2.39	<i>u</i>	15.37	0.06	LCO	58910.25	+56.25	<i>u</i>	18.59	0.10	Swope
58857.30	+3.30	<i>u</i>	15.41	0.09	LCO	58911.20	+57.20	<i>u</i>	18.55	0.09	Swope
58857.30	+3.30	<i>u</i>	15.41	0.09	LCO	58912.27	+58.27	<i>u</i>	18.80	0.11	Swope
58857.32	+3.32	<i>u</i>	15.60	0.07	LCO	58919.14	+65.14	<i>u</i>	>15.81	–	LCO
58858.30	+4.30	<i>u</i>	15.43	0.06	LCO	58921.25	+67.25	<i>u</i>	17.44	0.07	Swope
58859.05	+5.05	<i>u</i>	15.10	0.04	LCO	58923.14	+69.14	<i>u</i>	>16.00	–	LCO
58860.05	+6.05	<i>u</i>	14.66	0.04	LCO	58929.50	+75.50	<i>u</i>	16.94	0.10	LCO
58861.05	+7.05	<i>u</i>	14.10	0.04	LCO	58929.50	+75.50	<i>u</i>	>16.29	–	LCO
58861.05	+7.05	<i>u</i>	>14.72	–	LCO	58935.62	+81.62	<i>u</i>	>14.88	–	LCO
58861.05	+7.05	<i>u</i>	14.22	0.04	LCO	58935.62	+81.62	<i>u</i>	14.88	0.36	LCO
58864.75	+10.75	<i>u</i>	14.20	0.04	LCO	58935.64	+81.64	<i>u</i>	15.00	0.36	LCO
58866.30	+12.30	<i>u</i>	14.52	0.04	LCO	58935.64	+81.64	<i>u</i>	>15.00	–	LCO
58867.30	+13.30	<i>u</i>	14.98	0.04	LCO	58943.46	+89.46	<i>u</i>	14.67	0.36	LCO

MJD	Phase	Band	Mag.	Uncertainty	Telescope	MJD	Phase	Band	Mag.	Uncertainty	Telescope
58943.46	+89.46	<i>u</i>	>14.67	–	LCO	58859.49	+5.49	<i>B</i>	>14.44	–	<i>Swift</i>
58952.44	+98.44	<i>u</i>	>16.07	–	LCO	58860.38	+6.38	<i>B</i>	>14.25	–	<i>Swift</i>
58966.35	+112.35	<i>u</i>	>16.32	–	LCO	58861.25	+7.25	<i>B</i>	>13.99	–	<i>Swift</i>
58974.11	+120.11	<i>u</i>	>15.64	–	LCO	58864.60	+10.60	<i>B</i>	14.30	0.37	Synthetic
58980.76	+126.76	<i>u</i>	>16.87	–	LCO	58868.60	+14.60	<i>B</i>	14.63	0.38	Synthetic
58988.31	+134.31	<i>u</i>	>16.04	–	LCO	58869.35	+15.35	<i>B</i>	14.58	0.03	Swope
58996.50	+142.50	<i>u</i>	>16.69	–	LCO	58869.35	+15.35	<i>B</i>	14.73	0.03	Swope
59002.74	+148.74	<i>u</i>	>18.18	–	LCO	58870.32	+16.32	<i>B</i>	14.88	0.03	Swope
59007.70	+153.70	<i>u</i>	>18.79	–	LCO	58870.50	+16.50	<i>B</i>	15.02	0.39	Synthetic
59014.79	+160.79	<i>u</i>	>19.02	–	LCO	58871.36	+17.36	<i>B</i>	15.13	0.03	Swope
59026.34	+172.34	<i>u</i>	>17.91	–	LCO	58872.36	+18.36	<i>B</i>	15.30	0.03	Swope
59032.34	+178.34	<i>u</i>	>19.29	–	LCO	58872.40	+18.40	<i>B</i>	15.14	0.39	Synthetic
59202.09	+348.09	<i>u</i>	>17.83	–	LCO	58873.09	+19.09	<i>B</i>	>18.09	–	LCO
59208.07	+354.07	<i>u</i>	>17.84	–	LCO	58875.00	+21.00	<i>B</i>	15.22	0.39	Synthetic
59213.45	+359.45	<i>u</i>	>16.58	–	LCO	58875.38	+21.38	<i>B</i>	15.82	0.03	Swope
59214.05	+360.05	<i>u</i>	>16.73	–	LCO	58876.37	+22.37	<i>B</i>	15.94	0.03	Swope
59220.37	+366.37	<i>u</i>	>17.40	–	LCO	58876.70	+22.70	<i>B</i>	16.10	0.42	Synthetic
59226.10	+372.10	<i>u</i>	>17.77	–	LCO	58878.06	+24.06	<i>B</i>	>16.25	–	LCO
59227.71	+373.71	<i>u</i>	>17.74	–	LCO	58879.07	+25.07	<i>B</i>	>15.93	–	LCO
59232.37	+378.37	<i>u</i>	>17.12	–	LCO	58880.30	+26.30	<i>B</i>	16.10	0.42	Synthetic
59236.06	+382.06	<i>u</i>	>17.29	–	LCO	58880.40	+26.40	<i>B</i>	15.36	0.40	Synthetic
59245.42	+391.42	<i>u</i>	>17.76	–	LCO	58880.44	+26.44	<i>B</i>	>18.29	–	Nickel
59252.05	+398.05	<i>u</i>	>18.17	–	LCO	58882.33	+28.33	<i>B</i>	16.50	0.03	Swope
59257.33	+403.33	<i>u</i>	>17.73	–	LCO	58883.01	+29.01	<i>B</i>	>17.54	–	LCO
59262.22	+408.22	<i>u</i>	>17.55	–	LCO	58883.38	+29.38	<i>B</i>	16.55	0.03	Swope
59267.12	+413.12	<i>u</i>	>16.91	–	LCO	58884.38	+30.38	<i>B</i>	16.54	0.03	Swope
58856.45	+2.45	<i>U</i>	>14.00	–	<i>Swift</i>	58885.37	+31.37	<i>B</i>	16.62	0.03	Swope
58856.79	+2.79	<i>U</i>	>14.00	–	<i>Swift</i>	58887.69	+33.69	<i>B</i>	>14.70	–	<i>Swift</i>
58857.45	+3.45	<i>U</i>	>14.13	–	<i>Swift</i>	58892.00	+38.00	<i>B</i>	17.60	0.45	Synthetic
58858.85	+4.85	<i>U</i>	>13.96	–	<i>Swift</i>	58893.30	+39.30	<i>B</i>	16.90	0.03	Swope
58859.49	+5.49	<i>U</i>	>13.84	–	<i>Swift</i>	58894.32	+40.32	<i>B</i>	16.46	0.06	Swope
58860.38	+6.38	<i>U</i>	>13.61	–	<i>Swift</i>	58895.00	+41.00	<i>B</i>	16.98	0.44	Synthetic
58861.25	+7.25	<i>U</i>	>13.35	–	<i>Swift</i>	58895.43	+41.43	<i>B</i>	>18.60	–	Nickel
58877.19	+23.19	<i>U</i>	>14.31	–	<i>Swift</i>	58897.33	+43.33	<i>B</i>	16.34	0.03	Swope
58887.68	+33.68	<i>U</i>	>14.46	–	<i>Swift</i>	58898.57	+44.57	<i>B</i>	>14.70	–	<i>Swift</i>
58887.69	+33.69	<i>U</i>	>14.32	–	<i>Swift</i>	58903.29	+49.29	<i>B</i>	16.89	0.03	Swope
58898.56	+44.56	<i>U</i>	>14.68	–	<i>Swift</i>	58904.34	+50.34	<i>B</i>	17.05	0.03	Swope
58898.57	+44.57	<i>U</i>	>14.33	–	<i>Swift</i>	58905.31	+51.31	<i>B</i>	17.03	0.03	Swope
58907.25	+53.25	<i>U</i>	>14.49	–	<i>Swift</i>	58906.29	+52.29	<i>B</i>	17.08	0.03	Swope
58907.26	+53.26	<i>U</i>	>14.36	–	<i>Swift</i>	58906.30	+52.30	<i>B</i>	17.07	0.03	Swope
58856.45	+2.45	<i>B</i>	>14.75	–	<i>Swift</i>	58907.26	+53.26	<i>B</i>	>14.75	–	<i>Swift</i>
58856.79	+2.79	<i>B</i>	>14.81	–	<i>Swift</i>	58907.38	+53.38	<i>B</i>	17.02	0.03	Swope
58857.30	+3.30	<i>B</i>	15.66	0.41	Synthetic	58908.32	+54.32	<i>B</i>	17.02	0.03	Swope
58857.45	+3.45	<i>B</i>	>14.79	–	<i>Swift</i>	58908.33	+54.33	<i>B</i>	17.05	0.03	Swope
58858.85	+4.85	<i>B</i>	>14.52	–	<i>Swift</i>	58909.37	+55.37	<i>B</i>	17.11	0.03	Swope

MJD	Phase	Band	Mag.	Uncertainty	Telescope	MJD	Phase	Band	Mag.	Uncertainty	Telescope
58910.26	+56.26	<i>B</i>	17.03	0.03	Swope	58859.30	+5.30	<i>g</i>	14.52	0.03	LCO
58911.21	+57.21	<i>B</i>	17.12	0.03	Swope	58859.52	+5.52	<i>g</i>	14.39	0.03	ZTF
58912.28	+58.28	<i>B</i>	17.13	0.03	Swope	58859.69	+5.69	<i>g</i>	14.39	0.03	LCO
58921.26	+67.26	<i>B</i>	16.80	0.10	Swope	58860.05	+6.05	<i>g</i>	14.65	0.07	LCO
58923.29	+69.29	<i>B</i>	16.71	0.04	Swope	58860.05	+6.05	<i>g</i>	>16.55	–	LCO
58954.16	+100.16	<i>B</i>	>18.31	–	Nickel	58860.05	+6.05	<i>g</i>	14.23	0.03	LCO
58963.19	+109.19	<i>B</i>	>17.82	–	Nickel	58860.07	+6.07	<i>g</i>	14.15	0.03	LCO
58995.60	+141.60	<i>B</i>	16.79	0.45	Synthetic	58860.07	+6.07	<i>g</i>	14.16	0.03	LCO
58543.30	-310.70	<i>g</i>	18.19	0.15	ZTF	58861.05	+7.05	<i>g</i>	13.88	0.03	LCO
58559.31	-294.69	<i>g</i>	19.87	0.35	ZTF	58861.29	+7.29	<i>g</i>	13.96	0.03	LCO
58559.32	-294.68	<i>g</i>	19.83	0.34	ZTF	58861.35	+7.35	<i>g</i>	13.83	0.03	LCO
58575.29	-278.71	<i>g</i>	19.42	0.20	ZTF	58861.35	+7.35	<i>g</i>	13.85	0.03	LCO
58575.29	-278.71	<i>g</i>	18.79	0.19	ZTF	58861.68	+7.68	<i>g</i>	13.78	0.03	LCO
58580.26	-273.74	<i>g</i>	20.02	0.23	ZTF	58862.36	+8.36	<i>g</i>	13.65	0.03	LCO
58586.26	-267.74	<i>g</i>	20.03	0.27	ZTF	58862.36	+8.36	<i>g</i>	13.66	0.03	LCO
58596.23	-257.77	<i>g</i>	19.91	0.24	ZTF	58862.53	+8.53	<i>g</i>	13.58	0.04	Thacher
58596.23	-257.77	<i>g</i>	20.13	0.32	ZTF	58863.53	+9.53	<i>g</i>	12.57	0.03	Thacher
58600.21	-253.79	<i>g</i>	20.42	0.36	ZTF	58864.34	+10.34	<i>g</i>	13.51	0.04	Thacher
58600.21	-253.79	<i>g</i>	20.09	0.28	ZTF	58864.60	+10.60	<i>g</i>	14.10	0.37	Synthetic
58628.19	-225.81	<i>g</i>	20.13	0.27	ZTF	58864.75	+10.75	<i>g</i>	13.57	0.03	LCO
58635.19	-218.81	<i>g</i>	19.74	0.17	ZTF	58865.45	+11.45	<i>g</i>	13.57	0.03	Thacher
58636.25	-217.75	<i>g</i>	19.47	0.17	ZTF	58866.30	+12.30	<i>g</i>	13.60	0.03	LCO
58639.23	-214.77	<i>g</i>	20.26	0.29	ZTF	58866.32	+12.32	<i>g</i>	13.62	0.03	Thacher
58642.20	-211.80	<i>g</i>	20.24	0.32	ZTF	58866.57	+12.57	<i>g</i>	13.62	0.03	PS1
58846.55	-7.45	<i>g</i>	19.60	0.18	ZTF	58867.30	+13.30	<i>g</i>	13.73	0.03	LCO
58849.50	-4.50	<i>g</i>	20.45	0.36	ZTF	58867.30	+13.30	<i>g</i>	13.73	0.03	LCO
58856.31	+2.31	<i>g</i>	15.81	0.04	LCO	58867.30	+13.30	<i>g</i>	13.82	0.03	LCO
58856.33	+2.33	<i>g</i>	15.78	0.03	LCO	58867.35	+13.35	<i>g</i>	13.72	0.03	Thacher
58856.33	+2.33	<i>g</i>	15.79	0.03	LCO	58867.40	+13.40	<i>g</i>	13.77	0.03	LCO
58856.35	+2.35	<i>g</i>	15.83	0.03	LCO	58867.40	+13.40	<i>g</i>	13.79	0.03	LCO
58856.37	+2.37	<i>g</i>	15.82	0.04	LCO	58867.44	+13.44	<i>g</i>	13.87	0.03	ZTF
58856.41	+2.41	<i>g</i>	15.54	0.03	LCO	58868.27	+14.27	<i>g</i>	13.96	0.03	LCO
58856.73	+2.73	<i>g</i>	15.54	0.03	LCO	58868.60	+14.60	<i>g</i>	14.37	0.37	Synthetic
58856.73	+2.73	<i>g</i>	15.56	0.03	LCO	58869.27	+15.27	<i>g</i>	14.11	0.03	LCO
58857.30	+3.30	<i>g</i>	15.53	0.40	Synthetic	58869.35	+15.35	<i>g</i>	14.18	0.03	Swope
58857.30	+3.30	<i>g</i>	15.32	0.03	LCO	58869.36	+15.36	<i>g</i>	14.11	0.03	LCO
58857.32	+3.32	<i>g</i>	15.34	0.03	LCO	58869.36	+15.36	<i>g</i>	14.10	0.03	LCO
58857.35	+3.35	<i>g</i>	15.38	0.03	LCO	58869.57	+15.57	<i>g</i>	14.10	0.03	PS1
58857.36	+3.36	<i>g</i>	15.21	0.12	LCO	58870.27	+16.27	<i>g</i>	14.39	0.03	LCO
58857.71	+3.71	<i>g</i>	15.21	0.03	LCO	58870.50	+16.50	<i>g</i>	14.70	0.38	Synthetic
58857.72	+3.72	<i>g</i>	15.17	0.03	LCO	58871.27	+17.27	<i>g</i>	14.62	0.03	LCO
58858.30	+4.30	<i>g</i>	14.94	0.03	LCO	58871.32	+17.32	<i>g</i>	14.52	0.03	LCO
58858.30	+4.30	<i>g</i>	14.86	0.03	LCO	58871.32	+17.32	<i>g</i>	14.53	0.03	LCO
58858.31	+4.31	<i>g</i>	14.92	0.03	LCO	58871.33	+17.33	<i>g</i>	14.42	0.03	Thacher
58858.34	+4.34	<i>g</i>	14.88	0.03	LCO	58871.35	+17.35	<i>g</i>	14.52	0.03	Swope
58859.05	+5.05	<i>g</i>	14.63	0.03	LCO	58871.44	+17.44	<i>g</i>	14.59	0.03	ZTF

MJD	Phase	Band	Mag.	Uncertainty	Telescope
58872.29	+18.29	<i>g</i>	14.68	0.03	LCO
58872.33	+18.33	<i>g</i>	14.60	0.03	Thacher
58872.35	+18.35	<i>g</i>	14.73	0.03	Swope
58872.35	+18.35	<i>g</i>	14.61	0.03	Swope
58872.40	+18.40	<i>g</i>	14.85	0.38	Synthetic
58873.09	+19.09	<i>g</i>	14.76	0.03	LCO
58873.09	+19.09	<i>g</i>	14.75	0.03	LCO
58873.09	+19.09	<i>g</i>	14.80	0.03	LCO
58873.40	+19.40	<i>g</i>	14.84	0.03	Thacher
58874.28	+20.28	<i>g</i>	14.97	0.03	LCO
58874.29	+20.29	<i>g</i>	14.94	0.03	Thacher
58875.00	+21.00	<i>g</i>	15.02	0.39	Synthetic
58875.25	+21.25	<i>g</i>	15.20	0.03	LCO
58875.38	+21.38	<i>g</i>	15.18	0.03	Swope
58875.46	+21.46	<i>g</i>	15.25	0.03	ZTF
58876.03	+22.03	<i>g</i>	15.23	0.03	LCO
58876.03	+22.03	<i>g</i>	15.21	0.03	LCO
58876.29	+22.29	<i>g</i>	15.16	0.05	Thacher
58876.33	+22.33	<i>g</i>	15.36	0.05	LCO
58876.36	+22.36	<i>g</i>	15.30	0.03	Swope
58876.70	+22.70	<i>g</i>	15.65	0.40	Synthetic
58877.03	+23.03	<i>g</i>	15.35	0.03	LCO
58877.03	+23.03	<i>g</i>	15.37	0.03	LCO
58877.26	+23.26	<i>g</i>	15.44	0.03	LCO
58877.26	+23.26	<i>g</i>	15.40	0.04	LCO
58878.06	+24.06	<i>g</i>	>16.42	–	LCO
58878.34	+24.34	<i>g</i>	15.55	0.03	LCO
58878.49	+24.49	<i>g</i>	15.62	0.03	ZTF
58879.08	+25.08	<i>g</i>	>16.75	–	LCO
58879.40	+25.40	<i>g</i>	14.97	0.39	Synthetic
58880.12	+26.12	<i>g</i>	15.62	0.03	LCO
58880.12	+26.12	<i>g</i>	15.59	0.03	LCO
58880.28	+26.28	<i>g</i>	15.67	0.04	Thacher
58880.30	+26.30	<i>g</i>	15.86	0.41	Synthetic
58880.40	+26.40	<i>g</i>	15.25	0.39	Synthetic
58881.28	+27.28	<i>g</i>	15.75	0.04	Thacher
58881.46	+27.46	<i>g</i>	15.84	0.03	ZTF
58881.99	+27.99	<i>g</i>	15.78	0.03	LCO
58882.09	+28.09	<i>g</i>	15.80	0.03	LCO
58882.09	+28.09	<i>g</i>	15.85	0.03	LCO
58882.32	+28.32	<i>g</i>	15.92	0.03	Swope
58883.01	+29.01	<i>g</i>	15.90	0.04	LCO
58883.01	+29.01	<i>g</i>	15.91	0.04	LCO
58883.01	+29.01	<i>g</i>	>17.66	–	LCO
58883.12	+29.12	<i>g</i>	15.84	0.03	LCO
58883.12	+29.12	<i>g</i>	15.87	0.03	LCO

MJD	Phase	Band	Mag.	Uncertainty	Telescope
58883.38	+29.38	<i>g</i>	16.00	0.03	Swope
58883.99	+29.99	<i>g</i>	15.91	0.03	LCO
58884.00	+30.00	<i>g</i>	16.01	0.04	LCO
58884.37	+30.37	<i>g</i>	16.00	0.03	LCO
58884.37	+30.37	<i>g</i>	15.84	0.30	LCO
58884.37	+30.37	<i>g</i>	16.01	0.03	Swope
58884.37	+30.37	<i>g</i>	>17.25	–	LCO
58884.44	+30.44	<i>g</i>	16.07	0.03	ZTF
58885.36	+31.36	<i>g</i>	16.08	0.03	Swope
58885.37	+31.37	<i>g</i>	15.99	0.04	Thacher
58885.38	+31.38	<i>g</i>	>15.89	–	Swope
58886.28	+32.28	<i>g</i>	16.08	0.07	Thacher
58887.43	+33.43	<i>g</i>	16.11	0.03	ZTF
58890.28	+36.28	<i>g</i>	15.78	0.22	Thacher
58892.00	+38.00	<i>g</i>	17.06	0.44	Synthetic
58892.26	+38.26	<i>g</i>	16.21	0.05	Thacher
58892.38	+38.38	<i>g</i>	16.28	0.03	ZTF
58893.25	+39.25	<i>g</i>	16.16	0.03	Thacher
58893.29	+39.29	<i>g</i>	16.33	0.03	Swope
58894.25	+40.25	<i>g</i>	16.28	0.04	Thacher
58894.31	+40.31	<i>g</i>	16.34	0.03	Swope
58895.00	+41.00	<i>g</i>	16.69	0.43	Synthetic
58895.29	+41.29	<i>g</i>	>16.56	–	LCO
58895.29	+41.29	<i>g</i>	16.37	0.03	Swope
58895.38	+41.38	<i>g</i>	16.34	0.03	ZTF
58896.29	+42.29	<i>g</i>	16.38	0.04	Swope
58897.31	+43.31	<i>g</i>	16.06	0.03	Swope
58898.24	+44.24	<i>g</i>	16.44	0.04	Thacher
58898.42	+44.42	<i>g</i>	16.42	0.03	ZTF
58899.23	+45.23	<i>g</i>	16.44	0.05	Thacher
58899.40	+45.40	<i>g</i>	16.44	0.03	ZTF
58900.34	+46.34	<i>g</i>	16.48	0.05	Thacher
58902.24	+48.24	<i>g</i>	>16.54	–	LCO
58903.27	+49.27	<i>g</i>	16.51	0.03	Swope
58903.29	+49.29	<i>g</i>	16.33	0.04	Thacher
58903.36	+49.36	<i>g</i>	16.47	0.03	ZTF
58904.32	+50.32	<i>g</i>	16.52	0.03	Swope
58904.46	+50.46	<i>g</i>	16.54	0.03	ZTF
58905.29	+51.29	<i>g</i>	16.55	0.03	Swope
58905.31	+51.31	<i>g</i>	16.55	0.03	ZTF
58905.57	+51.57	<i>g</i>	15.93	0.11	Thacher
58906.28	+52.28	<i>g</i>	16.56	0.03	Swope
58906.33	+52.33	<i>g</i>	16.50	0.03	ZTF
58907.36	+53.36	<i>g</i>	16.58	0.03	Swope
58908.31	+54.31	<i>g</i>	16.57	0.03	Swope
58908.31	+54.31	<i>g</i>	16.59	0.03	Swope

MJD	Phase	Band	Mag.	Uncertainty	Telescope	MJD	Phase	Band	Mag.	Uncertainty	Telescope
58908.34	+54.34	<i>g</i>	16.55	0.03	ZTF	59007.71	+153.71	<i>g</i>	>18.14	–	LCO
58909.36	+55.36	<i>g</i>	16.66	0.03	Swope	59014.20	+160.20	<i>g</i>	20.23	0.28	ZTF
58910.25	+56.25	<i>g</i>	16.67	0.03	Swope	59014.80	+160.80	<i>g</i>	>18.73	–	LCO
58911.20	+57.20	<i>g</i>	16.67	0.03	Swope	59020.20	+166.20	<i>g</i>	19.92	0.22	ZTF
58911.40	+57.40	<i>g</i>	16.73	0.03	ZTF	59023.22	+169.22	<i>g</i>	20.15	0.31	ZTF
58912.27	+58.27	<i>g</i>	16.68	0.03	Swope	59026.22	+172.22	<i>g</i>	19.02	0.18	ZTF
58913.33	+59.33	<i>g</i>	16.62	0.03	ZTF	59026.35	+172.35	<i>g</i>	>16.83	–	LCO
58914.42	+60.42	<i>g</i>	16.76	0.04	ZTF	59032.34	+178.34	<i>g</i>	>19.87	–	LCO
58915.44	+61.44	<i>g</i>	16.70	0.04	ZTF	59038.72	+184.72	<i>g</i>	>19.25	–	LCO
58919.14	+65.14	<i>g</i>	16.05	0.04	LCO	59173.49	+319.49	<i>g</i>	20.16	0.34	ZTF
58919.14	+65.14	<i>g</i>	>16.37	–	LCO	59177.53	+323.53	<i>g</i>	19.46	0.17	ZTF
58923.14	+69.14	<i>g</i>	>17.07	–	LCO	59186.52	+332.52	<i>g</i>	18.81	0.23	ZTF
58929.50	+75.50	<i>g</i>	15.88	0.06	LCO	59193.46	+339.46	<i>g</i>	20.02	0.30	ZTF
58929.50	+75.50	<i>g</i>	>17.04	–	LCO	59202.09	+348.09	<i>g</i>	>18.12	–	LCO
58935.64	+81.64	<i>g</i>	16.72	0.36	LCO	59203.53	+349.53	<i>g</i>	19.34	0.17	ZTF
58935.64	+81.64	<i>g</i>	>16.72	–	LCO	59208.07	+354.07	<i>g</i>	>17.92	–	LCO
58936.29	+82.29	<i>g</i>	17.21	0.04	ZTF	59214.05	+360.05	<i>g</i>	>17.34	–	LCO
58939.34	+85.34	<i>g</i>	17.34	0.04	ZTF	59217.44	+363.44	<i>g</i>	19.46	0.24	ZTF
58940.39	+86.39	<i>g</i>	17.32	0.04	ZTF	59220.37	+366.37	<i>g</i>	>17.94	–	LCO
58941.46	+87.46	<i>g</i>	17.38	0.05	ZTF	59221.48	+367.48	<i>g</i>	19.45	0.18	ZTF
58943.46	+89.46	<i>g</i>	>16.66	–	LCO	59226.11	+372.11	<i>g</i>	>17.17	–	LCO
58943.46	+89.46	<i>g</i>	16.66	0.36	LCO	59227.71	+373.71	<i>g</i>	>18.33	–	LCO
58952.44	+98.44	<i>g</i>	>17.71	–	LCO	59232.37	+378.37	<i>g</i>	>16.88	–	LCO
58954.30	+100.30	<i>g</i>	17.82	0.04	ZTF	59236.06	+382.06	<i>g</i>	>17.68	–	LCO
58955.30	+101.30	<i>g</i>	17.83	0.05	ZTF	59245.42	+391.42	<i>g</i>	>18.21	–	LCO
58959.34	+105.34	<i>g</i>	>17.38	–	LCO	59250.36	+396.36	<i>g</i>	20.10	0.36	ZTF
58962.23	+108.23	<i>g</i>	17.95	0.05	ZTF	59252.06	+398.06	<i>g</i>	>17.65	–	LCO
58963.31	+109.31	<i>g</i>	18.13	0.05	ZTF	59252.49	+398.49	<i>g</i>	20.10	0.25	ZTF
58965.23	+111.23	<i>g</i>	17.99	0.05	ZTF	59257.33	+403.33	<i>g</i>	>18.74	–	LCO
58966.35	+112.35	<i>g</i>	>16.33	–	LCO	59262.22	+408.22	<i>g</i>	>17.90	–	LCO
58967.23	+113.23	<i>g</i>	18.12	0.06	ZTF	59267.12	+413.12	<i>g</i>	>16.98	–	LCO
58968.30	+114.30	<i>g</i>	18.33	0.06	ZTF	58856.46	+2.46	<i>V</i>	>14.17	–	<i>Swift</i>
58971.28	+117.28	<i>g</i>	18.18	0.07	ZTF	58856.80	+2.80	<i>V</i>	>14.17	–	<i>Swift</i>
58974.11	+120.11	<i>g</i>	>16.69	–	LCO	58857.30	+3.30	<i>V</i>	15.29	0.40	Synthetic
58974.21	+120.21	<i>g</i>	18.37	0.11	ZTF	58857.45	+3.45	<i>V</i>	>14.05	–	<i>Swift</i>
58977.17	+123.17	<i>g</i>	19.41	0.33	ZTF	58858.85	+4.85	<i>V</i>	>13.85	–	<i>Swift</i>
58980.19	+126.19	<i>g</i>	18.79	0.07	ZTF	58860.38	+6.38	<i>V</i>	>13.58	–	<i>Swift</i>
58980.76	+126.76	<i>g</i>	>16.81	–	LCO	58861.25	+7.25	<i>V</i>	>13.40	–	<i>Swift</i>
58986.22	+132.22	<i>g</i>	19.08	0.10	ZTF	58864.60	+10.60	<i>V</i>	13.57	0.35	Synthetic
58988.32	+134.32	<i>g</i>	>16.91	–	LCO	58868.60	+14.60	<i>V</i>	13.78	0.36	Synthetic
58991.17	+137.17	<i>g</i>	18.97	0.10	ZTF	58869.35	+15.35	<i>V</i>	13.80	0.03	Swope
58994.23	+140.23	<i>g</i>	19.42	0.12	ZTF	58869.36	+15.36	<i>V</i>	13.64	0.03	LCO
58995.60	+141.60	<i>g</i>	16.60	0.43	Synthetic	58870.32	+16.32	<i>V</i>	13.83	0.03	Swope
58996.50	+142.50	<i>g</i>	>17.03	–	LCO	58870.32	+16.32	<i>V</i>	13.90	0.03	Swope
58997.20	+143.20	<i>g</i>	19.14	0.12	ZTF	58870.50	+16.50	<i>V</i>	14.02	0.36	Synthetic
59002.75	+148.75	<i>g</i>	>18.42	–	LCO	58871.31	+17.31	<i>V</i>	13.89	0.03	LCO

MJD	Phase	Band	Mag.	Uncertainty	Telescope
58871.36	+17.36	V	14.12	0.03	Swope
58872.36	+18.36	V	14.30	0.03	Swope
58872.40	+18.40	V	14.31	0.37	Synthetic
58873.09	+19.09	V	>17.53	–	LCO
58875.00	+21.00	V	14.63	0.38	Synthetic
58875.38	+21.38	V	14.69	0.03	Swope
58876.37	+22.37	V	14.92	0.03	Swope
58876.70	+22.70	V	14.97	0.39	Synthetic
58877.19	+23.19	V	>13.84	–	<i>Swift</i>
58878.06	+24.06	V	>15.76	–	LCO
58879.08	+25.08	V	>15.62	–	LCO
58879.40	+25.40	V	14.87	0.38	Synthetic
58880.12	+26.12	V	>16.86	–	LCO
58880.30	+26.30	V	15.31	0.39	Synthetic
58880.40	+26.40	V	15.10	0.39	Synthetic
58880.44	+26.44	V	>17.76	–	Nickel
58882.33	+28.33	V	15.56	0.03	Swope
58883.12	+29.12	V	15.26	0.03	LCO
58883.38	+29.38	V	15.67	0.03	Swope
58884.37	+30.37	V	15.63	0.03	Swope
58885.37	+31.37	V	15.73	0.03	Swope
58887.68	+33.68	V	>13.97	–	<i>Swift</i>
58892.00	+38.00	V	16.32	0.42	Synthetic
58893.30	+39.30	V	16.12	0.03	Swope
58894.32	+40.32	V	16.17	0.03	Swope
58895.00	+41.00	V	16.12	0.41	Synthetic
58895.30	+41.30	V	16.11	0.03	Swope
58895.43	+41.43	V	>18.67	–	Nickel
58895.44	+41.44	V	>18.43	–	Nickel
58896.30	+42.30	V	16.08	0.03	Swope
58897.32	+43.32	V	15.80	0.12	Swope
58898.57	+44.57	V	>14.05	–	<i>Swift</i>
58899.32	+45.32	V	>18.54	–	Nickel
58900.38	+46.38	V	>18.18	–	Nickel
58903.28	+49.28	V	16.27	0.03	Swope
58904.34	+50.34	V	16.40	0.03	Swope
58904.35	+50.35	V	>18.08	–	Nickel
58905.30	+51.30	V	16.41	0.03	Swope
58906.29	+52.29	V	16.43	0.03	Swope
58907.25	+53.25	V	>14.10	–	<i>Swift</i>
58907.37	+53.37	V	16.39	0.03	Swope
58908.32	+54.32	V	16.39	0.03	Swope
58908.32	+54.32	V	16.41	0.03	Swope
58909.37	+55.37	V	16.51	0.03	Swope
58910.26	+56.26	V	16.45	0.03	Swope
58911.21	+57.21	V	16.46	0.03	Swope

MJD	Phase	Band	Mag.	Uncertainty	Telescope
58912.28	+58.28	V	16.58	0.03	Swope
58921.26	+67.26	V	16.50	0.05	Swope
58923.29	+69.29	V	16.34	0.03	Swope
58963.20	+109.20	V	>17.59	–	Nickel
58995.60	+141.60	V	16.32	0.85	Synthetic
58558.22	-295.78	<i>r</i>	18.58	0.18	ZTF
58575.37	-278.63	<i>r</i>	18.63	0.28	ZTF
58580.35	-273.65	<i>r</i>	20.23	0.33	ZTF
58583.28	-270.72	<i>r</i>	19.41	0.22	ZTF
58584.32	-269.68	<i>r</i>	20.14	0.34	ZTF
58588.34	-265.66	<i>r</i>	19.48	0.30	ZTF
58589.27	-264.73	<i>r</i>	18.89	0.29	ZTF
58597.33	-256.67	<i>r</i>	19.87	0.24	ZTF
58633.20	-220.80	<i>r</i>	20.12	0.36	ZTF
58634.26	-219.74	<i>r</i>	20.29	0.28	ZTF
58637.19	-216.81	<i>r</i>	20.25	0.28	ZTF
58638.23	-215.77	<i>r</i>	20.10	0.28	ZTF
58834.52	-19.48	<i>r</i>	18.72	0.20	ZTF
58855.54	+1.54	<i>r</i>	16.96	0.03	ZTF
58856.31	+2.31	<i>r</i>	15.98	0.04	LCO
58856.31	+2.31	<i>r</i>	>16.51	–	LCO
58856.33	+2.33	<i>r</i>	16.15	0.03	LCO
58856.33	+2.33	<i>r</i>	16.15	0.03	LCO
58856.37	+2.37	<i>r</i>	15.54	0.04	LCO
58856.41	+2.41	<i>r</i>	>16.44	–	LCO
58856.41	+2.41	<i>r</i>	16.62	0.28	LCO
58856.41	+2.41	<i>r</i>	15.79	0.04	LCO
58856.70	+2.70	<i>r</i>	15.92	0.04	LCO
58856.74	+2.74	<i>r</i>	15.74	0.03	LCO
58856.74	+2.74	<i>r</i>	15.74	0.03	LCO
58857.30	+3.30	<i>r</i>	15.45	0.03	LCO
58857.30	+3.30	<i>r</i>	15.39	0.03	Synthetic
58857.30	+3.30	<i>r</i>	15.20	0.03	LCO
58857.30	+3.30	<i>r</i>	>16.84	–	LCO
58857.32	+3.32	<i>r</i>	>17.03	–	LCO
58857.32	+3.32	<i>r</i>	15.51	0.03	LCO
58857.35	+3.35	<i>r</i>	>17.23	–	LCO
58857.35	+3.35	<i>r</i>	15.48	0.03	LCO
58857.37	+3.37	<i>r</i>	15.66	0.18	LCO
58857.72	+3.72	<i>r</i>	15.24	0.03	LCO
58857.72	+3.72	<i>r</i>	15.09	0.03	LCO
58858.30	+4.30	<i>r</i>	14.87	0.04	LCO
58858.30	+4.30	<i>r</i>	14.96	0.03	LCO
58858.30	+4.30	<i>r</i>	14.97	0.03	LCO
58858.31	+4.31	<i>r</i>	15.00	0.03	LCO
58858.34	+4.34	<i>r</i>	14.91	0.03	LCO

MJD	Phase	Band	Mag.	Uncertainty	Telescope
58859.05	+5.05	<i>r</i>	14.80	0.03	LCO
58859.30	+5.30	<i>r</i>	14.58	0.03	LCO
58859.48	+5.48	<i>r</i>	14.39	0.03	ZTF
58859.69	+5.69	<i>r</i>	14.46	0.03	LCO
58860.05	+6.05	<i>r</i>	14.33	0.03	LCO
58860.08	+6.08	<i>r</i>	14.31	0.03	LCO
58860.08	+6.08	<i>r</i>	14.32	0.03	LCO
58861.05	+7.05	<i>r</i>	14.04	0.03	LCO
58861.29	+7.29	<i>r</i>	14.00	0.03	LCO
58861.35	+7.35	<i>r</i>	14.00	0.03	LCO
58861.35	+7.35	<i>r</i>	14.05	0.03	LCO
58861.68	+7.68	<i>r</i>	13.98	0.03	LCO
58862.36	+8.36	<i>r</i>	13.87	0.03	LCO
58862.37	+8.37	<i>r</i>	13.88	0.03	LCO
58864.31	+10.31	<i>r</i>	13.58	0.04	LCO
58864.34	+10.34	<i>r</i>	13.62	0.03	Thacher
58864.60	+10.60	<i>r</i>	13.54	0.03	Synthetic
58864.75	+10.75	<i>r</i>	13.54	0.03	LCO
58864.75	+10.75	<i>r</i>	13.62	0.03	LCO
58864.75	+10.75	<i>r</i>	13.54	0.03	LCO
58865.46	+11.46	<i>r</i>	13.56	0.04	Thacher
58866.31	+12.31	<i>r</i>	13.50	0.03	LCO
58866.32	+12.32	<i>r</i>	13.57	0.03	Thacher
58867.30	+13.30	<i>r</i>	13.56	0.03	LCO
58867.35	+13.35	<i>r</i>	13.57	0.03	Thacher
58867.40	+13.40	<i>r</i>	13.56	0.03	LCO
58867.40	+13.40	<i>r</i>	13.59	0.03	LCO
58867.48	+13.48	<i>r</i>	13.51	0.03	ZTF
58868.27	+14.27	<i>r</i>	13.68	0.03	LCO
58868.27	+14.27	<i>r</i>	13.50	0.03	LCO
58868.27	+14.27	<i>r</i>	13.50	0.03	LCO
58868.60	+14.60	<i>r</i>	13.65	0.03	Synthetic
58869.27	+15.27	<i>r</i>	13.82	0.03	LCO
58869.35	+15.35	<i>r</i>	13.75	0.03	Swope
58869.35	+15.35	<i>r</i>	13.62	0.03	Swope
58869.36	+15.36	<i>r</i>	13.67	0.03	LCO
58869.36	+15.36	<i>r</i>	13.68	0.03	LCO
58869.57	+15.57	<i>r</i>	13.63	0.03	PS1
58870.27	+16.27	<i>r</i>	14.00	0.03	LCO
58870.31	+16.31	<i>r</i>	13.69	0.03	Swope
58870.50	+16.50	<i>r</i>	13.82	0.03	Synthetic
58871.27	+17.27	<i>r</i>	14.00	0.03	LCO
58871.32	+17.32	<i>r</i>	13.86	0.03	LCO
58871.32	+17.32	<i>r</i>	13.92	0.03	LCO
58871.32	+17.32	<i>r</i>	13.93	0.03	LCO

MJD	Phase	Band	Mag.	Uncertainty	Telescope
58871.34	+17.34	<i>r</i>	13.88	0.03	Thacher
58871.35	+17.35	<i>r</i>	13.79	0.03	Swope
58871.50	+17.50	<i>r</i>	13.86	0.03	ZTF
58872.29	+18.29	<i>r</i>	13.96	0.03	LCO
58872.33	+18.33	<i>r</i>	13.99	0.03	Thacher
58872.35	+18.35	<i>r</i>	14.06	0.03	Swope
58872.40	+18.40	<i>r</i>	14.02	0.03	Synthetic
58873.09	+19.09	<i>r</i>	14.09	0.03	LCO
58873.10	+19.10	<i>r</i>	14.16	0.03	LCO
58873.10	+19.10	<i>r</i>	14.14	0.03	LCO
58873.40	+19.40	<i>r</i>	14.09	0.03	Thacher
58874.28	+20.28	<i>r</i>	14.22	0.03	LCO
58874.29	+20.29	<i>r</i>	14.26	0.03	Thacher
58874.37	+20.37	<i>r</i>	14.28	0.03	Swope
58875.00	+21.00	<i>r</i>	14.34	0.03	Synthetic
58875.26	+21.26	<i>r</i>	14.46	0.03	LCO
58875.37	+21.37	<i>r</i>	14.33	0.03	Swope
58875.52	+21.52	<i>r</i>	14.38	0.03	ZTF
58876.03	+22.03	<i>r</i>	14.52	0.03	LCO
58876.03	+22.03	<i>r</i>	14.54	0.03	LCO
58876.29	+22.29	<i>r</i>	14.45	0.04	Thacher
58876.34	+22.34	<i>r</i>	14.62	0.03	LCO
58876.36	+22.36	<i>r</i>	14.49	0.03	Swope
58876.70	+22.70	<i>r</i>	14.57	0.03	Synthetic
58877.03	+23.03	<i>r</i>	14.64	0.03	LCO
58877.03	+23.03	<i>r</i>	>17.96	–	LCO
58877.03	+23.03	<i>r</i>	14.62	0.03	LCO
58877.26	+23.26	<i>r</i>	14.65	0.03	LCO
58877.26	+23.26	<i>r</i>	14.68	0.03	LCO
58878.28	+24.28	<i>r</i>	14.60	0.04	Thacher
58878.34	+24.34	<i>r</i>	14.83	0.03	LCO
58878.36	+24.36	<i>r</i>	14.80	0.03	ZTF
58879.40	+25.40	<i>r</i>	14.92	0.03	Synthetic
58880.12	+26.12	<i>r</i>	14.96	0.03	LCO
58880.12	+26.12	<i>r</i>	>17.30	–	LCO
58880.12	+26.12	<i>r</i>	15.02	0.03	LCO
58880.29	+26.29	<i>r</i>	15.03	0.03	Thacher
58880.30	+26.30	<i>r</i>	15.02	0.03	Synthetic
58880.40	+26.40	<i>r</i>	15.03	0.03	Synthetic
58880.44	+26.44	<i>r</i>	>18.07	–	Nickel
58881.28	+27.28	<i>r</i>	15.11	0.03	Thacher
58881.54	+27.54	<i>r</i>	15.02	0.03	ZTF
58882.00	+28.00	<i>r</i>	15.27	0.03	LCO
58882.09	+28.09	<i>r</i>	15.20	0.03	LCO
58882.09	+28.09	<i>r</i>	15.20	0.03	LCO

MJD	Phase	Band	Mag.	Uncertainty	Telescope
58882.32	+28.32	<i>r</i>	15.31	0.03	Swope
58883.01	+29.01	<i>r</i>	15.24	0.03	LCO
58883.12	+29.12	<i>r</i>	15.28	0.03	LCO
58883.12	+29.12	<i>r</i>	15.34	0.03	LCO
58883.37	+29.37	<i>r</i>	15.40	0.03	Swope
58884.00	+30.00	<i>r</i>	15.42	0.03	LCO
58884.00	+30.00	<i>r</i>	15.39	0.03	LCO
58884.37	+30.37	<i>r</i>	>18.20	–	LCO
58884.37	+30.37	<i>r</i>	15.32	0.03	Swope
58884.37	+30.37	<i>r</i>	15.42	0.03	LCO
58884.52	+30.52	<i>r</i>	15.34	0.03	ZTF
58885.35	+31.35	<i>r</i>	15.43	0.03	Swope
58886.28	+32.28	<i>r</i>	15.51	0.04	Thacher
58887.52	+33.52	<i>r</i>	15.46	0.03	ZTF
58890.28	+36.28	<i>r</i>	15.61	0.06	Thacher
58892.00	+38.00	<i>r</i>	15.83	0.03	Synthetic
58892.27	+38.27	<i>r</i>	15.85	0.04	Thacher
58892.32	+38.32	<i>r</i>	15.77	0.03	ZTF
58893.25	+39.25	<i>r</i>	15.89	0.03	Thacher
58893.29	+39.29	<i>r</i>	15.98	0.03	Swope
58894.26	+40.26	<i>r</i>	16.00	0.03	Thacher
58894.31	+40.31	<i>r</i>	15.99	0.03	Swope
58895.00	+41.00	<i>r</i>	15.96	0.03	Synthetic
58895.24	+41.24	<i>r</i>	16.56	0.26	Swope
58895.28	+41.28	<i>r</i>	15.91	0.03	Swope
58895.29	+41.29	<i>r</i>	>16.39	–	LCO
58895.43	+41.43	<i>r</i>	15.99	0.17	Nickel
58895.44	+41.44	<i>r</i>	>19.01	–	Nickel
58895.44	+41.44	<i>r</i>	15.84	0.03	ZTF
58896.29	+42.29	<i>r</i>	15.97	0.03	Swope
58897.31	+43.31	<i>r</i>	16.15	0.03	Swope
58897.31	+43.31	<i>r</i>	15.91	0.08	Swope
58898.24	+44.24	<i>r</i>	16.17	0.04	Thacher
58898.37	+44.37	<i>r</i>	15.90	0.03	ZTF
58899.23	+45.23	<i>r</i>	16.05	0.04	Thacher
58899.44	+45.44	<i>r</i>	16.01	0.03	ZTF
58900.34	+46.34	<i>r</i>	16.11	0.04	Thacher
58900.38	+46.38	<i>r</i>	16.13	0.31	Nickel
58900.44	+46.44	<i>r</i>	16.04	0.03	ZTF
58901.42	+47.42	<i>r</i>	16.08	0.03	ZTF
58902.24	+48.24	<i>r</i>	>16.54	–	LCO
58902.26	+48.26	<i>r</i>	16.01	0.04	Thacher
58903.27	+49.27	<i>r</i>	16.24	0.04	Swope
58903.27	+49.27	<i>r</i>	16.16	0.03	Swope
58903.29	+49.29	<i>r</i>	16.24	0.04	Thacher
58904.32	+50.32	<i>r</i>	16.19	0.03	Swope

MJD	Phase	Band	Mag.	Uncertainty	Telescope
58904.35	+50.35	<i>r</i>	>18.74	–	Nickel
58904.47	+50.47	<i>r</i>	16.21	0.03	ZTF
58905.28	+51.28	<i>r</i>	16.23	0.03	Swope
58905.28	+51.28	<i>r</i>	16.34	0.03	Swope
58905.57	+51.57	<i>r</i>	16.28	0.07	Thacher
58906.27	+52.27	<i>r</i>	16.24	0.03	Swope
58906.45	+52.45	<i>r</i>	16.25	0.03	ZTF
58907.36	+53.36	<i>r</i>	16.34	0.03	Swope
58908.30	+54.30	<i>r</i>	16.41	0.03	Swope
58908.30	+54.30	<i>r</i>	16.45	0.03	Swope
58908.45	+54.45	<i>r</i>	16.26	0.03	ZTF
58909.35	+55.35	<i>r</i>	16.37	0.03	Swope
58910.16	+56.16	<i>r</i>	>17.32	–	LCO
58910.24	+56.24	<i>r</i>	16.39	0.03	Swope
58911.20	+57.20	<i>r</i>	16.41	0.03	Swope
58911.45	+57.45	<i>r</i>	16.42	0.03	ZTF
58912.27	+58.27	<i>r</i>	16.19	0.12	Swope
58912.45	+58.45	<i>r</i>	16.45	0.03	ZTF
58913.45	+59.45	<i>r</i>	16.42	0.03	ZTF
58914.27	+60.27	<i>r</i>	>17.17	–	LCO
58914.38	+60.38	<i>r</i>	16.53	0.03	ZTF
58915.40	+61.40	<i>r</i>	16.49	0.04	ZTF
58919.14	+65.14	<i>r</i>	>16.41	–	LCO
58923.14	+69.14	<i>r</i>	>17.24	–	LCO
58929.50	+75.50	<i>r</i>	>17.02	–	LCO
58929.50	+75.50	<i>r</i>	>13.08	–	LCO
58935.64	+81.64	<i>r</i>	16.52	0.36	LCO
58935.64	+81.64	<i>r</i>	>16.52	–	LCO
58936.41	+82.41	<i>r</i>	17.20	0.04	ZTF
58939.36	+85.36	<i>r</i>	17.58	0.10	ZTF
58942.51	+88.51	<i>r</i>	17.22	0.05	PS1
58943.46	+89.46	<i>r</i>	16.16	0.36	LCO
58943.46	+89.46	<i>r</i>	>16.16	–	LCO
58952.44	+98.44	<i>r</i>	>17.75	–	LCO
58954.18	+100.18	<i>r</i>	>19.56	–	Nickel
58954.26	+100.26	<i>r</i>	17.79	0.04	ZTF
58955.27	+101.27	<i>r</i>	17.77	0.04	ZTF
58955.28	+101.28	<i>r</i>	18.21	0.07	ZTF
58959.34	+105.34	<i>r</i>	>17.53	–	LCO
58962.28	+108.28	<i>r</i>	18.17	0.06	ZTF
58963.21	+109.21	<i>r</i>	>19.12	–	Nickel
58964.27	+110.27	<i>r</i>	18.06	0.05	ZTF
58965.29	+111.29	<i>r</i>	18.14	0.05	ZTF
58966.35	+112.35	<i>r</i>	>16.59	–	LCO
58968.20	+114.20	<i>r</i>	18.12	0.05	ZTF
58971.21	+117.21	<i>r</i>	18.37	0.07	ZTF

MJD	Phase	Band	Mag.	Uncertainty	Telescope	MJD	Phase	Band	Mag.	Uncertainty	Telescope
58974.11	+120.11	<i>r</i>	>16.83	–	LCO	58856.41	+2.41	<i>i</i>	16.12	0.04	LCO
58974.25	+120.25	<i>r</i>	19.40	0.30	ZTF	58856.70	+2.70	<i>i</i>	>14.68	–	LCO
58976.42	+122.42	<i>r</i>	17.96	0.16	PS1	58856.70	+2.70	<i>i</i>	15.11	0.05	LCO
58978.29	+124.29	<i>r</i>	19.55	0.24	ZTF	58856.70	+2.70	<i>i</i>	15.75	0.07	LCO
58980.25	+126.25	<i>r</i>	19.19	0.12	ZTF	58856.74	+2.74	<i>i</i>	16.08	0.06	LCO
58980.76	+126.76	<i>r</i>	>16.86	–	LCO	58856.74	+2.74	<i>i</i>	16.06	0.03	LCO
58988.32	+134.32	<i>r</i>	>16.91	–	LCO	58857.30	+3.30	<i>i</i>	15.93	0.04	LCO
58994.21	+140.21	<i>r</i>	19.35	0.14	ZTF	58857.30	+3.30	<i>i</i>	15.55	0.40	Synthetic
58995.60	+141.60	<i>r</i>	16.22	0.05	Synthetic	58857.32	+3.32	<i>i</i>	15.82	0.03	LCO
58996.50	+142.50	<i>r</i>	>17.18	–	LCO	58857.35	+3.35	<i>i</i>	15.74	0.03	LCO
59002.75	+148.75	<i>r</i>	>18.54	–	LCO	58857.72	+3.72	<i>i</i>	15.30	0.04	LCO
59007.71	+153.71	<i>r</i>	>18.50	–	LCO	58857.72	+3.72	<i>i</i>	>16.74	–	LCO
59014.23	+160.23	<i>r</i>	20.08	0.28	ZTF	58857.72	+3.72	<i>i</i>	15.39	0.04	LCO
59014.80	+160.80	<i>r</i>	>18.73	–	LCO	58858.30	+4.30	<i>i</i>	15.28	0.03	LCO
59017.24	+163.24	<i>r</i>	20.33	0.32	ZTF	58858.30	+4.30	<i>i</i>	15.29	0.03	LCO
59020.24	+166.24	<i>r</i>	20.00	0.28	ZTF	58858.31	+4.31	<i>i</i>	15.31	0.03	LCO
59032.34	+178.34	<i>r</i>	>20.04	–	LCO	58858.34	+4.34	<i>i</i>	15.18	0.03	LCO
59038.72	+184.72	<i>r</i>	>19.34	–	LCO	58859.05	+5.05	<i>i</i>	14.97	0.03	LCO
59175.50	+321.50	<i>r</i>	18.75	0.33	ZTF	58859.30	+5.30	<i>i</i>	14.88	0.03	LCO
59193.54	+339.54	<i>r</i>	19.91	0.27	ZTF	58859.69	+5.69	<i>i</i>	14.75	0.03	LCO
59202.10	+348.10	<i>r</i>	>18.46	–	LCO	58860.05	+6.05	<i>i</i>	14.58	0.03	LCO
59203.50	+349.50	<i>r</i>	19.89	0.34	ZTF	58860.08	+6.08	<i>i</i>	14.63	0.03	LCO
59208.07	+354.07	<i>r</i>	>18.22	–	LCO	58860.08	+6.08	<i>i</i>	14.59	0.03	LCO
59214.05	+360.05	<i>r</i>	>17.97	–	LCO	58861.05	+7.05	<i>i</i>	14.34	0.03	LCO
59217.41	+363.41	<i>r</i>	19.58	0.28	ZTF	58861.05	+7.05	<i>i</i>	14.28	0.03	LCO
59220.37	+366.37	<i>r</i>	>17.88	–	LCO	58861.29	+7.29	<i>i</i>	14.31	0.03	LCO
59225.51	+371.51	<i>r</i>	18.98	0.30	ZTF	58861.35	+7.35	<i>i</i>	14.38	0.03	LCO
59226.11	+372.11	<i>r</i>	>17.59	–	LCO	58861.35	+7.35	<i>i</i>	14.35	0.03	LCO
59227.72	+373.72	<i>r</i>	>18.37	–	LCO	58861.69	+7.69	<i>i</i>	14.20	0.03	LCO
59232.38	+378.38	<i>r</i>	>16.59	–	LCO	58861.69	+7.69	<i>i</i>	>15.85	–	LCO
59236.06	+382.06	<i>r</i>	>17.78	–	LCO	58861.69	+7.69	<i>i</i>	14.00	0.03	LCO
59245.42	+391.42	<i>r</i>	>18.30	–	LCO	58862.37	+8.37	<i>i</i>	14.08	0.03	LCO
59252.06	+398.06	<i>r</i>	>17.81	–	LCO	58862.37	+8.37	<i>i</i>	14.07	0.03	LCO
59252.33	+398.33	<i>r</i>	20.21	0.30	ZTF	58862.53	+8.53	<i>i</i>	14.02	0.04	Thacher
59257.33	+403.33	<i>r</i>	>18.84	–	LCO	58864.31	+10.31	<i>i</i>	13.87	0.04	LCO
59262.23	+408.23	<i>r</i>	>18.25	–	LCO	58864.34	+10.34	<i>i</i>	13.83	0.03	Thacher
59267.12	+413.12	<i>r</i>	>17.02	–	LCO	58864.60	+10.60	<i>i</i>	13.79	0.35	Synthetic
59275.38	+421.38	<i>r</i>	19.55	0.22	ZTF	58864.76	+10.76	<i>i</i>	13.89	0.03	LCO
58873.25	+19.25	<i>G</i>	14.29	0.20	Gaia	58865.46	+11.46	<i>i</i>	13.76	0.05	Thacher
58547.44	-306.56	<i>i</i>	19.47	0.32	ZTF	58866.31	+12.31	<i>i</i>	13.73	0.03	LCO
58856.31	+2.31	<i>i</i>	17.52	0.12	LCO	58866.33	+12.33	<i>i</i>	13.79	0.03	Thacher
58856.34	+2.34	<i>i</i>	16.47	0.04	LCO	58866.56	+12.56	<i>i</i>	13.76	0.03	PS1
58856.34	+2.34	<i>i</i>	16.57	0.04	LCO	58867.30	+13.30	<i>i</i>	13.84	0.03	LCO
58856.37	+2.37	<i>i</i>	16.15	0.05	LCO	58867.35	+13.35	<i>i</i>	13.82	0.03	Thacher

MJD	Phase	Band	Mag.	Uncertainty	Telescope	MJD	Phase	Band	Mag.	Uncertainty	Telescope
58867.40	+13.40	<i>i</i>	13.79	0.03	LCO	58880.12	+26.12	<i>i</i>	15.08	0.03	LCO
58868.28	+14.28	<i>i</i>	14.00	0.03	LCO	58880.12	+26.12	<i>i</i>	15.05	0.03	LCO
58868.60	+14.60	<i>i</i>	13.84	0.35	Synthetic	58880.29	+26.29	<i>i</i>	15.06	0.03	Thacher
58869.27	+15.27	<i>i</i>	13.98	0.03	LCO	58880.30	+26.30	<i>i</i>	14.99	0.38	Synthetic
58869.35	+15.35	<i>i</i>	13.85	0.03	Swope	58880.40	+26.40	<i>i</i>	15.13	0.39	Synthetic
58869.36	+15.36	<i>i</i>	13.92	0.03	LCO	58880.44	+26.44	<i>i</i>	>17.34	–	Nickel
58869.36	+15.36	<i>i</i>	13.94	0.03	LCO	58881.28	+27.28	<i>i</i>	15.16	0.03	Thacher
58870.27	+16.27	<i>i</i>	14.25	0.03	LCO	58882.00	+28.00	<i>i</i>	>18.24	–	LCO
58870.32	+16.32	<i>i</i>	13.97	0.03	Swope	58882.00	+28.00	<i>i</i>	15.26	0.03	LCO
58870.32	+16.32	<i>i</i>	13.88	0.03	Swope	58882.00	+28.00	<i>i</i>	15.19	0.10	LCO
58870.50	+16.50	<i>i</i>	13.91	0.35	Synthetic	58882.09	+28.09	<i>i</i>	15.31	0.03	LCO
58871.32	+17.32	<i>i</i>	14.13	0.03	LCO	58882.09	+28.09	<i>i</i>	15.28	0.03	LCO
58871.32	+17.32	<i>i</i>	14.06	0.03	LCO	58882.32	+28.32	<i>i</i>	15.38	0.03	Swope
58871.34	+17.34	<i>i</i>	14.06	0.03	Thacher	58883.12	+29.12	<i>i</i>	15.34	0.03	LCO
58871.35	+17.35	<i>i</i>	14.03	0.03	Swope	58883.12	+29.12	<i>i</i>	15.31	0.03	LCO
58872.29	+18.29	<i>i</i>	14.07	0.03	LCO	58883.37	+29.37	<i>i</i>	15.48	0.03	Swope
58872.29	+18.29	<i>i</i>	14.15	0.03	LCO	58884.00	+30.00	<i>i</i>	15.44	0.03	LCO
58872.29	+18.29	<i>i</i>	14.07	0.03	LCO	58884.00	+30.00	<i>i</i>	15.41	0.03	LCO
58872.33	+18.33	<i>i</i>	14.12	0.03	Thacher	58884.37	+30.37	<i>i</i>	15.50	0.03	LCO
58872.35	+18.35	<i>i</i>	14.28	0.03	Swope	58884.37	+30.37	<i>i</i>	15.22	0.03	Swope
58872.40	+18.40	<i>i</i>	13.79	0.35	Synthetic	58885.35	+31.35	<i>i</i>	15.53	0.03	Swope
58873.09	+19.09	<i>i</i>	14.30	0.03	LCO	58886.28	+32.28	<i>i</i>	15.57	0.04	Thacher
58873.10	+19.10	<i>i</i>	14.22	0.03	LCO	58890.28	+36.28	<i>i</i>	15.62	0.06	Thacher
58873.10	+19.10	<i>i</i>	14.23	0.03	LCO	58892.00	+38.00	<i>i</i>	15.25	0.39	Synthetic
58873.40	+19.40	<i>i</i>	14.24	0.03	Thacher	58892.27	+38.27	<i>i</i>	15.89	0.04	Thacher
58874.29	+20.29	<i>i</i>	>16.62	–	LCO	58893.25	+39.25	<i>i</i>	15.90	0.03	Thacher
58874.29	+20.29	<i>i</i>	14.36	0.03	LCO	58893.29	+39.29	<i>i</i>	15.97	0.03	Swope
58874.29	+20.29	<i>i</i>	14.34	0.03	Thacher	58894.26	+40.26	<i>i</i>	16.03	0.04	Thacher
58874.29	+20.29	<i>i</i>	14.53	0.08	LCO	58894.31	+40.31	<i>i</i>	16.08	0.03	Swope
58875.00	+21.00	<i>i</i>	14.25	0.36	Synthetic	58895.00	+41.00	<i>i</i>	15.92	0.41	Synthetic
58875.26	+21.26	<i>i</i>	14.56	0.03	LCO	58895.29	+41.29	<i>i</i>	16.01	0.03	Swope
58875.38	+21.38	<i>i</i>	14.46	0.03	Swope	58895.29	+41.29	<i>i</i>	>16.20	–	LCO
58876.03	+22.03	<i>i</i>	14.60	0.03	LCO	58895.43	+41.43	<i>i</i>	15.31	0.07	Nickel
58876.03	+22.03	<i>i</i>	14.61	0.03	LCO	58895.44	+41.44	<i>i</i>	>18.83	–	Nickel
58876.29	+22.29	<i>i</i>	14.39	0.04	Thacher	58896.29	+42.29	<i>i</i>	15.45	0.04	Swope
58876.34	+22.34	<i>i</i>	14.60	0.04	LCO	58897.31	+43.31	<i>i</i>	15.75	0.03	Swope
58876.36	+22.36	<i>i</i>	14.62	0.03	Swope	58898.24	+44.24	<i>i</i>	16.01	0.04	Thacher
58876.70	+22.70	<i>i</i>	14.04	0.36	Synthetic	58899.24	+45.24	<i>i</i>	16.24	0.05	Thacher
58877.03	+23.03	<i>i</i>	14.75	0.03	LCO	58900.35	+46.35	<i>i</i>	16.06	0.04	Thacher
58877.03	+23.03	<i>i</i>	14.71	0.03	LCO	58900.38	+46.38	<i>i</i>	>18.23	–	Nickel
58877.27	+23.27	<i>i</i>	14.70	0.03	LCO	58902.24	+48.24	<i>i</i>	>16.52	–	LCO
58878.07	+24.07	<i>i</i>	14.75	0.03	LCO	58902.26	+48.26	<i>i</i>	16.12	0.06	Thacher
58878.07	+24.07	<i>i</i>	14.75	0.03	LCO	58903.27	+49.27	<i>i</i>	16.25	0.03	Swope
58878.07	+24.07	<i>i</i>	>15.15	–	LCO	58903.29	+49.29	<i>i</i>	16.10	0.04	Thacher
58878.29	+24.29	<i>i</i>	14.77	0.04	Thacher	58904.32	+50.32	<i>i</i>	16.30	0.04	Swope
58878.34	+24.34	<i>i</i>	14.84	0.03	LCO	58904.35	+50.35	<i>i</i>	>19.00	–	Nickel
58879.40	+25.40	<i>i</i>	14.97	0.38	Synthetic	58905.29	+51.29	<i>i</i>	16.41	0.03	Swope

MJD	Phase	Band	Mag.	Uncertainty	Telescope
58905.58	+51.58	<i>i</i>	16.25	0.16	Thacher
58906.10	+52.10	<i>i</i>	>17.05	–	LCO
58906.10	+52.10	<i>i</i>	15.61	0.04	LCO
58906.28	+52.28	<i>i</i>	16.49	0.03	Swope
58907.36	+53.36	<i>i</i>	16.39	0.03	Swope
58908.30	+54.30	<i>i</i>	16.54	0.03	Swope
58908.30	+54.30	<i>i</i>	16.55	0.03	Swope
58909.36	+55.36	<i>i</i>	16.60	0.03	Swope
58911.20	+57.20	<i>i</i>	16.51	0.04	Swope
58912.27	+58.27	<i>i</i>	16.53	0.04	Swope
58919.14	+65.14	<i>i</i>	>16.37	–	LCO
58923.14	+69.14	<i>i</i>	>17.26	–	LCO
58923.27	+69.27	<i>i</i>	16.36	0.03	Swope
58929.50	+75.50	<i>i</i>	>12.78	–	LCO
58929.50	+75.50	<i>i</i>	>16.73	–	LCO
58935.64	+81.64	<i>i</i>	16.52	0.36	LCO
58935.64	+81.64	<i>i</i>	>16.52	–	LCO
58943.46	+89.46	<i>i</i>	>15.74	–	LCO
58943.46	+89.46	<i>i</i>	15.74	0.36	LCO
58952.44	+98.44	<i>i</i>	>17.70	–	LCO
58954.18	+100.18	<i>i</i>	>18.80	–	Nickel
58959.34	+105.34	<i>i</i>	>17.52	–	LCO
58963.21	+109.21	<i>i</i>	>18.28	–	Nickel
58966.35	+112.35	<i>i</i>	>16.49	–	LCO
58974.11	+120.11	<i>i</i>	>16.62	–	LCO
58980.76	+126.76	<i>i</i>	>16.62	–	LCO
58988.32	+134.32	<i>i</i>	>16.70	–	LCO
58995.60	+141.60	<i>i</i>	16.23	0.52	Synthetic
58996.50	+142.50	<i>i</i>	>17.25	–	LCO
59002.75	+148.75	<i>i</i>	>18.46	–	LCO
59007.71	+153.71	<i>i</i>	>18.41	–	LCO
59014.80	+160.80	<i>i</i>	>18.49	–	LCO
59026.35	+172.35	<i>i</i>	>17.34	–	LCO
59032.34	+178.34	<i>i</i>	>19.96	–	LCO
59038.72	+184.72	<i>i</i>	>19.58	–	LCO
59202.10	+348.10	<i>i</i>	>18.22	–	LCO
59208.07	+354.07	<i>i</i>	>17.68	–	LCO
59214.05	+360.05	<i>i</i>	>17.97	–	LCO
59220.37	+366.37	<i>i</i>	>17.76	–	LCO
59226.11	+372.11	<i>i</i>	>16.87	–	LCO
59227.72	+373.72	<i>i</i>	>18.22	–	LCO
59232.38	+378.38	<i>i</i>	>16.44	–	LCO
59236.06	+382.06	<i>i</i>	>17.02	–	LCO
59245.42	+391.42	<i>i</i>	>18.28	–	LCO
59252.06	+398.06	<i>i</i>	>17.33	–	LCO
59257.33	+403.33	<i>i</i>	>18.78	–	LCO
59262.23	+408.23	<i>i</i>	>18.13	–	LCO

MJD	Phase	Band	Mag.	Uncertainty	Telescope
59267.12	+413.12	<i>i</i>	>16.71	–	LCO
58857.30	+3.30	<i>z</i>	15.56	0.40	Synthetic
58862.53	+8.53	<i>z</i>	14.08	0.04	Thacher
58864.34	+10.34	<i>z</i>	13.84	0.03	Thacher
58864.60	+10.60	<i>z</i>	13.82	0.35	Synthetic
58866.33	+12.33	<i>z</i>	13.79	0.04	Thacher
58867.36	+13.36	<i>z</i>	13.78	0.04	Thacher
58868.60	+14.60	<i>z</i>	13.83	0.35	Synthetic
58870.50	+16.50	<i>z</i>	13.82	0.35	Synthetic
58871.34	+17.34	<i>z</i>	14.00	0.04	Thacher
58872.34	+18.34	<i>z</i>	14.06	0.03	Thacher
58873.41	+19.41	<i>z</i>	14.11	0.03	Thacher
58874.29	+20.29	<i>z</i>	14.23	0.04	Thacher
58876.29	+22.29	<i>z</i>	14.35	0.05	Thacher
58878.29	+24.29	<i>z</i>	14.45	0.06	Thacher
58880.29	+26.29	<i>z</i>	14.76	0.04	Thacher
58880.40	+26.40	<i>z</i>	14.74	0.37	Synthetic
58881.29	+27.29	<i>z</i>	14.82	0.04	Thacher
58886.29	+32.29	<i>z</i>	15.04	0.04	Thacher
58890.29	+36.29	<i>z</i>	15.30	0.06	Thacher
58892.27	+38.27	<i>z</i>	15.23	0.05	Thacher
58893.25	+39.25	<i>z</i>	15.31	0.05	Thacher
58894.26	+40.26	<i>z</i>	15.24	0.04	Thacher
58898.25	+44.25	<i>z</i>	15.33	0.04	Thacher
58899.24	+45.24	<i>z</i>	15.35	0.05	Thacher
58900.35	+46.35	<i>z</i>	15.32	0.04	Thacher
58903.30	+49.30	<i>z</i>	15.59	0.05	Thacher
58905.58	+51.58	<i>z</i>	15.41	0.15	Thacher
58942.52	+88.52	<i>z</i>	16.77	0.06	PS1